# Offshore wind turbine blade installation

## Development of a motion-compensated Stewart platform for blade installation with a floating vessel

Master thesis

Jadyr Macabú Araújo Peres

Delft University of Technology | Norwegian University of Science and Technology

TU Delft

NTNU

# Offshore wind turbine blade installation

## Development of a motion-compensated Stewart platform for blade installation with a floating vessel

by

Jadyr Macabú Araújo Peres

| Student Number | |
|---|---|
| 5612403 | TU Delft |
| 595263 | NTNU |

in partial fulfillment of the requirements to obtain the degrees of

Master of Science in Offshore and Dredging Engineering at the Delft University of Technology

&

Master of Science in Technology - Wind Energy at the Norwegian University of Science and Technology

under the European Wind Energy Master programme.

To be publicly defended on Monday 28th of August 2023 at 13:00h.

| | |
|---|---|
| Supervisor TU Delft: | Dr. ir. Sebastiaan Mulders |
| Supervisor NTNU: | Prof. dr. ir. Dong Trong Nguyen |
| Co-Supervisor NTNU: | Prof. dr. ir. Zhen Gao |
| Supervisor Heerema Marine Contractors: | Jurgen de Jong |

Cover: Heerema Marine Contractors

# Preface

This master's thesis is submitted to fulfill the requirements to complete the European Wind Energy Master in the Offshore Engineering track, and to obtain the Master's degrees in Offshore and Dredging Engineering from the Delft University of Technology (TU Delft) and Technology - Wind Energy from the Norwegian University of Science and Technology (NTNU). The project was carried out in cooperation with Heerema Marine Contractors.

One year ago, this project began investigating possible motion compensation solutions for the installation of a wind turbine generator blades by a floating vessel, initially focusing on the use of tugger wires and the possible control strategies, both from academia and from products in use by the industry. After an extensive literature review, it was concluded that an alternative solution could be the use of a motion compensated Stewart platform and, based on this, the project was developed and the process detailed in this report.

Motion compensation is developed on the basis of control systems, in which I had close to no knowledge before starting this project. Therefore, I would especially like to thank my supervisors, Dr. ir. Sebastiaan Mulders from TU Delft and Prof. Dr. ir. Dong Trong from NTNU, who were capable to provide extensive and in depth knowledge from this field, and guide me during the whole project. Additionally, I thank Prof. Dr. ir. Zhen Gao, who initiated important discussions, provided a different perspective of the problems, as well as offered his academic expertise in offshore operations, more specifically in the installations of wind turbines.

I would like to especially thank Heerema Marine Contractors, more specifically my supervisor Jurgen de Jong, who helped me with his extensive knowledge and experience not only technically, but also to structure the development of this project.

Lastly, but not least, I would like to thank my EWEM colleagues and the mutual support during the last two years. Most importantly, I would like to thank my family who supported me during the entire process that led to this moment.

*Jadyr Macabú Araújo Peres*
*Leiden - NL, August 2023*

# Abstract

With the increasing water depths of the new offshore wind farms, the challenging soil conditions, the availability of assets, and other factors, jack-up installation vessels may no longer be suitable to complete the installation scope of work for the new wind farms. Therefore, installation methods and techniques using floating vessels must be further developed to allow safe and efficient installation of wind turbines.

Due to the response of floating installation vessels, excessive motions can be transmitted to the lifted object, making the installation operation very weather sensitive. To increase workability, Heerema Marine Contractors (HMC) has developed the RNA method for wind turbine installation using a semi-submersible crane vessel. This method uses a temporary support structure on the vessel deck (installation tower) where the RNA is fully assembled with the assistance of the GREP (Guided Root End Positioning) tool to constrain the blade root to the top of the installation tower and consequently the hub. Finally, the RNA is installed in a single lift on the WTG permanent support structure. However, the GREP tool is compatible only with a specific range of wind turbine blade dimensions; therefore, for a different-size wind turbine blade a new GREP tool must be designed, fabricated, and mobilised.

This project proposes an improvement to the HMC's RNA method to eliminate the necessity of the GREP tool. That is, a motion-compensated Stewart platform attached to the crane boom, where the blade is fixed to be installed in the hub on top of the installation tower. The project is developed by investigating the initial assumptions; those are crane boom stiffness, blade deflection, installation tower motions and their influence on the vessel's response, and aerodynamic loads acting on the blade during installation. The kinematics (inverse and forward) and dynamics of a Stewart platform are formulated, as well as the mechanical concept of the proposed system and the blade installation process using a Stewart platform attached to the crane boom.

Furthermore, to eliminate the requirement of the GREP tool, a control system is developed to compensate for the blade root motions relative to the hub. The motion control system uses sensors to measure the hub's motions and generate the Stewart platform actuators' set points. Different possible sensor set-ups are evaluated, and a filter is designed to reduce the influence of the sensors' noise. The control system is developed on the basis of feedback PI (Proportional and Integral) and adaptive feedforward control to the actuators (hydraulic cylinders).

It is concluded that it is technically feasible to use a motion- compensated Stewart platform for blade installation in the RNA method. However, the economic aspects of the proposed solution must be investigated.

Keywords: *Offshore wind, Installation, Motion compensation, Control, Motion tracking, Stewart platform, Wind turbine installation vessel*

# Contents

# 1

# Introduction

## 1.1. Offshore wind energy

As part of the goals to achieve higher renewable energy production and ensure energy independence, the number of offshore wind farms under licensing and construction has increased significantly in the last years, as governments in Europe pledge up to 135 GW, in capacity, of offshore wind installed by 2030 [1] [2]. Figure 1.1 shows the expected new capacity of wind energy to be connected to the European grid from 2023 to 2027 according to WindEurope, with a significant growing trend for offshore wind farms. The choice of offshore wind energy is also driven by technical and logistic factors. First, the wind at offshore sites has a higher average wind speed and fewer variations compared to onshore, resulting in a higher capacity factor [3]. Additionally, for large wind turbines, transporting its components to offshore wind farms becomes simpler compared to transporting to the transport of long turbine structural components (blades and towers) in challenging terrestrial areas.

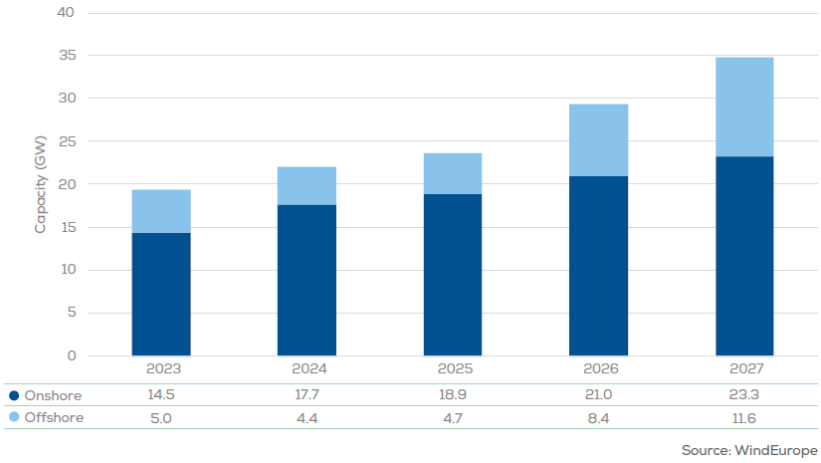


**Figure 1.1:** Expected new installations of wind energy in Europe from 2023 to 2027 under WindEurope's central scenario [3].

Other factors come into place in favor of offshore wind. Although causing an impact to the marine ecosystem, offshore wind farms have less impact to people, as they are offshore, they cause less, or none, visual impact, do not affect possible farming areas, the noise restrictions are not as strict, amongst other factors.

However, offshore wind energy has its own challenges. Wave loads acting on the turbine and its support structures require a more robust design. Maintenance and operation costs (OpEx) are higher when compared with onshore wind. Furthermore, the transport and installation of wind turbines become

more challenging because sites tend to have more challenging conditions and wind turbines grow in size; the average capacity of the ordered offshore wind turbine in 2022 was 12 MW [4]. Figure 1.2 shows the increase in the average wind turbine ordered, which in the future will demand more capable installation vessels and methods.

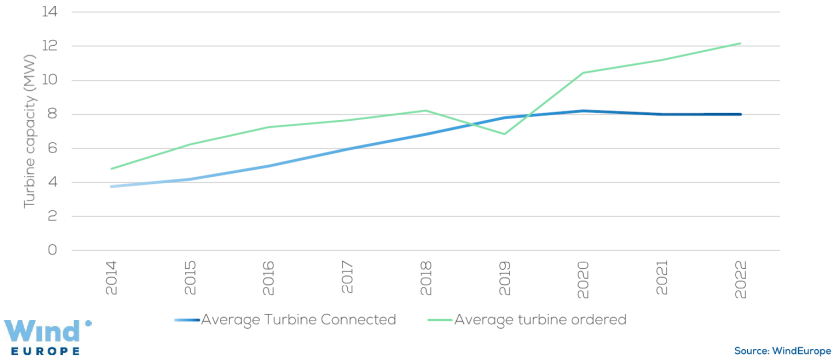


**Figure 1.2:** Average capacity of ordered and connected offshore wind turbine in Europe [4].

## 1.2. Installation of offshore wind turbines

As new offshore wind farms are constructed far from the shore and into deeper waters [1] [2], together with the increase in the turbine size, transport and installation becomes more challenging.

The previous techniques used for turbine installation are no longer technically and economically feasible. These methods were previously developed to reduce the number of lifts during installation by pre-assembling some of the WTG's components, and thus reducing the number of lifts required to install a wind turbine. Nevertheless, the growing size of wind turbines makes the transport of pre-assembled WTG's components inefficient. Furthermore, for larger wind turbines with a rotor diameter of more than 150 m, transportation of the rotor nacelle assembly onboard the installation vessel (or feeder barge) becomes not only a technical challenge, but also a logistical one, since the channels and ports must be able to accommodate this operation. For these reasons, more and more offshore wind farms have been installed using a method that has the greater number of lifts amongst the others, i.e. single-blade installation. Although this method requires at least five lifting operations (1 - single piece tower installation, 1 - hub and nacelle assembly installation, 3 - single blade installation), it allows the storage of more components onboard the installation vessel, minimizing port calls for load-out, port costs, time under transit, and other factors.

As depicted in Figure 1.1, the growing number of new offshore wind farms requires an increase in the number of available transport and installation vessels. Companies such as Cadeler A/S building four new jack-up installation vessels, and Seaway 7 building foundation and wind turbine installation vessels show that the transport and installation companies are working to supply this demand. However, the number of wind turbine installation vessels (WTIVs) under construction may not be sufficient to meet demand [5]. Therefore, it is expected that other vessels, less specialized in the installation of wind turbines or their foundations, will enter this business.

## 1.3. Installation vessels and methods

The typical WTIV is a jack-up heavy lift vessel, nevertheless new vessels are being used in the installation of wind turbines, mainly semisubmersible crane vessels, such as the Saipem 7000 installing the wind turbines for the Hywind floating wind farm back in 2017, and more recently the Heerema Thialf installing the wind turbines for the Arcadis Ost I wind farm.

This not only starts a new chapter in the construction of wind farms by significantly increasing the

number of vessels capable of this kind of operation but also represents a new technical challenge as the conventional techniques used by jack-up vessels cannot be straightforwardly implemented for the installation of wind turbines by floating vessels. Therefore, new techniques are required, mainly due to the motions on the floating vessel caused by wind, waves, and current.

### 1.3.1. Jack-up installation vessels

Since at least 2016, all bottom-founded wind farms built in Europe had their turbines installed by a jack-up installation vessel [4], the only exception was the Arcadis Ost 1 wind farm, where the turbines were installed by the Heerema Marine contractor's SSCV Thialf.

As the largest majority of offshore wind farms built until now is bottom-founded and in places with reasonable soil conditions, jack-up vessels have been the preferred choice for installation of wind turbines, as they have a proven track record of projects executed and have reduced motions, which allows for reasonable workability. One drawback of jack-up installation vessels is that they can only jack-up until a certain sea state [6] [7]. Figure 1.3 depicts a blade installation operation by a jack-up vessel.

As jack-up WTIV are in high demand and are very specialized assets, building new vessels seems like the obvious choice, nevertheless it is not this simple. The design requirements for these kinds of vessel are very specific, for example: the jacking system has to resist a higher amount of loading cycles when compared to jack-up drilling rigs that stay at the same location for a much longer time, jack-up WTIV stays in the same location only for the installation of a single wind turbine and then moves to the next one. This results in the requirement for high-standard materials and design, restricting the number of shipyards capable of building one of these vessels [5]. Additionally, due to the length of the legs while the vessel is floating, they significantly increase the ship's air draft, hence limiting the route she can be in transit due to bridges and other possible obstacles; this restricts even more the possible shipyards [5]. Together with the technical aspects presented above, the construction of a new jack-up WTIV has to also be an economic choice.


**Figure 1.3:** Installation of a wind turbine blade by a jack-up vessel [8].

### 1.3.2. Floating installation vessels

An alternative to jacking up WTIV is to use floating vessels for the installation of wind turbines. As they are a common asset in the Oil&Gas industry, they can be adapted, if necessary, for the installation of wind turbines. To use already built floating vessels for the installation of wind turbines, two main challenges arise; the first is the required lifting height during the installation of wind turbine generators (WTG), as hub heights can reach 150 m, the required lifting height is more than that, therefore, not

every heavy lift floating crane can perform the job, and upgrading a crane is not a simple task as structural limitations may prevent it.

The other main factor is the motions on a floating vessel. Although different equipment, such as anti-roll tanks, are designed to reduce these motions, they are not completely eliminated, and when lifting a fragile and large payload, e.g. a blade, these motions are transmitted to the payload, which may prevent the installation operation. These motions are generally reduced for semi-submersible vessels compared to monohulls; therefore, semi-submersible crane vessels (SSCV) are recommended.

Currently, novel methods have been developed to make the installation of WTG by floating vessels feasible. In Figure 1.4 a rotor nacelle assembly is installed on the WTG support structure in a single lift by a SSCV after being pre-assembled on the vessel's deck. Other methods include lifting the complete WTG in a dual crane operation and placing it on the support structure [9], and the integrated solution proposed by Huisman where a WTG is assembled on the specialized WTIV deck, splitting the process into different paths and reducing the overall duration of the critical path [10]. However, there is still a great horizon of possible innovations that can facilitate the installation of wind turbines by floating vessels, one of them being motion compensation.


**Figure 1.4:** Installation of a rotor nacelle assembly by a floating semi-submersible crane vessel [11].

## 1.4. The RNA method by Heerema Marine Contractors

The RNA (Rotor Nacelle Assembly) method was developed by Heerema Marine Contractors as a competitive solution for the installation of wind turbine generators (WTG) with a floating vessel. With this method, the first commercial size wind farm had its turbines installed by a floating vessel.

In the RNA method, the floating vessel loads the individual turbine components on deck, i.e. the tower, blades, and the nacelle connected to the hub. The installation phase can be divided into two to shorten the critical path. Therefore, one crane installs the tower on the pre-installed foundation, while the other crane places the nacelle on the installation tower. The two main components used in the RNA method are the installation tower and the GREP (Guided Root End Positioning) tool, both described in the next subsections.

### 1.4.1. The installation tower

The installation tower is the temporary support structure on which the nacelle is placed. A key element in the efficiency of the RNA method. Figure 1.5 shows a fully assembled RNA on the installation tower.

In terms of efficiency, it allows the installation process to be split in two paths, while one crane installs the permanent WTG tower on the foundation, the other crane is being used to assemble the RNA. Furthermore, it is also a technical enabler, with the installation tower on the SSCV deck, the relative motions in the traditional single blade installation method, that is, lifting the blade from the deck of the vessel and connecting it to the hub previously installed on the permanent support structure as depicted in Figure 1.3 using a jack-up WTIV.

Because of this set-up, the influence of the vessel's response on the relative motions between blade root and hub is already drastically reduced.

**Figure 1.5:** RNA fully assembled on the installation tower (in blue) on the Thialf's deck. Courtesy of Heerema Marine Contractors.

### 1.4.2. The GREP (Guided Blade Root End Positioning) tool

The GREP tool, as shown in Figure 1.6, is a structure mounted around the upper part of the installation tower and is responsible for guiding the blade root towards the WTG's hub while also restraining the former's motions and making it follow the hub. It allows the blade root to be almost motionless relative to the hub.

While holding and restraining the root of the blade, the GREP guides it towards the hub inserting its bolts into the hub, following the start of the bolting stage and the blade is connected to the hub.

This method developed by Heerema Marine Contractors, and successfully used to install the WTG of the Arcadis Ost 1 wind farm, significantly increases the workability that this type of operation would have with a floating vessel. However, the GREP tool is designed for a specific range of wind turbines, i.e. when installing different-sized wind turbines and blades, a new GREP would have to be designed and built, which can significantly increase the costs in building a wind farm.


**Figure 1.6:** Blade installation using the GREP tool. Courtesy of Heerema Marine Contractors.

### 1.4.3. WTG installation with the RNA method

In the RNA method, the nacelle is placed on top of the installation tower and the blade installation phase starts. Each blade is individually lifted using the BIT (Blade Installation Tool) and its root is placed on the GREP (Guided Blade Root End Positioning) tool, securing the blade root motionless relative to the hub as depicted in Figure 1.6; an example of a BIT is shown in Figure 1.7. With the blade root secured by the GREP, the equipment guides the blade root toward the hub in a controlled manner, connecting the blade to the hub; during this phase, the GREP tool can correct the blade root position in the $x-$, $y-$ and $z-$ directions. The blade is then in its final position and bolted to the hub.

**Figure 1.7:** Blade and BIT example [12].

The GREP is lowered along the installation tower and opens its clamps to free the recently installed blade from it. Once the first installed blade is free from the GREP, the hub is rotated to the position for the installation of the second blade. The same process is repeated for the installation of the second and third blades.

The RNA is now fully assembled; it is then lifted from the installation tower on the SSCV deck and placed on the definitive WTG tower as shown in Figure 1.8, where both parts are connected. The installation of a wind turbine using the RNA method is completed.

This method allows the installation of wind turbines in challenging soil conditions, where the use of jack-up vessels is not possible. Moreover, this methodology is competitive not only when soil conditions are a limitation for jack-up vessels, this method allows the installation of WTG to be split in two parallel

phases, tower installation and completion, and RNA installation due to the fact that the Heerema Marine Contractor's vessels are equipped with two capable cranes. Additionally, the workability of this method is not limited to occasional metocean conditions; furthermore, there is no time required for jacking up and down for the installation of each WTG, making this method competitive with the installation times done by jack-up WTIV.

**Figure 1.8:** RNA installation, lifted from the installation tower on Thialf's deck to be placed on the final WTG tower. Courtesy of Heerema Marine Contractors.

## 1.5. Research challenge

The clear benefits of the GREP tool are explained in Section 1.4, and in more detail in Subsection 1.4.2. However, the existing GREP is a specific tool with a narrow range of compatibility with different sizes of wind turbine blades, additionally, with the growing size of the turbines ordered, it is a tool that can quickly be outdated.

The broad objective of this thesis is to develop a method for blade installation using the RNA method without the GREP tool. For this, a new blade installation method is proposed using a Stewart platform, as well as a model-free control system to control the Stewart platform and compensate the motions between blade root and hub. As this project is intended to be used in the RNA method, the installation tower is still used.

The Stewart platform is a parallel mechanism first proposed in 1965 [13] consisting of a fixed base and a controllable platform connected by a set of actuators. Most commonly, Stewart platforms have a 6-by-6 configuration, i.e., the base structure is connected to the platform structure by six actuators in six joints, where each actuator is attached to the base and platform at different and individual points. It is commonly used in flight simulators and offshore access platforms.

The biggest challenge originates when no primary alignment system (part of the WTG) is used to guide the blade into the hub; in those cases the mating tolerance is only the free space between the blade's bolts and the hub's holes, i.e., in the order of a few millimeters.

## 1.6. Horizontal motion compensation / control

The main challenge in blade installation without the GREP tool is to compensate for motions between blade root and hub. More specifically, the horizontal motions, with higher amplitude.

When the blade is lifted with the vessel's crane to connect it to the hub, vertical relative motions are very small compared to horizontal ones. As the nacelle is on top of the installation tower that is mounted on the vessel's deck, the vertical relative motions originate mainly from the pendulum motion of the blade hanging from the crane's wire. Therefore, if the horizontal blade motions are controlled, the vertical motions of the payload will also be controlled.

### 1.6.1. Motion control by tugger lines

The most common way of controlling a cargo being hoisted by an offshore crane is to use tugger lines. These are traditionally operated in two different modes, constant length and constant tension [14], i.e. maintaining the tugger lines at a constant length while its tension varies with vessel's motions, or paying in and out the tugger line to keep its tension constant. The first alternative severely increases the operation's risk, as the tension on the tugger line can significantly, and suddenly, increase or slack, creating the risk of overloading the wire or even shock loads, both outcomes can break the wire. The constant tension mode pays the tugger line in and out to keep the tension constant, although it, in most cases, protects the wire from breaking, it still allows relatively large motions of the payload.

A simple and efficient solution is the damping tugger system, a proportional controller [14]. The payloads swing is a resonance problem; therefore, if damping is added, motions are reduced. Damping can be added by modifying the constant tension controller of the winch. The proposed modification is that the pay-out/in speed of the tugger wire is measured, and the winch's tension is made a function of the former. The biggest benefit of this motion control system is that the payload's motions are coupled with the vessel's roll response; therefore, damping out the payload's motions also reduces the vessel's roll. Nevertheless, the improved performance of this system is best found when the payload has a large mass and the coupling with the vessel's roll response is more significant. When controlling the motions of light-weight objects, such as blades, its performance is very similar to that of a constant tension tugger system.

Active motion compensation systems using tugger winches may also be an alternative, [15] proposed a model-free motion control system of a complex shaped payload using multiple lift wires using a PI (proportional-integral) controller, nevertheless, the performance obtained by implementing this control strategy still does not match the blade - hub mating tolerances.

Another model-free tugger control system is proposed in [16], where a simplified version of the model-free controller in [15] is combined with the damping tugger system in [14], resulting in a reasonable increase in performance compared to only damping control, the standard deviation of the payload's motions is reduced from 4.73m to 0.27m.

However, the performance of these two previous control systems, [15] and [16], do not meet the requirements of the blade-hub mating tolerances without counting with a primary alignment system. Furthermore, the control systems use measurements from the wire lengths, and when the accuracy of these measurements is considered, the performance of the controllers is significantly reduced.

### 1.6.2. Motion control by Stewart platform

An alternative is to eliminate the hoisting wires for the blade-hub mating phase, by directly attaching the BIT to the crane boom. Alternatives such as the boom lock, shown in Figure 1.9, have been used in jack-up installations. With this auxiliary equipment, the crane's hook is restrained by a device mounted on the boom; however, the system is not motion compensated and a shorter pendulum still remains. This solution may suffice for a jack-up WTIV but is not necessarily the case for floating installation vessels.

Nevertheless, the boom lock alternative restrains the crane's hook motion, not the payload, the slings connecting the hook to the blade still create a pendular motion. Additionally, the natural fre-

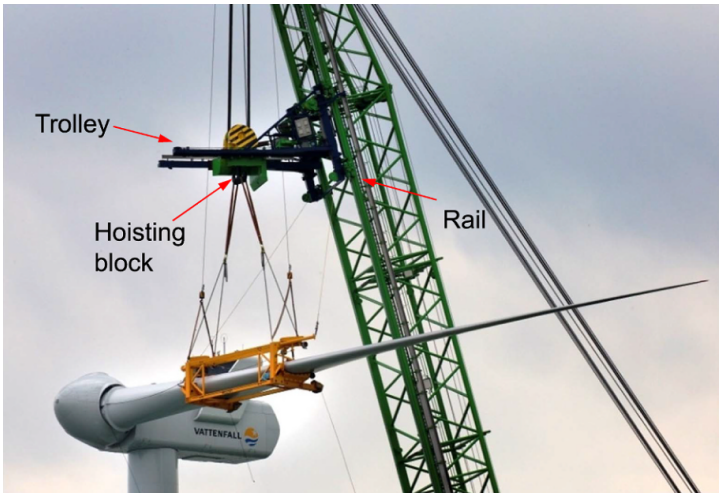


**Figure 1.9:** Boom lock [17].

quency of this pendular motion now lays in the range with wave peak frequencies; therefore, it is not a reasonable solution to be used with floating WTIV.

A solution may be to increase the system's robustness, completely removing lifting wires from the final blade installation phase. This could be achieved by implementing a motion compensated Stewart platform physically connected to the crane's boom, and controlling the BIT's motions. A schematic of the application of a Stewart platform for blade installation is presented in Figure 1.10, and a close-up representation of the system is shown in Figure 1.11.

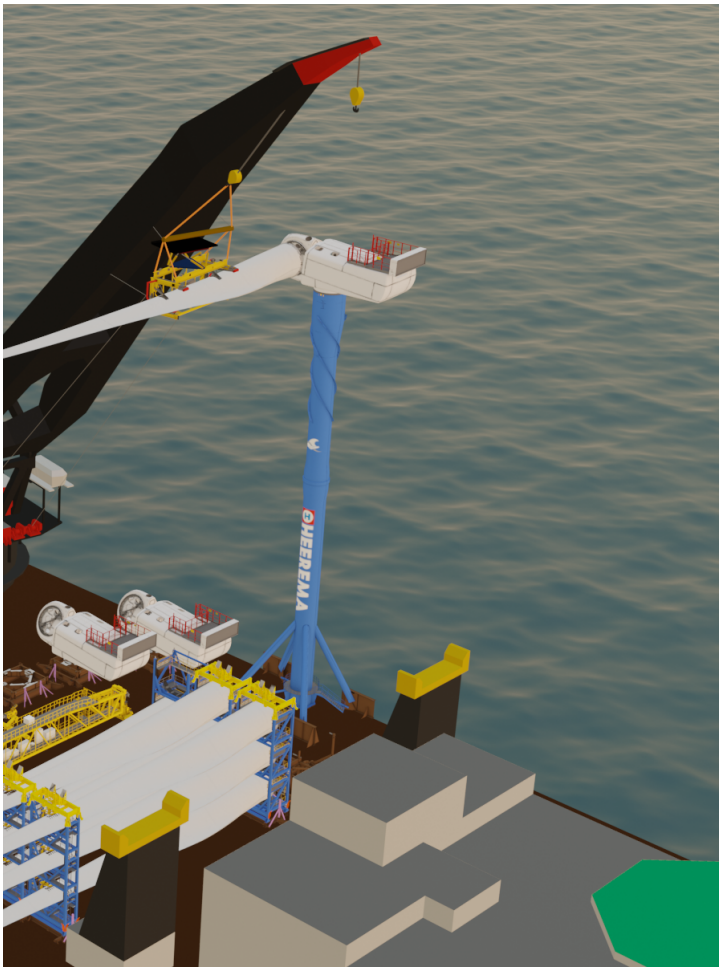


**Figure 1.10:** Representation of the GREP-less blade installation with a motion compensated Stewart platform connecting the blade / BIT to the crane's boom.

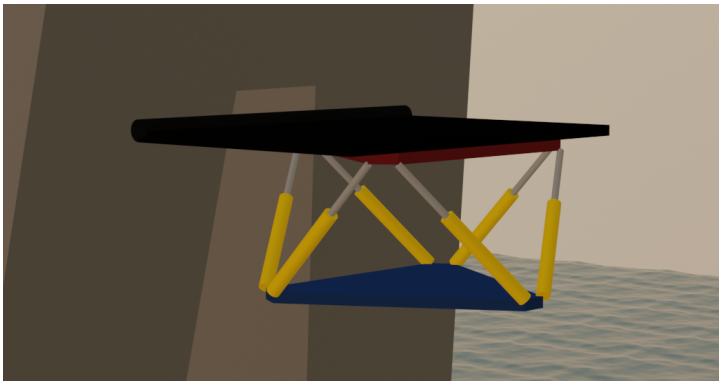

**Figure 1.11:** Close-up view of the Stewart platform to be used for blade installation.

## 1.7. Research questions and document structure

Previously developed tugger systems, both available in the industry or in the research phase, cannot compensate the motions of a wind turbine blade during installation by a floating vessel to meet the blade - hub mating tolerance without a primary alignment system; this limitation applies for the two scenarios where the blade is installed on the hub mounted on a temporary support structure on the vessel deck, and also for the blade installation on the permanent WTG support structure. Therefore,

this thesis project proposes the development of a motion compensated Stewart platform connecting the BIT and blade to the crane's boom for blade installation on the hub on top of the installation tower.

### 1.7.1. Research questions

The main research question is specified to serve as guideline for the thesis project development, as well as to address topics that are considered critical for the project's feasibility. It is presented below with the subquestions that provide extra clarity to the research.

**Research question** Is it technically feasible to use a motion compensated Stewart platform connecting the crane boom to the BIT for blade installation with the nacelle on top of the installation tower?

**Research subquestion #1** How is the performance of the motion compensated Stewart platform for blade installation affected when introducing the performance parameters of position and velocity measuring devices?

**Research subquestion #2** Given the expected influence of sensor noise in the motion control system, can compensating for relative motions in fewer degrees of freedom reduce the overall relative motions between the blade root and the hub? If not all degrees of freedom are compensated for, they are not measured; therefore, the sensors' noise is not considered for the specific degrees of freedom.

### 1.7.2. Thesis structure

The thesis is structured to provide a clear timeline for the project development, answer research questions, and summarize the project's conclusions. This report is structured as follows:

**Chapter 1** introduces the background of WTG installation with floating vessels and the Heerema Marine contractor's RNA method and the GREP tool. Moreover, provides an overview of motion compensation systems with tugger winches, and the Stewart platform as a solution for GREP-less blade installation.

**Chapter 2** provides information about the installation tower. Includes a description of the OrcaFlex model, mode analysis, and simulations to obtain the hub motions on top of the installation tower. Furthermore, the assumption that all the motions to be compensated for come from the installation tower is confirmed by calculating the crane boom stiffness and the blade static deflection.

**Chapter 3** provides a description of a general Stewart platform with a kinematic (inverse and forward) and dynamic formulation. Presents the design assumptions for the Stewart platform to be used for blade installations. The loads acting on the Stewart platform are calculated. Moreover, the Stewart platform actuators are specified and the spatial characteristics of the platform are calculated.

**Chapter 4** contains a blade installation procedure using the motion compensated Stewart platform attached to the crane's boom. Additionally, it defines the concept of the Stewart platform's main mechanical systems.

**Chapter 5** simulates different set-ups of instrumentation to measure the motions to be compensated for, and defines a final set-up and filter parameters.

**Chapter 6** presents the motion compensation control system for blade installation using the Stewart platform. The first results of the motion compensation control system are presented in this chapter.

**Chapter 7** concludes the research and provides recommendations and discussions.

**Appendix A** presents the derivation of the installation tower's equation of motion.

**Appendix B** contains the aerodynamic loads that act on the blade during the installation phase that were used to calculate the loads that act on the Stewart platform and select its actuators.

**Appendix C** provides additional results for the motion compensation system.

# 2

# Relative motions between hub and blade root

In this chapter, the possible source of the relative motions between the hub and the blade root is investigated. In the proposed method for blade installation, the nacelle is bolted to the top of the installation tower, and the blade secured by the Stewart platform attached to the portside crane boom. It is not unreasonable to consider the vessel's hull as rigid, therefore the possible source of the relative motions between the hub and the blade root are: the hub motions on top of the installation tower due to its response caused by the vessel's motions, and aerodynamic loads acting on the tower structure, nacelle, and blades connected to the hub (if any). The second possible source of relative motions between hub and blade root may originate from the free hanging length of the blade, i.e. from the BIT's face to the blade root, approximately 16 m in the case of the Vestas V174-9.5MW wind turbine blade. The third and final possible source of motions come from the crane boom stiffness, more specifically in the horizontal direction ($X - Y$ plane) where motions are expected to be larger.

These three possible sources of motion are individually assessed considering their relevance to the specific installation method being developed.

## 2.1. The Installation tower

The installation tower is one of the key elements that allows the innovative RNA installation method using a floating vessel. It is used as a temporary support structure for the nacelle and hub in order to install the blades, once all three blades are bolted to the hub, the RNA is lifted off the installation tower and placed on the wind turbine tower. Figure 2.1 depicts the RNA being lifted from the installation tower, or the RNA support tower, on the right and moved to the WTG tower on the left.

During the whole RNA installation method, one of the most critical parts is the blade installation, due to the motions involved, a restriction system such as the GREP tool or the proposed motion compensated Stewart platform must be used, either to limit the relative motions, or to compensate them. Therefore, to compensate the relative motions between the bodies, these motions need to first be modeled.

### 2.1.1. OrcaFlex model

OrcaFlex, a dynamic analysis software for offshore marine systems commonly used in the industry, is used to model the installation tower. There, the structure is modeled as a line-type element, which is flexible. The physical properties of the structure are used in the model; their values are presented in

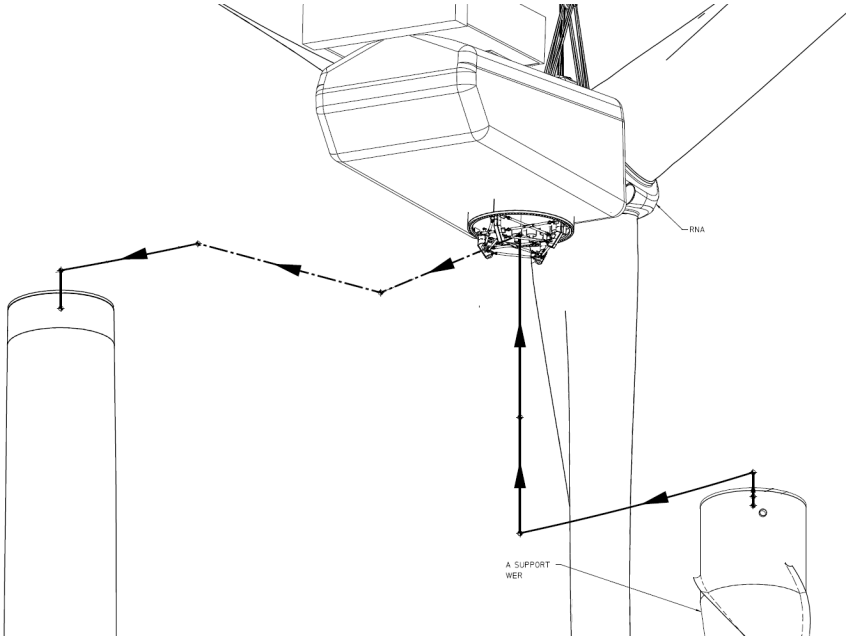


**Figure 2.1:** RNA installation by lifting it from the installation tower, or RNA support tower, and placing it on the WTG tower. Taken from [18]

Section A.3. Furthermore, the installation tower is also subject to aerodynamic loads in the OrcaFlex model, with drag coefficient $C_D = 1.2$. Structural damping is also taken into account, as the stiffness is proportional to the damping ratio of 1.0% at the response period of 0.75 seconds, the stiffness coefficient is derived in Subsection A.5.2.

The hub and nacelle are modeled as 6D buoys, i.e. rigid bodies with six degrees of freedom. Their mass properties (mass and inertia), as well as aerodynamic properties, are from the Vestas V174-9.5MW wind turbine.

Blades are modeled using the turbine section of OrcaFlex specifically designed for wind turbines. For the blades, their structural model is analogous to that of line-type elements, and they can be rigid or flexible. In the specific model, the blades connected to the hub are flexible and their structural properties come from the Vestas V174-9.5MW wind turbine.

### 2.1.2. Load cases

In order to calculate the operational requirements for the motion compensating Stewart platform for blade installation, it is necessary to know which motions the platform will have to compensate, i.e. the hub motions on the vessel reference frame. Initially, possible operational scenarios are considered:

- Nacelle and hub on top of the installation tower to receive the first blade.
- Nacelle and hub with one blade installed, in position to receive the second blade.
- Nacelle and hub with two blades installed, in position to receive the third blade.

These three possible configurations are chosen for the simulations because they represent the hub positions when blades are installed, which are the scenarios in which the Stewart platform will be used. It is important to point out that the blades are installed in the horizontal position, and consequently the possible hub orientations are fixed, that is, if there are already installed blades, their position is also predetermined. Additionally, the blades are not analyzed individually; only their influence on the hub's motions is assessed.

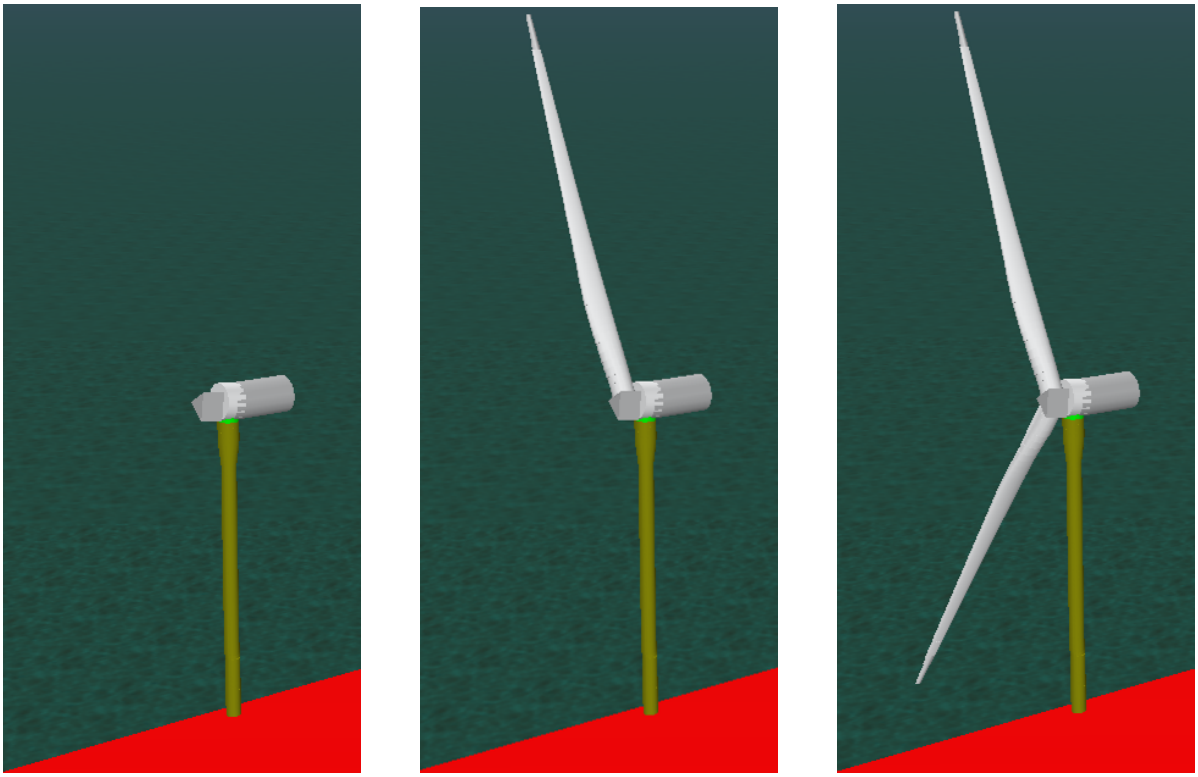

**(a)** Hub and nacelle without blades installed.

**(b)** Hub and nacelle with one blade installed.

**(c)** Hub and nacelle with two blades installed.

**Figure 2.2:** Three possible configurations of hub and nacelle for blade installation.

Having the hub, nacelle, and blade configurations defined, metocean data from different sites are analyzed to choose the weather parameters that will be used in the simulations. An important limit to be considered is the wind speed during the blade installation phase; this threshold is usually defined by the wind turbine manufacturer and considers not only the blade installation operation but also other criteria. Commonly the wind speed limit for blade installation is 12m/s at hub height. For this reason, the wind speeds chosen to define the load cases are 12 m/s and 14 m/s. The latter is specified above the common limit to test the performance of the proposed motion compensation system in more severe weather conditions.

Wind fields are generated using TurbSim from the National Renewable Energy Laboratory (NREL). The inputs for TurbSim are presented in Table 2.1 and the version used was TurbSim_v2.00.07a-bjj. The parameters for which the inputs are not defined below are the default values.

The wave parameters, significant height, and peak period are chosen to reflect a wide workability criterion in different locations around the world. First, metocean reports from three different sites are evaluated. The sites are chosen to represent locations where there is a high demand for offshore wind (Baltic Sea, North Sea, and Northeast cost of the USA). The scatter diagram of the significant wave height and peak period of these three sites, for the previously specified wind speeds, is analyzed and a value of the peak period and the significant wave height is chosen to represent more than 90% of the probability of occurrence [19] [20] [21] [22]. The peak wave period is defined as 8 seconds and a significant wave height of 2.5m. For the Orcaflex simulations, a JONSWAP wave spectrum is used in combination with a spreading exponent of 4.0 over 24 wave directions around the main wave incident direction.

The combinations of wind speed, wind direction, wave direction, as well as hub and nacelle configuration with respect to the number of blades installed are presented in Table 2.2, where the reference for wind and wave directions is represented by Figure 2.3.

**Table 2.1:** TurbSim input parameters.

| Runtime Options | | Turbine/Model Specifications | | Meteorological Boundary Conditions | |
|---|---|---|---|---|---|
| RandSeed1 | 2318573 | NumGrid_Z | 33 | UserFile | unused |
| RandSeed2 | RANLUX | NumGrid_Y | 33 | IECstandard | 3 |
| WrBHHTP | FALSE | TimeStep | 0.05 | IECturbc | B |
| WrFHHTP | FALSE | AnalysisTime | 3600 | IEC_WindType | NTM |
| WrADHH | FALSE | UsableTime | ALL | ETMc | default |
| WrADFF | TRUE | HubHt | 89.753 | ProfileType | PL |
| WrBLFF | FALSE | GridHeight | 180 | ProfileFile | unused |
| WrADTWR | FALSE | GridWidth | 270 | RefHt | 89.753 |
| WrFMTFF | FALSE | VFlowAng | 0 | URef | 12 or 14 |
| WrACT | TRUE | HFlowAng | 0 | ZJetMax | 450 |
| Clockwise | TRUE | **Meteorological Boundary Conditions** | | PLExp | 0.14 |
| ScaleIEC | 0 | TurbModel | IECKAI | Z0 | 0.0003 |

**Table 2.2:** Load cases used in the OrcaFlex simulations to obtain the hub responses. Combination of number of blades connected to the hub, wind speed and incident direction, and wave parameters (significant wave height and peak period) and its incident direction.

| Load case | Num. Blades | Vel. Wind [m/s] | Dir. Wind [°] | Hs [m] | Tp [s] | Dir. Wave [°] |
|---|---|---|---|---|---|---|
| LC 01 | 0 | 12 | 0 | 2.50 | 8 | 0 |
| LC 02 | 0 | 12 | 0 | 2.50 | 8 | -45 |
| LC 03 | 0 | 12 | -45 | 2.50 | 8 | 0 |
| LC 04 | 0 | 14 | 0 | 2.50 | 8 | 0 |
| LC 05 | 0 | 14 | 0 | 2.50 | 8 | -45 |
| LC 06 | 0 | 14 | -45 | 2.50 | 8 | 0 |
| LC 07 | 0 | 12 | 0 | 2.50 | 8 | -90 |
| LC 08 | 0 | 12 | -90 | 2.50 | 8 | 0 |
| LC 09 | 0 | 14 | 0 | 2.50 | 8 | -90 |
| LC 10 | 0 | 14 | -90 | 2.50 | 8 | 0 |
| LC 11 | 1 | 12 | 0 | 2.50 | 8 | 0 |
| LC 12 | 1 | 12 | 0 | 2.50 | 8 | -45 |
| LC 13 | 1 | 12 | -45 | 2.50 | 8 | 0 |
| LC 14 | 1 | 14 | 0 | 2.50 | 8 | 0 |
| LC 15 | 1 | 14 | 0 | 2.50 | 8 | -45 |
| LC 16 | 1 | 14 | -45 | 2.50 | 8 | 0 |
| LC 17 | 1 | 12 | 0 | 2.50 | 8 | -90 |
| LC 18 | 1 | 12 | -90 | 2.50 | 8 | 0 |
| LC 19 | 1 | 14 | 0 | 2.50 | 8 | -90 |
| LC 20 | 1 | 14 | -90 | 2.50 | 8 | 0 |
| LC 21 | 2 | 12 | 0 | 2.50 | 8 | 0 |
| LC 22 | 2 | 12 | 0 | 2.50 | 8 | -45 |
| LC 23 | 2 | 12 | -45 | 2.50 | 8 | 0 |
| LC 24 | 2 | 14 | 0 | 2.50 | 8 | 0 |
| LC 25 | 2 | 14 | 0 | 2.50 | 8 | -45 |
| LC 26 | 2 | 14 | -45 | 2.50 | 8 | 0 |
| LC 27 | 2 | 12 | 0 | 2.50 | 8 | -90 |
| LC 28 | 2 | 12 | -90 | 2.50 | 8 | 0 |
| LC 29 | 2 | 14 | 0 | 2.50 | 8 | -90 |
| LC 30 | 2 | 14 | -90 | 2.50 | 8 | 0 |

### 2.1.3. Installation tower motions

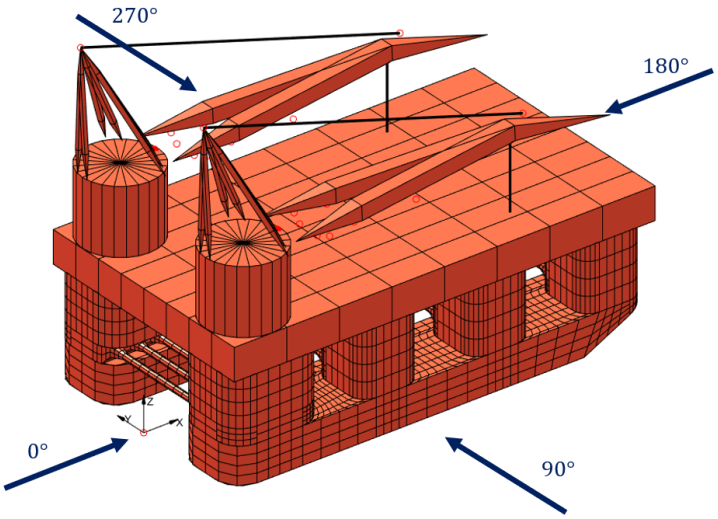


**Figure 2.3:** Incident angle definition.

Once the installation tower and wind turbine model are finalized, a modal analysis is performed in OrcaFlex to identify the excitation modes and their corresponding natural frequency and period. A list of natural frequencies and periods is presented in Table 2.3 for the three possible blade installation configurations (0 blades installed, 1 blade installed, and 2 blades installed in the hub).

**Table 2.3:** Natural frequencies and periods of the installation tower.

| Config. | Mode number | 1 | 2 | 3 | 4 |
|---|---|---|---|---|---|
| 0 Blade | Period (s) | 2.7064 | 2.673 | 0.5842 | 0.3096 |
| | Frequency (Hz) | 0.3695 | 0.3741 | 1.7119 | 3.2304 |
| 1 Blade | Period (s) | 3.0006 | 2.9837 | 0.945 | 0.9048 |
| | Frequency (Hz) | 0.3333 | 0.3352 | 1.0582 | 1.1052 |
| 2 Blades | Period (s) | 3.0598 | 3.0361 | 1.0591 | 0.9683 |
| | Frequency (Hz) | 0.3268 | 0.3294 | 0.9442 | 1.0328 |

The modes presented in Table 2.3 do not represent all modes, but those with the lowest natural frequencies, those that may be excited by external loads and the response of the vessel.

Next, with the load cases defined, Orcaflex implicit time domain simulations are carried on to calculate the hub motions that result from the aerodynamic loads acting on the installation tower, nacelle, hub, blades connected to the hub, and the vessel's response to the waves that are transmitted to the installation tower. The simulations have a duration of one hour (3600 seconds), with 600 seconds of ramp up. Once the simulations have been completed, six time series of the response of the hub are generated, one per degree of freedom ($x$, $y$, $z$, rotation about the $x-$ axis, rotation about the $y-$ axis and rotation about the $z-$ axis). In the hub motions time series, the vessel motions are properly subtracted such that the results of hub motions analyzed are centered in the hub reference frame.

The maximum and minimum double amplitude (maximum response value minus minimum response value) of each degree of freedom is calculated, and their corresponding load case is presented. From these values detailed in Table 2.4, it is possible to notice that the overall response of the hub is small, nevertheless, it is enough to cause significant relative motions not allowing the blade - hub connection if they are not compensated.

The time series of the hub response is used to calculate the power spectrum density (PSD) of each response. PSDs allow us to identify which frequencies cause the largest responses. Figure 2.4

**Table 2.4:** Largest and smallest double amplitude of the hub's responses and their corresponding load cases.

| Degree of freedom | Max. double amplitude | Load case | Min. double amplitude | Load case |
|---|---|---|---|---|
| x [mm] | 194.6 | 19 | 70.0 | 9 |
| y [mm] | 227.0 | 29 | 115.0 | 2 |
| z [mm] | 73.9 | 16 | 25.8 | 10 |
| Rotation x [°] | 0.342 | 29 | 0.069 | 1 |
| Rotation y [°] | 0.188 | 16 | 0.116 | 9 |
| Rotation z [°] | 0.089 | 29 | 0.021 | 1 |

presents the time series and PSD of the response of the hub in load case 16. There, it becomes clear that the hub response results not only in the same frequencies of the external loads (wind and wave), but also in the system's natural frequencies. Although all degrees of freedom have a high response around the wave's peak period (8 seconds, 0.125Hz), $y-$ hub motions, as well as rotations about the $x-$ and $z-$ axis, are highly influenced by the wind's low frequency. Furthermore, a high response can be observed near the first and second natural frequencies at all degrees of freedom ( 0.33Hz). And, as expected, rotation about the $z-$ axis also has a peak around the third and fourth natural frequencies ( 1.10Hz).

Analyzing the results of the other 29 simulations, it can be observed that the degrees of freedom with high responses in the wind frequency are related to the wind's incident direction, i.e., in which degree of freedom the wind loads contribute the most. Nevertheless, it is possible to observe that significant responses in the different degrees of freedom can be observed at wave and wind frequencies, and first and second natural frequencies of the system. Specifically for rotation about the $z-$ axis where one or two blades are already installed, a significant response can be observed at frequencies near 1Hz, i.e., third and fourth natural frequencies for the configuration with one blade, and third until fifth natural frequencies for the configuration with two blades installed.

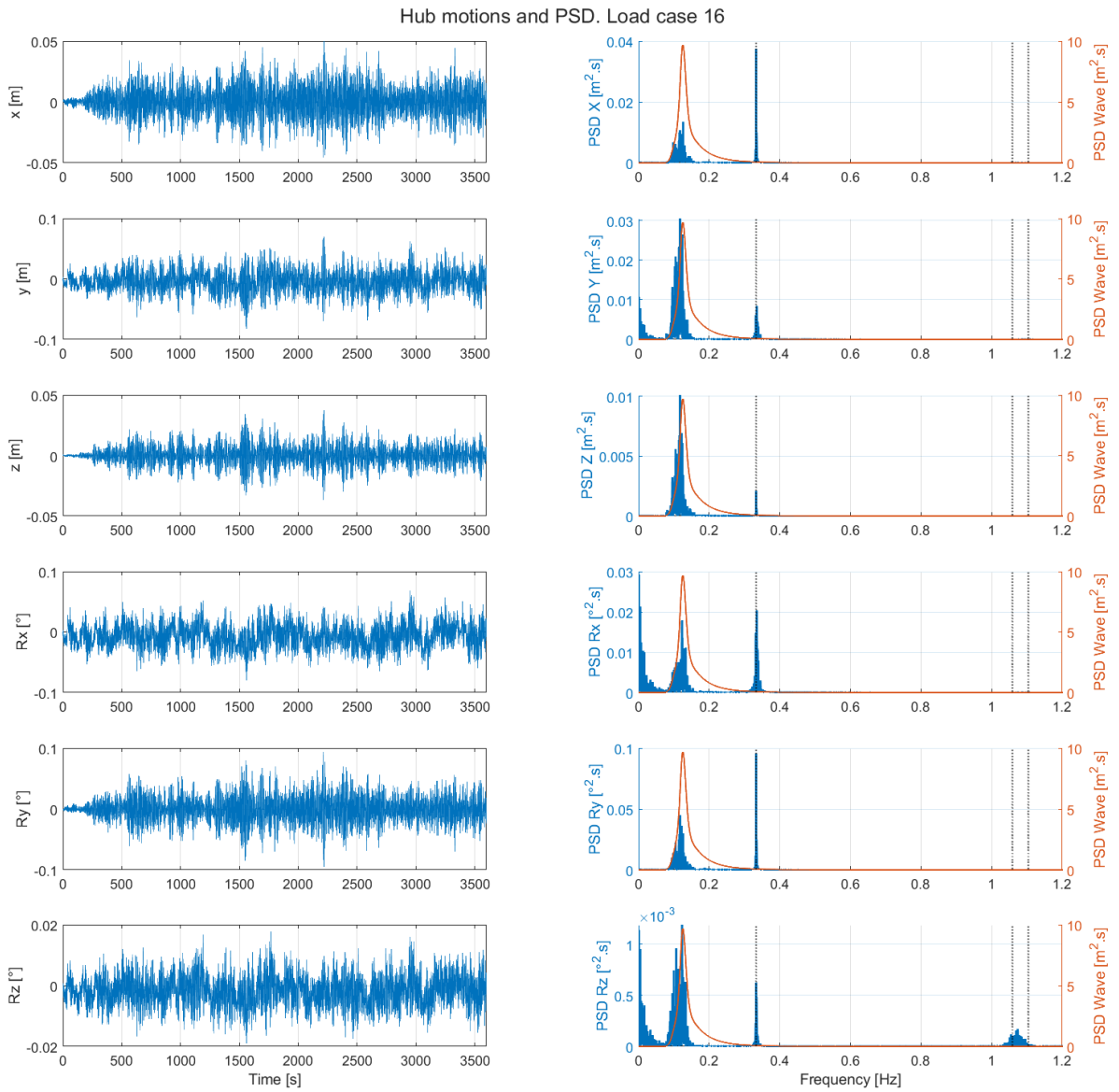


**Figure 2.4:** Time series and PSD of the hub's 6 degrees of freedom - Load case 16. The orange line is the wave spectrum, and the vertical dashed black lines are the corresponding natural frequencies.

## 2.2. Blade deflection

During the blade installation process, the BIT is used to lift and hold the blade. The tool clamps the blade in two points that envelope its CoG. Therefore, the blade can be considered as two independent clamped beams, one from the BIT to the blade's tip, and the second one from the BIT to the blade's root. This allows for the calculation of the blade's deflection under its own weight for the part of interest, the one for which the motions must be compensated for, i.e. the part of the blade from the BIT until its root. The main purpose of this analysis is to verify if this length of the blade can be considered as a rigid body or if its flexibility must be taken into account.

To calculate the blade deflection due to its own weight between the BIT and the root, the distributed mass of the blade, Figure 2.5, is used to calculate the internal forces acting on the blade, force and moment. The internal moment on each node is used to calculate the curvature of the blade, the bending angle, and finally the deflection of the blade using the classical beam theory.

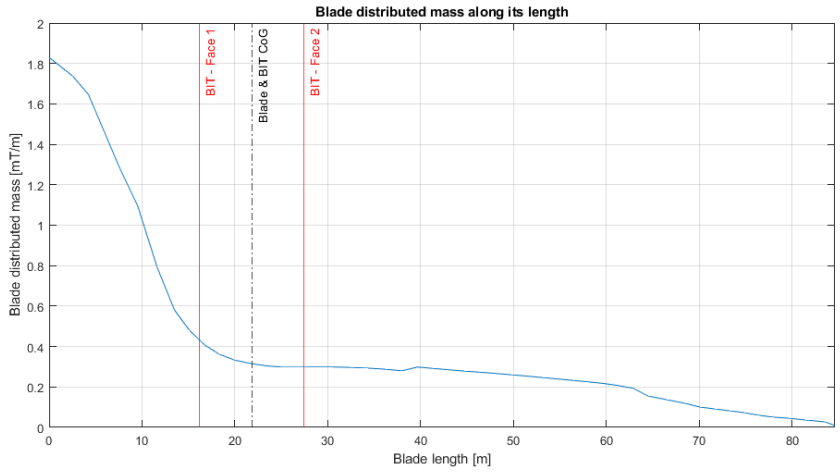


**Figure 2.5:** Blade distributed mass in metric tonnes per meter as a function of the blade length.

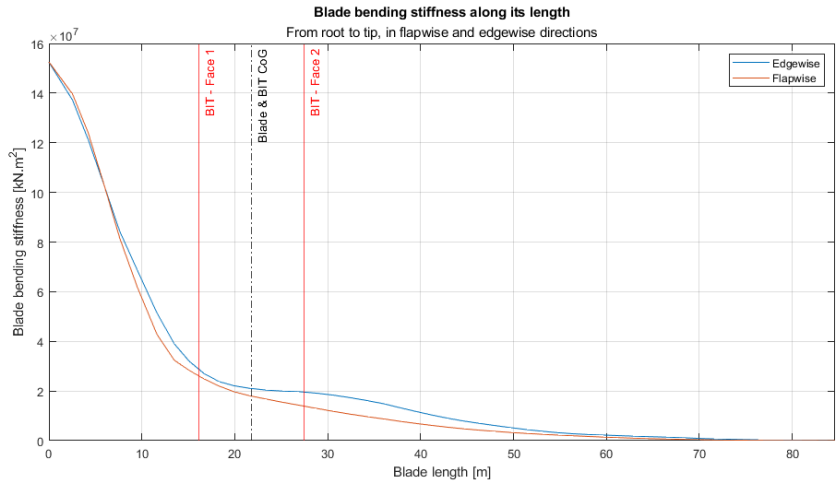


**Figure 2.6:** Blade bending stiffness in edgewise and flapwise directions as a function of the blade length.

Although most of the blade's mass is concentrated near the root, this length of the blade is also where it is the most stiff, thus, in practical terms, the most important factor is the lever arm, i.e. the distance between the BIT and the blade's root. It is important to note that this parameter is directly related to the blade mass distribution, GoG, and total length. Combining all the required information, the static deflection of the blade under its own weight is calculated and presented in Figure 2.7. The maximum blade root deflection is obtained, as expected, in the flapwise direction, with a value of -0.47 mm. Flapwise direction here is used to represent the blade's local $z-$ direction and considering the blade's structural twist. Analogously, edgewise direction represents the local $y-$ direction of the blade, also considering its structural twist.

Considering only the blade's distributed mass to calculate the deflection at the root may be misleading because the aerodynamic loads and vessel motions transmitted to the blade are not considered. Initially the vessel's motions will not be considered due to the small response that a semi-submersible vessel presents in normal operation weather conditions. The aerodynamic loads that act on the blade are calculated using the cross-flow principle and are presented in Appendix B. It is important to point out that in the cross-flow principle, the resulting drag force is the one that will contribute to the blade's horizontal deflection, while the lift force will be responsible for the vertical deflection of the blade. Figure B.7 present the aerodynamic forces that act on the entire blade in two different angles of attack, one that creates the highest lifting force and the other responsible for the highest drag force. When these

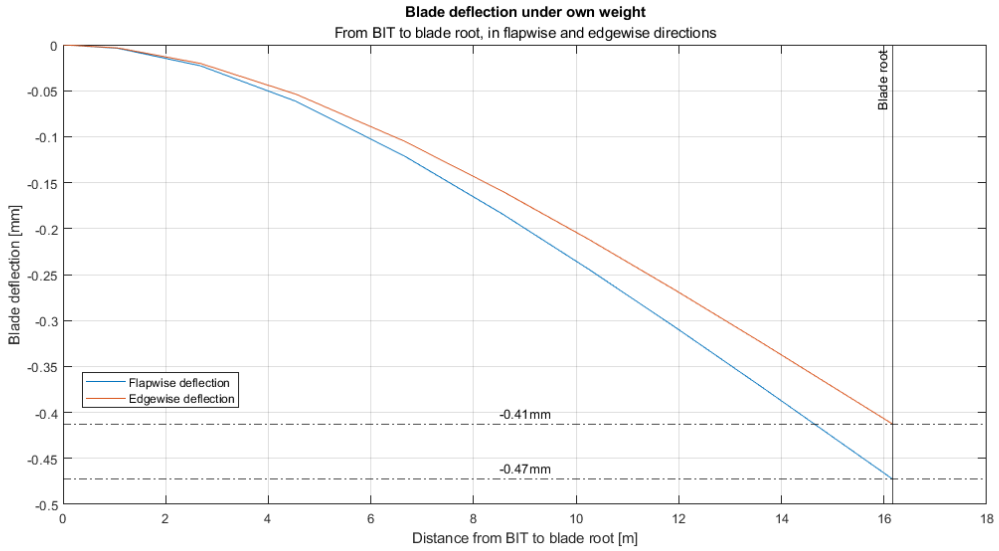


**Figure 2.7:** Blade static deflection under own weight from the BIT until the root in flapwise and edgewise directions.

aerodynamic loads are compared to the weight of the blades themselves, it is possible to conclude that their influence on the deflection of the blade root will be negligible.

When the blade root deflection is calculated to be less than 0.5 mm under the considerable load that is the blade's own weight, it becomes clear that the length of the blade between the BIT and the root can be considered a rigid body.

## 2.3. Crane boom stiffness

One of the important parameters that must be evaluated to implement the proposed motion-compensated Stewart platform is the stiffness of the crane boom. As the Stewart platform is attached to the crane's boom, if the boom's deflection is significant due to the loads acting on it, it must be considered in the project. However, the importance of crane stiffness must be evaluated based on its contribution to relative motions between the blade and the nacelle & hub on top of the installation tower, that is, the stiffness of the crane must be compared to the stiffness of the installation tower in the same direction, that is, in the radial direction of the crane and the bending direction of the installation tower (local $x-$ and $y-$).

In regular lifting operations, there are four main components of the crane that influence its overall stiffness, the boom, A-frame, derrick wires, and the hoist wires [23]. Nevertheless, for the application with the Stewart platform, the hoist wire is not used, therefore, its contribution to the crane's stiffness must not be taken into account. The three main components that contribute to the stiffness of the crane are highlighted in Figure 2.8, where the boom is colored orange, the A frame blue, and the derrick wires are colored green.

From Figure 2.8 it is also possible to notice that the stiffness of the crane will be a function of its working radius, as the boom is lowered, the forces and directions acting on the boom itself, on the A frame and on the derrick wires change, thus changing the overall stiffness of the crane as a function of the working radius. Thus, the total stiffness of the crane in all directions for the application with the Stewart platform can be formulated as [23]:

$$K_{\text{Crane}} = \left( \frac{1}{K_{\text{Boom}}} + \frac{1}{K_{\text{Derrick}}} + \frac{1}{K_{\text{A-frame}}} \right)^{-1} \tag{2.1}$$

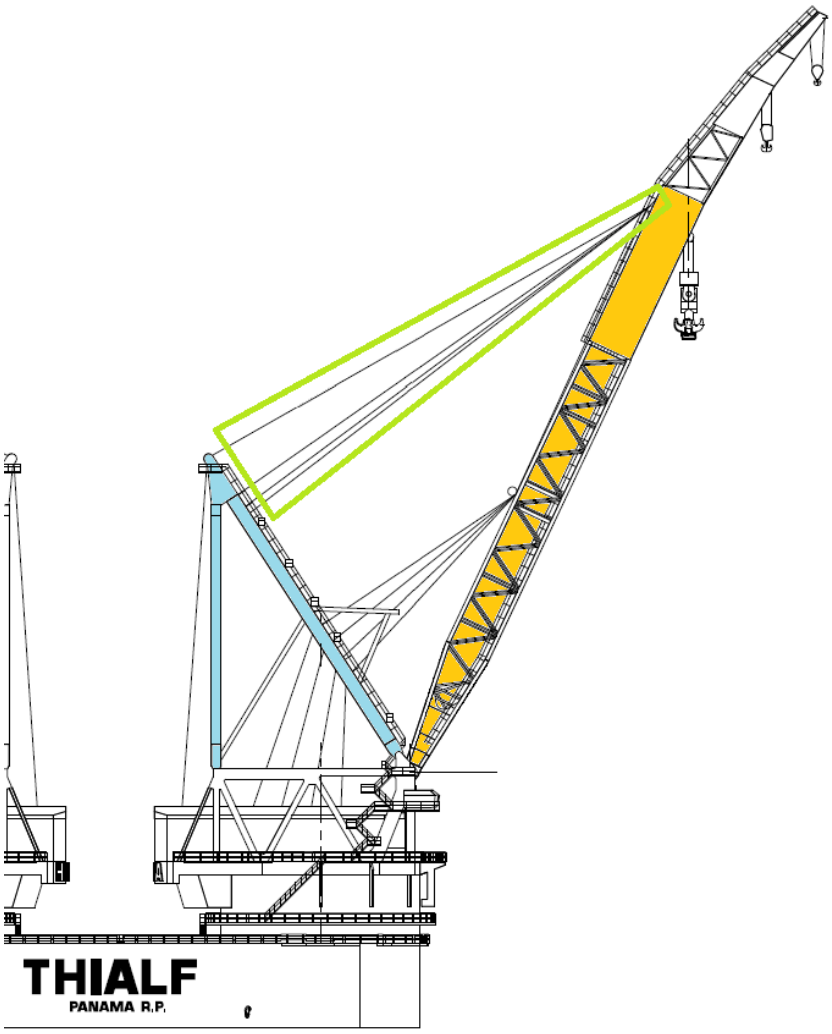


**Figure 2.8:** Components of the crane influencing its stiffness.

Where $K_{\text{Boom}}$ is the stiffness of the boom, $K_{\text{Derrick}}$ is the stiffness of the derrick wires, and $K_{\text{A-frame}}$ is the stiffness of the crane's A-frame. These parameters are provided by the crane manufacturer as the displacement resulting from an applied force, that is, in units of force per length [23].

Because of the form in which the crane stiffness is calculated, an equivalent stiffness for the installation tower has to be calculated in order to provide a stiffness that is comparable to the crane's. Thus, the stiffness is expressed in units of force per length.

To calculate the equivalent stiffness of the installation tower in unit force per length, a point force $F$ is applied to the top of the installation tower to create a virtual static deflection, resulting in an internal bending moment of:

$$M(z) = F(L - z)$$

Where $F$ is the force applied to the top of the tower, $L$ is the height of the tower, and $M$ is the moment generated by the force $F$. From the Euler-Bernoulli beam theory, the internal bending moment is:

$$M = -EI\frac{\partial^2 u}{\partial z^2}$$

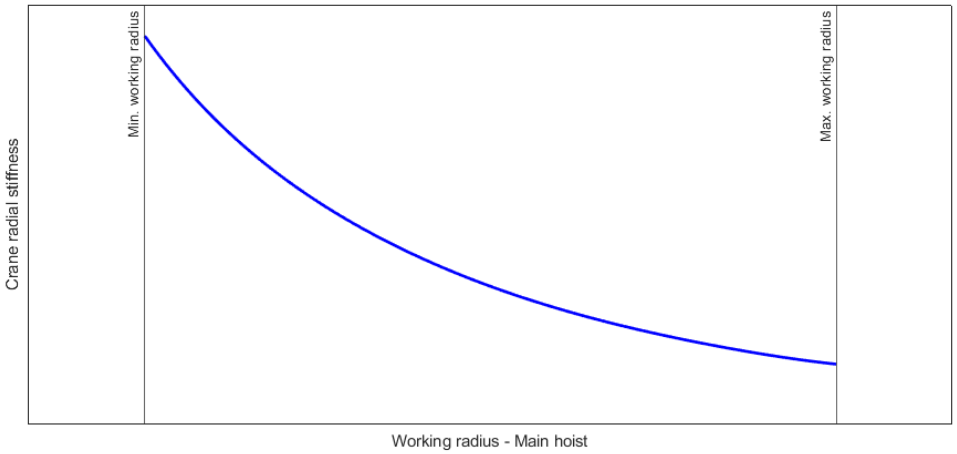


**Figure 2.9:** Crane's stiffness as a function of the main hoist working radius, parameters taken from [23].

Where $E$ is the Young modulus, $I$ is the moment of inertia of the cross section, and $u$ is the deflection along the tower's $z-$ axis. Although the installation tower is 65.00m tall, it is clamped at 13.08m above the deck level, as depicted in Appendix A, so $L$ =51.92 m. Additionally, because the installation tower is clamped at its base, $u(z=0) = \partial u/\partial z|_{z=0} = 0$. The moment can now be integrated twice with respect to $z$ to result in static displacement on top of the installation tower $(z = L)$.

$$K_{\text{installation Tower}} = \frac{F}{u(z)} = \frac{2EI}{\left(Lz^2 - \frac{L^3}{3}\right)} \tag{2.2}$$

For $z = L$ =51.92 m and using the constant equivalent stiffness of the installation tower, $EI$, in Appendix A,
$\mathbf{K}_{\text{installation Tower}} = \mathbf{3.11}$kN/mm.

As a reference, for the installation tower configuration used in the Arcadis Ost 1 project, the Stewart platform would be placed approximately 90% of the boom length of the crane (main hoist) from its foot, resulting in a working radius that produces a crane stiffness in its radial direction of approximately **12 times** the equivalent stiffness of the installation tower. It is important to point out that the taller the installation tower, the lower its stiffness and the higher the crane stiffness due to the reduction in the working radius. Similarly, if the installation tower is positioned closer to the crane's pedestal, the latter's stiffness will increase also due to reduction of working radius (installation tower's stiffness remains unchanged); the opposite happens if the tower is moved further away from the crane's pedestal.

When considering the crane's overall stiffness, the tangential direction shall also be assessed, i.e. the direction in which the crane slews. To do so, it is important to identify the loads acting in that direction, which are aerodynamic, inertia, and loads transmitted from the payload (blade attached to the boom). Another possible source of motions in the tangential direction is mechanical play between the slewing gears; nevertheless, the vessel's cranes' slewing motors maintain a counter torque to eliminate the mechanical loose from the slewing gears and to have an influence in the crane boom's motions. Regarding the aerodynamic loads on the crane's boom, they are minimal due to the trussed nature of the boom, the aerodynamic drag is kept to a minimum, and its influence can be neglected. The loads transmitted to the boom by the payload will also have a small influence on the boom's deflection due to its rectangular shape with widest side in the tangential direction, as well as small loads transmitted to the boom compared to the crane's rated capacity of 7100mT. Finally, the influence of inertia loads can be neglected due to small accelerations in regular operational environmental conditions. Therefore, it is possible to conclude that crane boom motions in the tangential direction may be neglected, not only due to the structural characteristics of the crane, but also due to the small magnitudes of the loads

acting in this direction.

From the figures presented in this section, it is possible to conclude that the crane's boom can be considered as a rigid body when compared to the installation tower with its flexibility taken into account in the model.

## 2.4. Source of relative motions between hub and blade root

The possible source of relative motions between the blade root and hub is assessed in the previous sections of this chapter. It is concluded that the crane stiffness under the blade installation scenario is considerably higher than the one of the installation tower, therefore the former can be neglected.

Furthermore, the blade deflection is analyzed for the length between the BIT and the blade root. Although being the blade section with the highest distributed mass, it is also the stiffest section. When combined with its short length, the blade deflection can be neglected compared to the hub motions.

From the analysis of the installation tower, crane boom and blade deflection, it is concluded that the only relevant source of motions between the hub and the blade root originates from the installation tower response.

# 3

# The Stewart platform

The Stewart platform, first proposed in 1965 [13], is a parallel mechanism consisting of a base and a platform connected by a set of actuators. Most commonly, Stewart platforms have a 6-by-6 configuration, that is, the base structure is connected to the platform structure by six actuators in six joints, where each actuator is attached to the base and platform at different and individual points, as depicted in Figure 3.1.

One of the advantages of a 6-by-6 configuration is the precision to control all six degrees of freedom of the platform, with respect to the base, by controlling the actuators' (legs) lengths, and with few singularity points. Amongst others, these are some of the reasons why the Stewart platform is used in complex and demanding applications, from flight simulators to motion compensated access systems in the offshore environment.

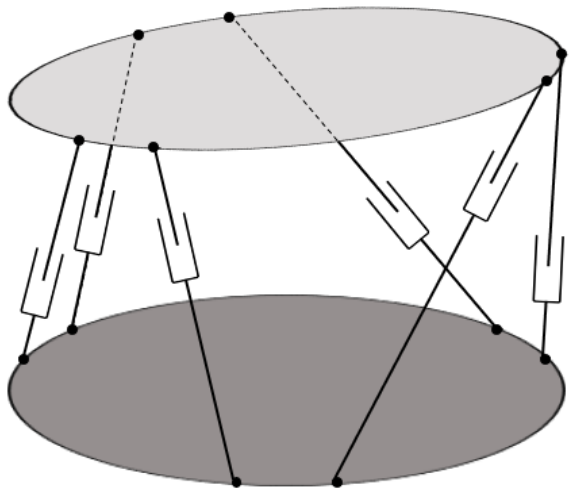

**Figure 3.1:** Stewart platform schematic. Base represented in dark grey (bottom) and platform in light grey (top).

## 3.1. Kinematic formulation of the Stewart platform

To control the blade root motions and make it (nearly) motionless relative to the hub, the controllable element of the Stewart platform is used; therefore, the kinematics of the mechanism must be formulated. The kinematic formulation of the Stewart platform behavior can be done in two different ways, forward and inverse kinematics. The inverse kinematic problem calculates the actuators' lengths

based on a given platform position and orientation. On the other hand, the forward kinematic problem calculates the position and orientation of the platform, with respect to the base, from the length of the actuators. The approaches are described in the following sections.

In the formulation of the Stewart platform equations, matrices and vectors are represented with bold letters from the Greek or Latin alphabet (**A** or **a**) and scalar quantities are represented with regular letters from the Greek or Latin alphabet ($\delta$ or $\Delta$). The system's reference system is defined in Figure 3.2. In Figure 3.2a, $O_V$ represents the origin of the external reference system, that is, the vessel's reference system, $O_B$ and $O_P$ are, respectively, the origin of the local base and platform reference systems. Each of these reference systems has its own orthogonal $x-y-z$ axis. Figure 3.2b shows the relevant vectors used in the kinematic and dynamic formulation of the Stewart platform's behavior. The joint vectors of both base and platform in their respective reference systems are defined as $\mathbf{B_{B,i}}$ and $\mathbf{P_{P,i}}$, i.e. base's and platform's $i^{\text{th}}$ joint vector in their respective reference system. The platform's and base's joint vectors can also be written in the vessel reference system, respectively $\mathbf{P_{V,i}}$ and $\mathbf{B_{V,i}}$. The vector $\mathbf{S_{V,i}}$ denotes the actuator vector in the reference system of the vessel. The position of $O_P$ and $O_B$ in the vessel reference system is indicated by $\mathbf{T_{V2P}}$ and $\mathbf{T_{V2B}}$, respectively. Finally, the vectors $\mathbf{X_{P1V}}$ and $\mathbf{X_{B1V}}$ denote the position and orientation of the platform's and base's reference system relative to $O_V$.

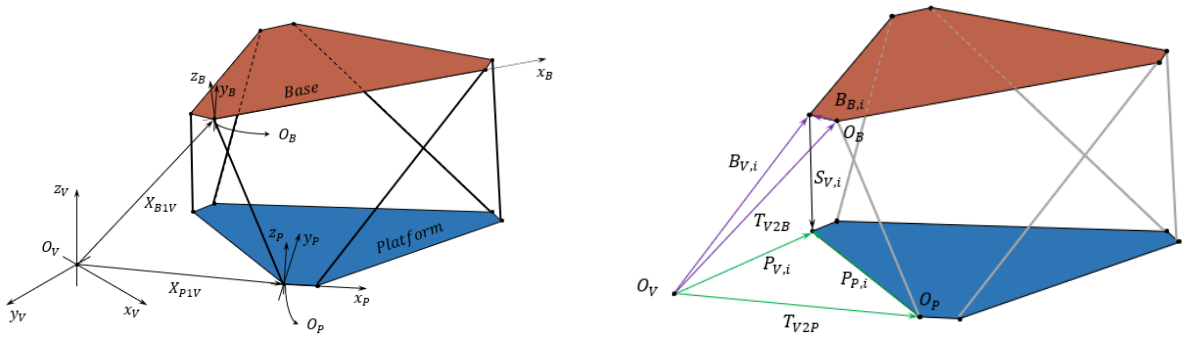


**(a)** Coordinate system.

**(b)** Relevant vectors.

**Figure 3.2:** Stewart's platform coordinate system and relevant vectors for the kinematic formulation.

### 3.1.1. Inverse kinematics

The inverse kinematic formulation of the Stewart platform calculates the actuators lengths and velocities required to compensate the motions between the hub on top of the installation tower and the blade root that is controlled by the Stewart platform, that is, given the position and orientation of the platform, the actuators lengths are calculated. Therefore, the goal is to determine the required actuator operational parameters (length and velocity) so that the blade root follows the hub.

Both the platform and the base have their own reference system, as depicted in Figure 3.2a, when using the reference system of the platform, the subscript $_P$ will be used, while for the base, the subscript $_B$ is used. When referring to one object in a different reference system, for example referring to the base in the vessel reference system, the following notation is used: $\mathbf{X}_{B1V}$, meaning "base in the vessel reference system". Analogously, when describing a vector from one object or reference system to another, the following notation is used: $\mathbf{T}_{V2P}$, which means the translation vector from the origin of the reference system of the vessel to the origin of the reference system of the platform. Vectors **T** are used to represent the position between two objects, or reference systems, for example, $\mathbf{T}_{V2B}$ represents the base position relative to the vessel reference system, as depicted in Figure 3.2b, and vectors $\phi_{V2B}$ represent the orientation of the base reference system relative to the vessel reference system. Therefore, the position and orientation of one object or reference system relative to another is written as:

$$\mathbf{T} = \begin{bmatrix} T_x & T_y & T_z \end{bmatrix} \tag{3.1a}$$

$$\phi = \begin{bmatrix} \alpha & \beta & \gamma \end{bmatrix} \tag{3.1b}$$

$$\mathbf{X} = \begin{bmatrix} \mathbf{T} & \phi \end{bmatrix} = \begin{bmatrix} T_x & T_y & T_z & \alpha & \beta & \gamma \end{bmatrix} \tag{3.1c}$$

From the orientation between two reference systems, the Euler transformation matrices can be derived:

$$\mathbf{R}_x(\alpha) = \begin{bmatrix} 1 & 0 & 0 \\ 0 & \cos\alpha & \sin\alpha \\ 0 & -\sin\alpha & \cos\alpha \end{bmatrix} \tag{3.2a}$$

$$\mathbf{R}_y(\beta) = \begin{bmatrix} \cos\beta & 0 & -\sin\beta \\ 0 & 1 & 0 \\ \sin\beta & 0 & \cos\beta \end{bmatrix} \tag{3.2b}$$

$$\mathbf{R}_z(\gamma) = \begin{bmatrix} \cos\gamma & \sin\gamma & 0 \\ -\sin\gamma & \cos\gamma & 0 \\ 0 & 0 & 1 \end{bmatrix} \tag{3.2c}$$

The rotation matrices, Equation 3.2, are now combined to describe the rotation matrix between two reference systems.

$$\mathbf{R} = \mathbf{R}_z(\gamma)\mathbf{R}_y(\beta)\mathbf{R}_x(\alpha) = \begin{bmatrix} \cos\gamma\cos\beta & -\sin\gamma\cos\alpha + \cos\gamma\sin\beta\sin\alpha & \sin\gamma\sin\alpha + \cos\gamma\cos\alpha\sin\beta \\ \sin\gamma\cos\beta & \cos\gamma\cos\alpha + \sin\alpha\sin\beta\sin\gamma & -\cos\gamma\sin\alpha + \sin\gamma\cos\alpha\sin\beta \\ -\sin\beta & \cos\beta\sin\alpha & \cos\beta\cos\alpha \end{bmatrix} \tag{3.3}$$

Mathematically, actuators can be defined as vectors for their lengths to be calculated such that the leg vectors are the difference between the base and platform joint vectors. Nevertheless, it is not possible to proceed with this operation if all the elements are not in the same reference system. Therefore, a common reference system must be chosen. For simplicity, the vessel reference system is chosen and, as a consequence, the base and platform are defined in the vessel reference system:

$$\mathbf{P}_{V,i} = \mathbf{R}_{V2P}\mathbf{P}_{P,i} + \mathbf{T}_{V2P} \tag{3.4}$$

Where $\mathbf{P}_{V,i}$ is the platform's $i^{th}$ joint vector in the vessel reference system, $\mathbf{R}_{V2P}$ is the rotation matrix from the platform to the reference system of the vessel, $\mathbf{P}_{P,i}$ is the platform's $i^{th}$ joint vector in the platform's reference system, and $\mathbf{T}_{V2P}$ is the position of the platform in the reference system of the vessel. And analogously, the base joint vectors are also defined in the vessel reference system:

$$\mathbf{B}_{V,i} = \mathbf{R}_{V2B}\mathbf{B}_{B,i} + \mathbf{T}_{V2B} \tag{3.5}$$

With the base and platform joint vectors defined in the vessel reference system, the leg vectors can also be calculated, where $\mathbf{S_{V,i}}$ is the $i^{th}$ leg vector in the vessel reference system.

$$\mathbf{S_{V,i}} = \mathbf{P_{V,i}} - \mathbf{B_{V,i}} \tag{3.6}$$

Then, the length of the legs, $\sigma_i$, can be calculated taking the norm of the vector $\mathbf{S_{V,i}}$:

$$\sigma_i = \|\mathbf{S_{V,i}}\| = \sqrt{\mathbf{S_{V,i}} \cdot \mathbf{S_{V,i}}} \tag{3.7}$$

Knowing the leg vectors and their lengths, we introduce the moment vectors $\mathbf{M'_{V,i}}$. Moment vectors are vectors with origin at the origin of the reference system and perpendicular to the plane formed by the vectors $\mathbf{P_{V,i}}$ and $\mathbf{B_{V,i}}$, i.e., it is the moment of the vector $\mathbf{S_{V,i}}$ about the origin of the chosen reference

system, in this case the vessel's.

$$\mathbf{M'_{V,i}} = \mathbf{B_{V,i}} \times \mathbf{P_{V,i}} = \mathbf{B_{V,i}} \times \mathbf{S_{V,i}} = \mathbf{P_{V,i}} \times \mathbf{S_{V,i}} \tag{3.8}$$

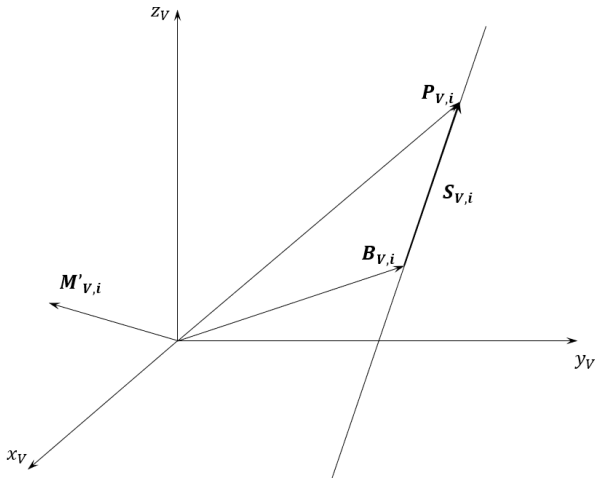


**Figure 3.3:** Representation of leg and moment vectors.

The leg and moment vectors, $\mathbf{S_{V,i}}$ and $\mathbf{M'_{V,i}}$, are normalized with respect to the lengths of the legs, and later used to formulate the normalized vector of the Plücker coordinates ($\mathbf{U_{V,i}}$), which is used in the dynamic formulation of the Stewart platform:

$$\mathbf{s_{V,i}} = \frac{\mathbf{S_{V,i}}}{\sigma_i}$$

$$\mathbf{M_{V,i}} = \frac{\mathbf{M'_{V,i}}}{\sigma_i}$$

$$\mathbf{U_{V,i}} = [s_{Vx,i} \quad s_{Vy,i} \quad s_{Vz,i} \quad M_{Vx,i} \quad M_{Vy,i} \quad M_{Vz,i}] \tag{3.10}$$

## 3.1.2. Forward kinematics

The forward kinematics formulation allows one to calculate the platform's position and orientation, with respect to the base, by using the actuators' lengths. This problem has no known closed-form solution for the most general 6-by-6 configuration. [24] used algebraic elimination to solve the forward kinematic problem, but the proposed method yields 40 possible solutions, real and imaginary, from which only one is the physically correct one. [25] made use of optimization functions and adaptations, such as the position of the origins of the reference systems, to reduce the number of solutions and improve the forward kinematics solution method. The forward kinematics problem can be analytically described by combining Equations 3.4 - 3.7, resulting in the following equation:

$$\sigma_i^2 = \|\mathbf{P_{V,i}} - \mathbf{B_{V,i}}\|^2 = \|\mathbf{R}_{V2P}\mathbf{P}_{P,i} + \mathbf{T}_{V2P} - \mathbf{R}_{V2B}\mathbf{B}_{B,i} - \mathbf{T}_{V2B}\|^2 \tag{3.11}$$

Here, the $i$ index represents the $i^{th}$ leg. To simplify the forward kinematics problem, some properties of the rotation matrix are used. For clarity, the rotation matrix, Equation 3.3, is written as follows:

$$\mathbf{R} = \begin{bmatrix} \mathbf{n} & \mathbf{o} & \mathbf{a} \end{bmatrix} = \begin{bmatrix} n_x & o_x & a_x \\ n_y & o_y & a_y \\ n_z & o_z & a_z \end{bmatrix} \tag{3.12}$$

The way in which the elements of the rotation matrix are interdependent is the following way:

$$\mathbf{n} \cdot \mathbf{n} = n_x^2 + n_y^2 + n_z^2 = 1 \tag{3.13a}$$

$$\mathbf{o} \cdot \mathbf{o} = o_x^2 + o_y^2 + o_z^2 = 1 \tag{3.13b}$$

$$\mathbf{n} \cdot \mathbf{o} = n_x o_x + n_y o_y + n_z o_z = 0 \tag{3.13c}$$

$$\mathbf{a} = \mathbf{n} \times \mathbf{o} \tag{3.13d}$$

Furthermore, without loss of generality as previously described, the base and platform coordinate systems are defined such that $\mathbf{B_{B,1}} = [0, 0, 0]$, $B_{By,2} = 0$, $\mathbf{P_{P,1}} = [0, 0, 0]$ and $P_{Py,2} = 0$.

These series of simplifications and properties reduce the problem to nine equations and nine unknowns, where the unknowns are the platform position with respect to the base (3 unknowns), and the vectors **n** and **o** from the rotation matrix. Once all the unknowns are calculated, the vector **a** of the rotation matrix is calculated from the cross product of **n** and **o**. Next, the Euler angles can be calculated from the rotation matrix knowing that the latter is $\mathbf{R} = \mathbf{R}_z(\gamma)\mathbf{R}_y(\beta)\mathbf{R}_x(\alpha)$.

It is important to note that the proposed system of nine unknowns and nine equations does not have an analytical single solution; therefore, a numerical method of choice must be used. [25] suggested the implementation of the Newton-Rapson method and showed that the proposed approach provides fast and precise solutions. However, it should be noted that the initial guess and numerical parameters used in the Newton-Rapson method determine the accuracy of the result and how fast it converges; therefore, they must be carefully selected.

## 3.2. Jacobian

The Jacobian matrix is used to map active joint velocities to end-effector velocity, and because of the constraint between actuator velocities and base and platform velocities, the Jacobian matrix can be used to calculate the former.

In the proposed use of the Stewart platform for blade installation, the base remains fixed in the inertial reference frame, i.e. the base, attached to the crane's boom, is fixed in the vessel's reference frame. Therefore, the Jacobian can be defined as follows [26]:

$$\mathbf{J} = \begin{bmatrix} \mathbf{s_{V,1}} & (\mathbf{R_{P2B}P_{V,1}} \times \mathbf{s_{V,1}})^T \\ \vdots & \vdots \\ \mathbf{s_{V,6}} & (\mathbf{R_{P2B}P_{V,6}} \times \mathbf{s_{V,6}})^T \end{bmatrix} \tag{3.14}$$

And from the Jacobian, the actuators' velocities are calculated [27]:

$$\dot{\sigma} = \mathbf{J}\left(\dot{\mathbf{X}}_{P1V} - \dot{\mathbf{X}}_{B1V}\right) \tag{3.15}$$

Where $\dot{\sigma}$ is the vector that contains the velocity of the six actuators, $\dot{\mathbf{X}}_{P1V}$ is the vector with the linear and angular velocities of the platform in the reference system of the vessel, and $\dot{\mathbf{X}}_{B1V}$ is the vector with the linear and angular velocities of the base in the reference frame of the vessel.

It is important to note that the Jacobian is used not only to calculate actuator velocities, but also to calculate condition number and dexterity as depicted in Subsection 3.8.2.

## 3.3. Dynamics of the Stewart platform

In order to properly select the actuators, or cylinders, for the motion compensating Stewart platform, the forces required of the actuators to balance the inertia forces and external loads must be determined.

The procedure described in [28] formulates the forces required of the actuators based on screw theory considering that there are nine wrenches acting on the platform, six exerted by the legs, one by gravity, one by the inertia loads, and finally one by the external loads. From the balance of forces and moments, the equation below is formulated, a linear 6x6 system of equations that can be solved numerically or analytically to produce the forces on the actuators.

$$\mathbf{U_P f}^T = \begin{bmatrix} m\left(a_{Px} - g_{Px}\right) - F_{PE,x} \\ m\left(a_{Py} - g_{Py}\right) - F_{PE,y} \\ m\left(a_{Pz} - g_{Pz}\right) - F_{PE,z} \\ -C_{IP,x} - C_{PE,x} \\ -C_{IP,y} - C_{PE,y} \\ -C_{IP,z} - C_{PE,z} \end{bmatrix} \tag{3.16}$$

Where $\mathbf{f}^T$ is the vector that contains the forces on the actuators, $\mathbf{U_P}$ is the matrix with the Plücker coordinates of the six legs. $\mathbf{a_P}$ is the acceleration vector of the platform, $\mathbf{g_P}$ is the gravity vector, $\mathbf{F_{PE}}$ is the vector with the external forces acting on the platform, $\mathbf{C_{PE}}$ is the vector with the external moments acting on the platform, and $\mathbf{C_{IP}}$ is a vector containing the mass moment of inertia. The subscript $_P$ indicates that the variables are referenced in the platform reference system.

$$\mathbf{C_{IP}} = -\left(\mathbf{I_P}\dot{\omega}_P^T\right) - \begin{bmatrix} 0 & -\omega_{P,z} & \omega_{P,y} \\ \omega_{P,z} & 0 & -\omega_{P,x} \\ -\omega_{P,y} & \omega_{P,x} & 0 \end{bmatrix} \mathbf{I_P}\omega_P^T \tag{3.17}$$

Where $\mathbf{I_P}$ is the matrix with the mass moment of inertia in all directions, $\omega_\mathbf{P}$ is the rotational speed vector, and $\dot{\omega}_P$ is the rotational acceleration vector. An important observation is that all the parameters involved in calculating the forces on the actuators are in the reference system of the platform, including the matrix with the Plücker coordinates.

## 3.4. Loads acting on and transmitted to the Stewart platform

The Stewart platform mounted on the crane's boom must be designed to withstand the loads to be transmitted to it in different scenarios. Correct identification of these cases, both qualitatively and quantitatively, allows for the selection and specification of the actuators in terms of the loads with which they will have to deal.

### 3.4.1. Blade installation

During the installation of blades using the motion compensating Stewart platform, the blade and BIT assembly will transmit a set of forces and moments to the Stewart platform, they are:

- Own weight of Stewart platform and its actuators.
- BIT weight.
- Blade weight.
- Wind loads acting on the blade
- Dynamic amplification of the loads due to vessel's motions.
- Accidental loads during the mating phase.

- Bumper loads from the primary blade alignment system, such as shark fins.

In order to get realistic numbers for the loads acting on and transmitted to the Stewart platform, real figures from the Arcadis Ost 1 wind farm installation campaign will be used as reference for the BIT and blade weights. The blade of Vestas' V174 9.5MW wind turbine is 84.6 m long, weighs 34220 kg, and its center of gravity is 23.77 m away from the blade root [29]. The weight of the BIT is 32000kg [30].

Wind loads acting on the blade and transmitted to the Stewart platform are calculated using the cross-flow principle and the correction factor proposed in [31]. They are calculated only for the specification of the actuators, the aerodynamic loads calculated in the numerical simulations in the OrcaFlex environment use the blade element momentum (BEM) method adapted from AeroDyn, and because there is no turbine rotating, axial and tangential induction factors are not used. The methodology used to calculate the aerodynamic loads calculated for the specification of the actuators of the platform is presented in Appendix B, as well as the detailed results. The aerodynamic loads chosen for the actuator specification were calculated using steady wind with a speed of 16m/s, which is already above the allowed wind speed for blade installation. Although this combination is impossible to occur simultaneously, the aerodynamic loads acting on the blade and transmitted to the Stewart platform will be chosen for the purpose of actuators specification as the maximum total lift force, maximum drag force, maximum lift moment about the blade's center of gravity, and maximum drag moment about the blade's center of gravity. It is important to point out that, in the cross-flow principle, the lift force is the load perpendicular to the plane of the inflow wind, hence acting vertically for a horizontal blade under installation configuration. Additionally, the critical combination of vertical loads will occur when the aerodynamic lift force acts in the same direction as the gravity forces (BIT, blade and platform weight); therefore, the critical combination of vertical forces will occur at the largest magnitude of negative lift aerodynamic force.

The critical aerodynamic forces acting on the wind turbine blade are:

- Critical lift force: -13.64 kN.
- Critical lift moment: 549.95 kN.m.
- Critical drag force: 19.41 kN.
- Critical drag moment: 573.00 kN.m.

The structural design of the Stewart platform falls out of the scope of this thesis; therefore, a detailed weight will not be specified; nevertheless, given the importance of this parameter, the platform and actuators are estimated to have a combined weight of 10 metric tonnes.

Due to the intrinsic characteristic of the offshore environment, every lifting operation will be subject to a dynamic amplification factor (DAF) due to the movements of the vessel, and to take this characteristic into account, a dynamic amplification factor of 1.3 is considered [32]. As aerodynamic loads are not affected by the dynamics of the vessel, the dynamic amplification factor shall only be used on the weight of the components.

During the blade mating phase, an unexpected motion of the hub that is not compensated on time by the Stewart platform will lead to undesired loads on the blade that can, among other things, damage the blade's guiding pins and / or bolts and cause other structural damages to the equipment involved in the operation; additionally, the impact will transmit the load from the blade to the actuators of the Stewart platform, this causes an overload on the actuators that might result in a leakage in case the actuators are hydraulic cylinders, i.e. possibly causing an accident with consequences to the assets and to the environment.

A possible accidental overload on the actuators shall be considered in their specification; it is known that the loads calculated during a project and design phase may not be encountered exactly during the actual offshore operations; therefore, an overloading protection system shall not come in place necessarily when the calculated actuators load are reached, but before an accident is caused. This overload

protection system must be implemented in the control strategy and can consist of moving the Stewart, and blade root as a consequence, platform away from the hub while maintaining the relative orientation between the blade and the hub, as well as disabling the crane joystick in movements that will bring the blade root closer to the hub.

A summary of the loads acting on, or transmitted to, the Stewart platform is presented in Table 3.1.

**Table 3.1:** Magnitude and direction of the loads acting on the Stewart platform under normal operational conditions. DAF is not applicable to aerodynamic loads.

| Load description | Magnitude | Magnitude (DAF = 1.3) | Direction |
|---|---|---|---|
| **Stewart plat. weight** | 98.10 kN | 127.53 kN | Negative z axis |
| **BIT weight** | 313.92 kN | 408.10 kN | Negative z axis |
| **Blade weight** | 335.70 kN | 436.41 kN | Negative z axis |
| **Drag force** | 19.41 kN | 19.41 kN | Positive x axis |
| **Drag moment** | 573.00 kN.m | 573.00 kN.m | About z axis |
| **Lift force** | 13.64 kN | 13.64 kN | Negative z axis |
| **Lift moment** | 549.95 kN.m | 549.95 kN.m | About x axis |

### 3.4.2. Special cases

In addition to the loads to which the Stewart platform is subjected during the blade installation phase, other special cases must be considered in the design of the platform and specification of its actuators. Important scenarios that must be considered are:

- The crane on the boom rest with the platform attached to it. The direction of the loads due to its own weight will change in direction and must be considered.
- Survival mode. Similarly to what occurs with cranes, the platform must be designed to withstand extreme wind loads both for the crane on and off the boom rest.
- Handling. The platform must be robust enough and equipped with lifting points for handling. It is relevant that the platform has not only lifting points, but also allows for safe handling using a forklift, for example.
- Storage and seafastening. When not in use, the platform must have accessories that allow safe storage and seafastening. For storage, it is interesting that the hydraulic and electronic systems are not completely exposed and are reasonably protected. Additionally, it is recommended that the structure of the platform enables fast, safe and cost-effective seafastening, with the structure for twist locks, for example.
- Impacts and accidental loads. During the use of the platform, the equipment will be subjected to loads for which it was not necessarily designed, such as impacts and other accidental loads. For this reason, it is recommended that the platform is robust and equipped with protection frames to protect the structural integrity of the platform and protect its fragile accessories. These guards and protections must not interfere with the platform's workability and functionality.

## 3.5. Architecture of the Stewart platform

The main purpose of the Stewart platform during blade installation is to compensate for the relative motions between the blade root and the hub where the former is to be connected. In the case of the RNA method, the hub and nacelle are placed on top of the installation tower. The Stewart platform (base, actuators and platform) is attached to the crane's boom, where the base is connected to a support structure. The blade installation concept with a Stewart platform is shown in Figure 3.4, where the blade is secured by the BIT that is fixed to the controllable Stewart platform on the crane boom.

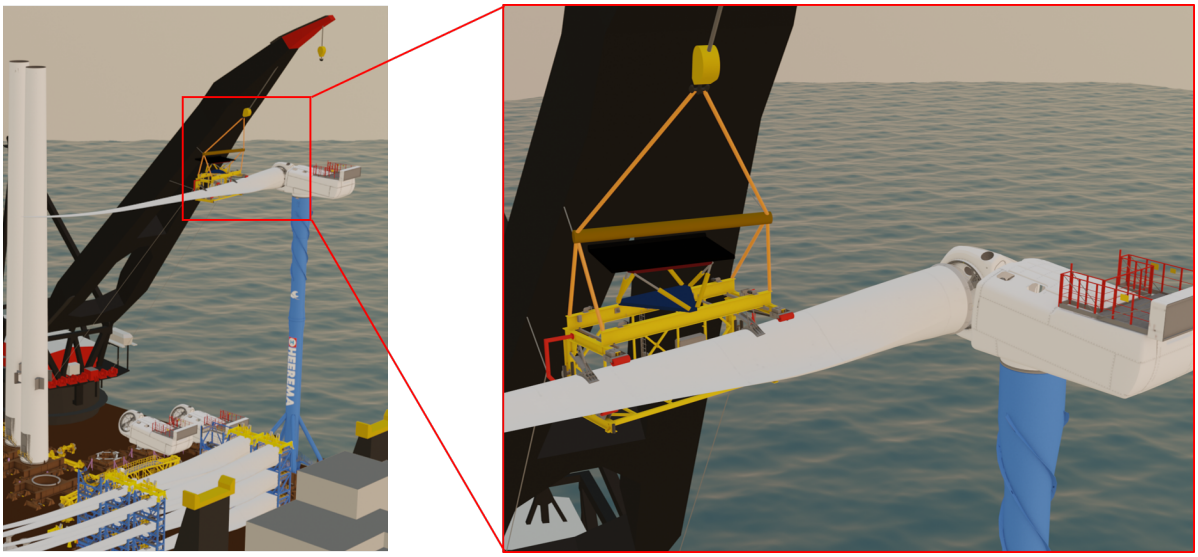

**Figure 3.4:** Stewart platform's configuration for blade installation.

The blade, secured by the blade installation tool (BIT), is raised to the height where the BIT is rigidly connected to the platform. Then, the Stewart platform is used to hold the BIT and blade weight, as well as to compensate the relative motions between blade root and hub. Because the BIT is connected to the platform, it is an advantage to define the platform's dimensions based on the BIT's. Figure 3.5 shows how the Stewart platform's hexapod has its dimensions constraint to the BIT. Using this concept, four definitions are made:

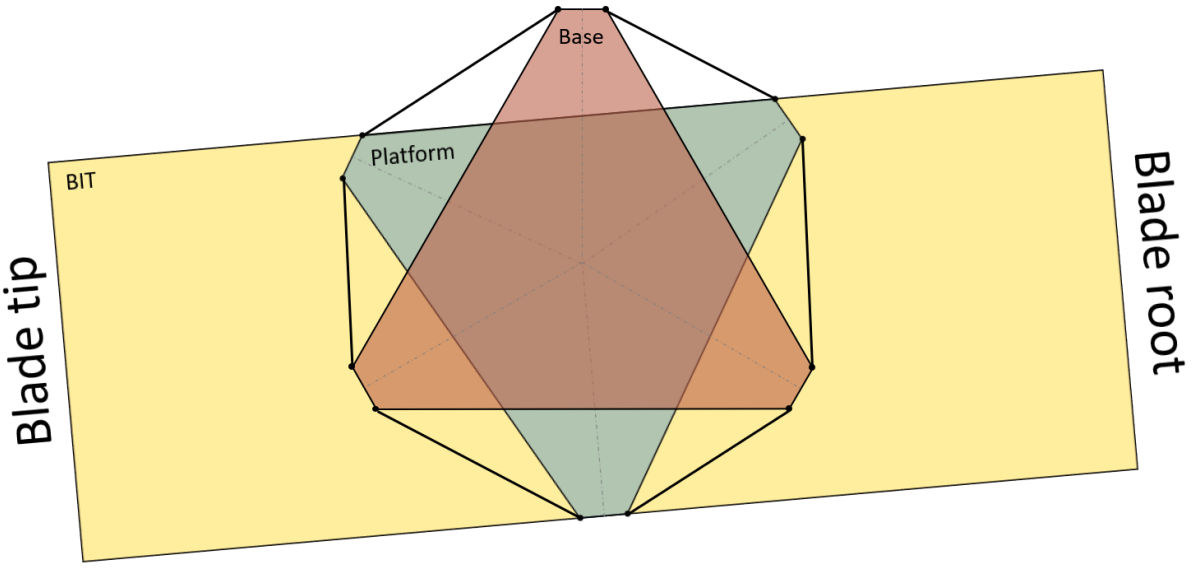


**Figure 3.5:** Stewart platform's schematic for blade installation - top view.

- The distance between the platform's shortest and opposing longest side is the same as the BIT's top frame width.
- The shortest side of both the base and the platform is 0.5 m long. It is assumed that this value is enough to avoid mechanical interference between the base's and platform's joints.
- Geometry of base and platform is based on an equilateral triangle with the vertices trimmed so the shortest side is 0.5 m long.

- The base and platform have the same main dimensions, i.e. both longest and shortest sides have the same length.

Based on these definitions, the length of the longest side can be calculated based on a BIT height of 4.2 m and the shortest side of 0.5 m. Figure 3.6 shows the parameterized main dimensions of the hexapods.

$$L = \frac{BIT_{Height}}{\sin \pi/3} - l \approx 4.35\text{m} \tag{3.18}$$

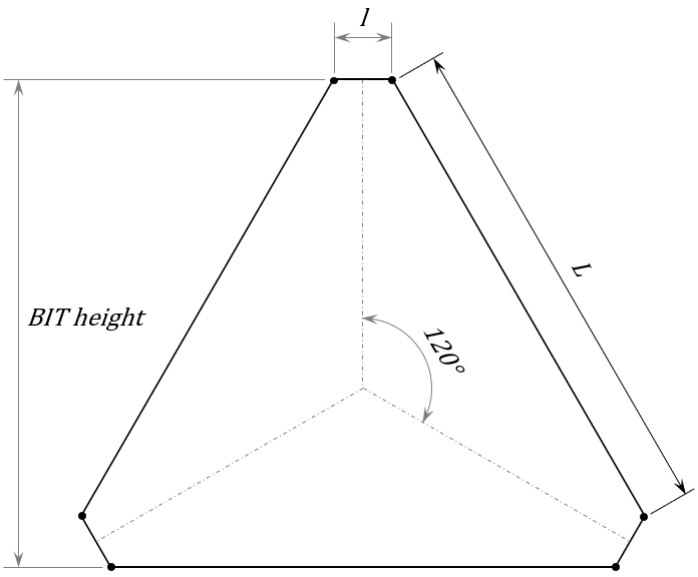


**Figure 3.6:** Parameterized dimensions of the Stewart platform.

Once the base and platform dimensions are defined, their joint coordinates can be calculated. However, the origin of their coordinate systems must be defined, and these definitions are valid for both the platform and base. First, all joints form a plane such that, in their local coordinate system, $z = 0$ for all points. Second, the origin of the coordinate systems is chosen to coincide with the first joint. And finally, the local coordinate system is defined such that the coordinate $y-$ of the second gimbal, on both the base and the platform, is equal to $0$. These definitions are useful for solving the forward-kinematics problem and do not cause a loss of generality. The base and platform joints' coordinates in their local reference systems are calculated as a function of the parameters defined previously, i.e. the platform's and base's lengths. Not to loose generality, longest and shortest sides of the base are defined as $L_b$ and $l_b$, respectively, while the longest and shortest sides of the platform are referenced as $L_p$ and $l_p$, respectively.

**Table 3.2:** Base and platform gimbal's coordinates in their local reference systems.

| | Base | | | Platform | | |
|---|---|---|---|---|---|---|
| Gimbal | $x$ | $y$ | $z$ | $x$ | $y$ | $z$ |
| #1 | $0$ | $0$ | $0$ | $0$ | $0$ | $0$ |
| #2 | $L_b$ | $0$ | $0$ | $l_p$ | $0$ | $0$ |
| #3 | $L_b + l_b \cos \frac{\pi}{3}$ | $l_b \sin \frac{\pi}{3}$ | $0$ | $l_p + L_p \cos \frac{\pi}{3}$ | $L_p \sin \frac{\pi}{3}$ | $0$ |
| #4 | $L_b + (l_b - L_b) \cos \frac{\pi}{3}$ | $(L_b + l_b) \sin \frac{\pi}{3}$ | $0$ | $l_p + (L_p - l_p) \cos \frac{\pi}{3}$ | $(L_p + l_p) \sin \frac{\pi}{3}$ | $0$ |
| #5 | $L_b - l_b + (l_b - L_b) \cos \frac{\pi}{3}$ | $(L_b + l_b) \sin \frac{\pi}{3}$ | $0$ | $(l_p - L_p) \cos \frac{\pi}{3}$ | $(L_p + l_p) \sin \frac{\pi}{3}$ | $0$ |
| #6 | $-l_b \cos \frac{\pi}{3}$ | $l_b \sin \frac{\pi}{3}$ | $0$ | $-L_p \cos \frac{\pi}{3}$ | $L_p \sin \frac{\pi}{3}$ | $0$ |

## 3.6. Motions to be compensated by the Stewart platform and actuators' loads

The results of the installation tower simulations described in Chapter 2 are used to calculate the requirements for the Stewart platform actuators, that is, the loads to which they are subjected, their required lengths to compensate for the relative motions and the required velocity. For these calculations, the distance between the blade root and the hub was kept constant; in other words, the blade root perfectly followed the hub. Actuators' lengths, forces, and velocity were calculated in this scenario for the 30 load cases described in Chapter 2 using the inverse kinematics approach.

The results presented below are, for clarity, presented only for the load cases with the lowest and highest double amplitude in hub motions, as depicted in Subsection 2.1.3. Another important factor

that must be considered is the vertical distance between the base and the platform. In the initial, or static, position, the platform's $x-y$ plane is parallel to the base's $x-y$ plane; therefore, this vertical distance is the neutral distance between the platform and the base along the $z-$ axis. Four different configurations were assessed with regard to the vertical distance between the base and the platform: 1.5 m, 2.0 m, 2.5 m and 3.0 m. The dimensions of the platform and the base, as well as the external forces used, are those described in Sections 3.5 and 3.4, respectively.

Figures 3.7 and 3.8 present the required strokes, maximum absolute velocities, and mean length of all actuators in the specified load cases for perfect motion compensation, the numerical values are presented in Table 3.3. In the above-mentioned figures, the static vertical distance between base and platform is varied in order to assess its influence on the specified actuators' parameters. It is possible to see that the maximum absolute velocity and the required stroke remain nearly unchanged regardless of the static vertical distance between the base and the platform. And, as expected, the mean actuators lengths change reflecting the variation of the vertical distance between base and platform.

**Table 3.3:** Actuator's length requirements, minimum and maximum, for a vertical distance between base and platform of 1.5m, 2.0m, 2.5m and 3.0m.

| | | Leg | | | | | |
|---|---|---|---|---|---|---|---|
| | | #1 | #2 | #3 | #4 | #5 | #6 |
| z = 1.5m | Max. [m] | 3.061 | 2.564 | 2.947 | 2.550 | 3.069 | 2.434 |
| | Min. [m] | 2.957 | 2.308 | 2.777 | 2.458 | 2.801 | 2.305 |
| z = 2.0m | Max. [m] | 3.343 | 2.895 | 3.222 | 2.880 | 3.351 | 2.764 |
| | Min. [m] | 3.232 | 2.648 | 3.083 | 2.784 | 3.088 | 2.663 |
| z = 2.5m | Max. [m] | 3.671 | 3.270 | 3.549 | 3.254 | 3.680 | 3.153 |
| | Min. [m] | 3.555 | 3.034 | 3.434 | 3.155 | 3.423 | 3.048 |
| z = 3.0m | Max. [m] | 4.035 | 3.674 | 3.916 | 3.658 | 4.044 | 3.570 |
| | Min. [m] | 3.915 | 3.449 | 3.816 | 3.557 | 3.795 | 3.462 |

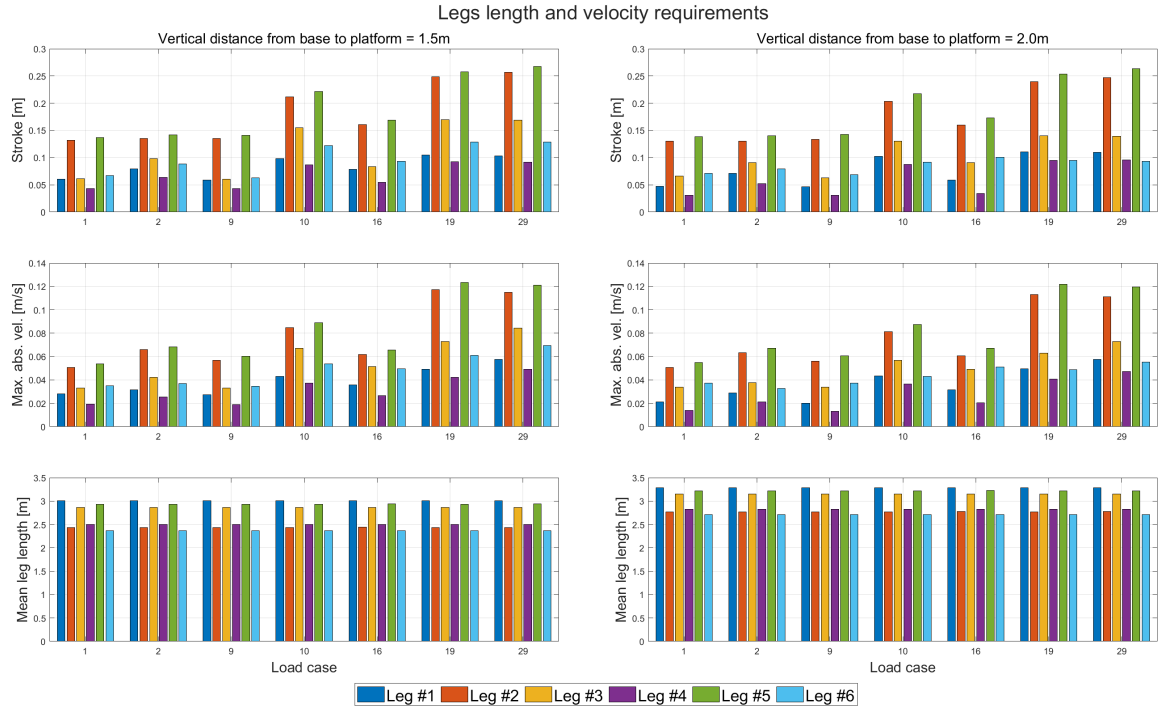


**Figure 3.7:** Stewart platform's actuators' parameters of length and velocity. Vertical distance between base and platform of 1.5m (left) and 2.0m (right).

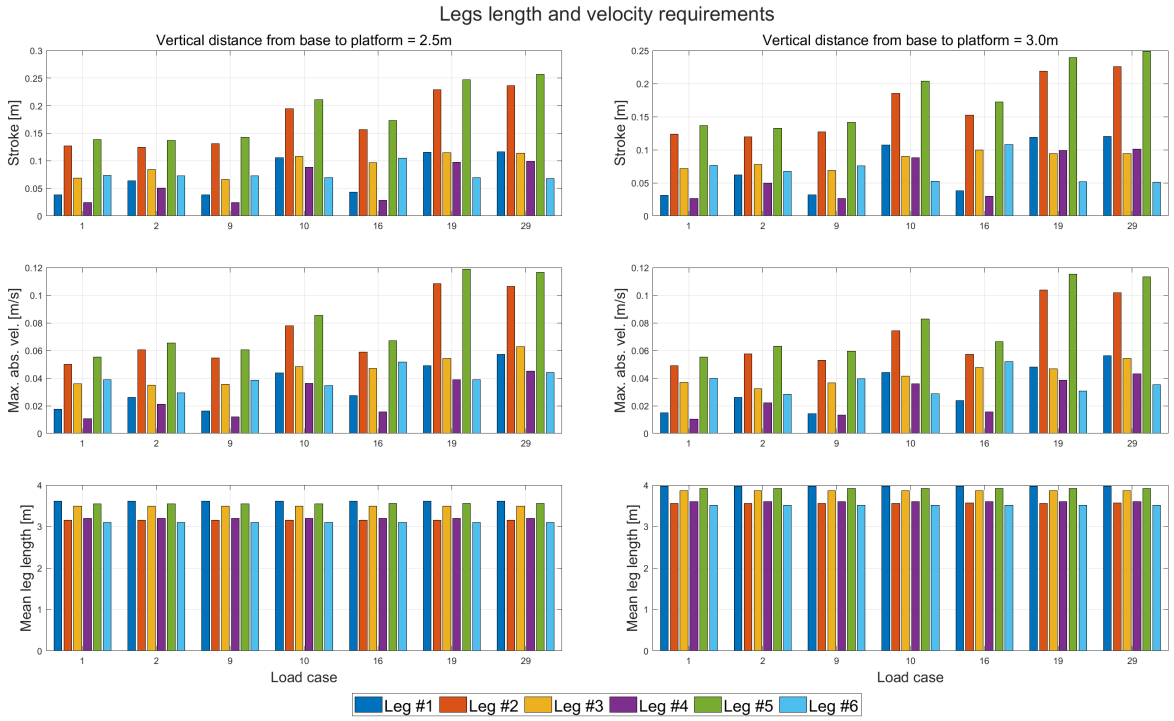


**Figure 3.8:** Stewart platform's actuators' parameters of length and velocity. Vertical distance between base and platform of 2.5m (left) and 3.0m (right).

Following the required actuators' lengths, the forces acting on them are also calculated. These forces are the result of mass and inertia forces, as well as aerodynamic loads acting on the blade and transmitted to the Stewart platform. The actuator loads parameters were calculated for the same load cases as the lengths and velocities above, and varying the static vertical distance between base and platform with the same values (1.5 m, 2.0 m, 2.5 m, and 3.0 m). The numerical values for the maximum and minimum load per actuator are presented in Table 3.4. Figures 3.9 and 3.10 graphically show the influence of varying the static vertical distance between base and platform on the actuators loads, that is, mean load, load standard deviation, and maximum load variation. From the mean load values, it can be observed that increasing the distance between the base and the platform has a great impact on the maximum absolute load applied to the actuators. Additionally, the same occurs with the maximum load variation, as well as with the load standard deviation. One important factor to point out is that some of the actuators will be more influenced by this vertical distance variation than others, this one factor allowing us to conclude that all actuators should be selected to be identical.

**Table 3.4:** Actuator's load requirements, minimum and maximum, for a vertical distance between base and platform of 1.5m, 2.0m, 2.5m and 3.0m.

| | | Leg | | | | | |
|---|---|---|---|---|---|---|---|
| | | #1 | #2 | #3 | #4 | #5 | #6 |
| z = 1.5m | Max. [kN] | -251.2 | 72.6 | -114.7 | -218.9 | 164.9 | 165.5 |
| | Min. [kN] | -374.4 | 50.7 | -247.5 | -299.2 | 109.3 | 135.3 |
| z = 2.0m | Max. [kN] | -270.8 | 79.8 | -90.8 | -183.2 | 139.3 | 185.5 |
| | Min. [kN] | -410.9 | 56.2 | -202.8 | -249.3 | 93.2 | 152.3 |
| z = 2.5m | Max. [kN] | -294.6 | 88.3 | -77.5 | -163.9 | 125.7 | 209.0 |
| | Min. [kN] | -453.7 | 62.4 | -179.2 | -223.7 | 84.6 | 171.6 |
| z = 3.0m | Max. [kN] | -321.5 | 97.7 | -69.4 | -152.3 | 117.7 | 234.5 |
| | Min. [kN] | -501.1 | 69.3 | -165.0 | -208.4 | 79.5 | 192.6 |

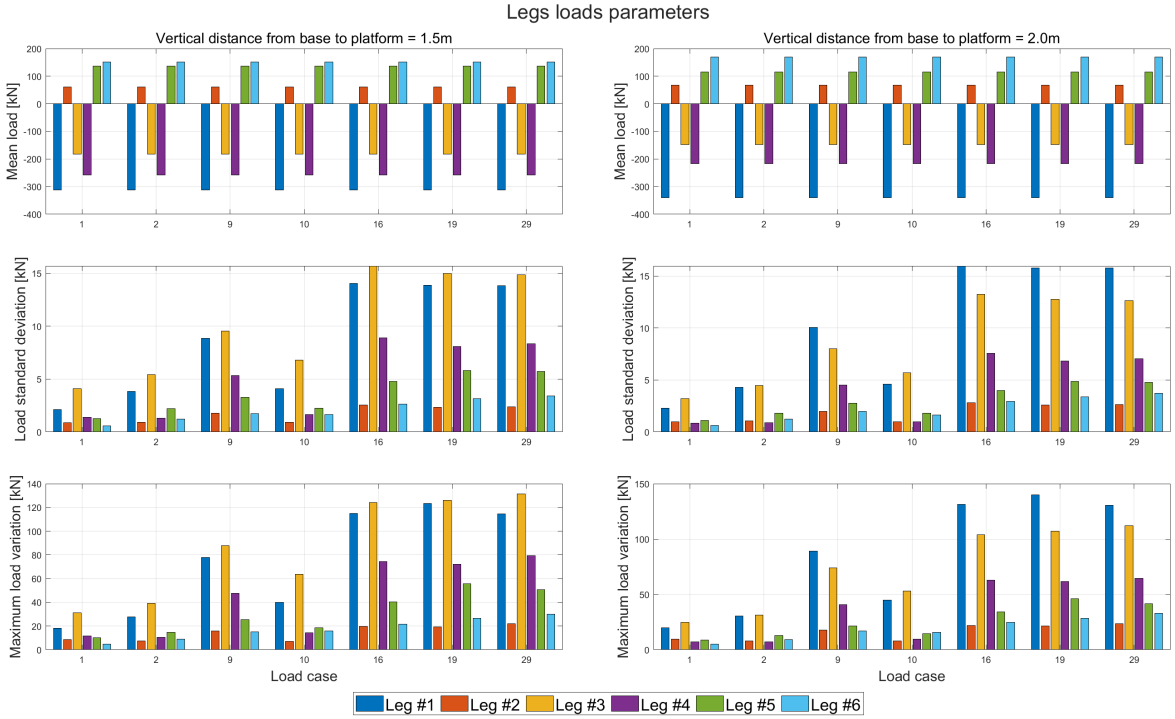


**Figure 3.9:** Stewart platform's actuators' parameters of load. Vertical distance between base and platform of 1.5m (left) and 2.0m (right).

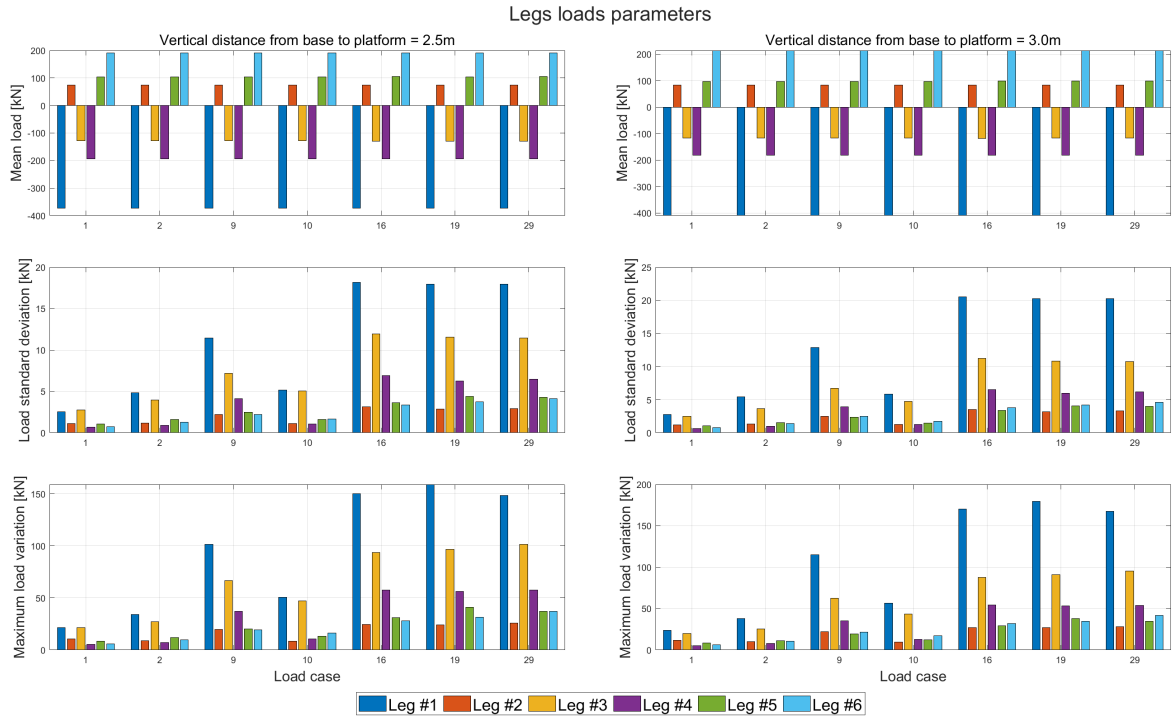


**Figure 3.10:** Stewart platform's actuators' parameters of load. Vertical distance between base and platform of 2.5m (left) and 3.0m (right).

From the adopted reference system, a negative actuator load means that the cylinder is pulling, while a positive one means that the cylinder is pushing.

## 3.7. Specification of the Stewart platform's actuators

Once length, velocity and load requirements for the Stewart platform actuators are calculated based on the hub motions to be compensated for, the cylinder selection process can be started.

This task is performed using the following steps:

- Choice of rated working pressure.
- Selection of the cylinder based on pulling and pushing loads.
- Choice of cylinder mountings based on the application.
- Assessment of minimum and maximum lengths, as well as stroke considering the requirements and dead length of cylinder.
- Buckling check.
- Required velocity check.

From a manufacturer catalog, a rated working pressure of 210 bar is chosen; this value lies in the middle range of products and is expected not to require a top rated HPU (hydraulic power unit). Next, the maximum required loads (pushing and pulling) are verified and the diameters of the bore and rod are selected. The mountings selected are from the spherical eye type, this choice is based on an increased range of out-of-plane angles that the cylinder mounting can be submitted to. With the chosen base model and mechanical characteristics, the dead length of the cylinder is evaluated along with the stroke requirements. The minimum and maximum lengths are defined as follows:

$$l_{max} = l_{dead} + 2 \cdot Stroke \tag{3.19a}$$

$$l_{min} = l_{dead} + Stroke \tag{3.19b}$$

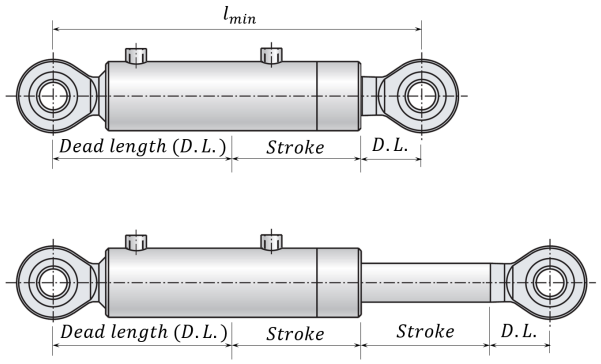


**Figure 3.11:** Cylinder lengths parameters.

The buckling check is performed using the manufacturer's guidelines for the specific cylinder configuration and piston rod diameter. The largest push load required of the actuators, detailed in Table 3.4, is used together with the diameter of the pre-selected piston rod. From the manufacturer's guidelines, the maximum allowable buckling length is verified and compared with the requirements presented in Table 3.3. For a rod diameter of 125mm and a pushing load of 250 kN, the buckling length with a safety factor of 3 is 5.75m, that is, the combination of pushing loads and cylinder lengths resulting from the calculations are not enough to cause buckling.

Next, the required cylinder velocity is compared with the manufacturer's limits, which are much above the operational requirements detailed in Table 3.3. Vremac cylinder manufacturer informs us of a maximum cylinder velocity of 5m/s. It is important to point out that the limitation for the cylinder velocity is related not only to the flow rate available from the HPU, but also to the internals of the cylinder, such as the seals.

Proceeding with the assessment, the dead length of the chosen cylinder configuration is 1.325m when considering the internal dead length, the mounting dead length, as well as an estimated 0.5m

for the joints on both sides (base and platform). Resulting in the above-mentioned total dead length. When combining the total dead length with the maximum and minimum cylinder length requirements from Table 3.3 for vertical distance between base and platform of 1.5m and 3.0m, it becomes clear that one cylinder stroke is not capable of attending all the same six legs. Nevertheless, the same cylinder configuration for all six legs is a design choice for several reasons; therefore, the cylinder stroke is defined to avoid unnecessary high loads and give the platform a wider range of motions and possible operating configurations. For these reasons, the chosen stroke is **1.225m**, resulting in a maximum length of **3.775m** and a minimum length of **2.550m**, enabling the configurations with vertical distance between the base and platform of 2.0 and 2.5 m, as well as providing a wide range of operational configurations (workspace).

**Table 3.5:** Cylinders specifications [33]

| | | | |
|---|---|---|---|
| Dead length [m] | 1.325 | Rod diameter [mm] | 125 |
| Maximum length [m] | 3.775 | Bore diameter [mm] | 220 |
| Minimum length [m] | 2.550 | Piston area / ring area [-] | 1.48 |
| Stroke [m] | 1.225 | Max. pulling force [kN] | 541 |
| Working pressure [bar] | 210 | Max. pushing force [kN] | 798 |

## 3.8. Stewart platform's spatial characteristics

The spatial characteristics of the Stewart platform are not only defined by its range of motions (workspace), but also if there are positions inside the workspace where singularities occur, which means a specific position where the platform becomes immobile, or if the kinematic formulations are not existing and unique.

The workspace of the proposed Stewart platform design is calculated considering the maximum and minimum actuators lengths, then the dexterity is calculated for every position inside the workspace, and finally it is verified if any singularities are possible to occur.

### 3.8.1. Workspace

The workspace of the Stewart platform is defined as its motion range, that is, the total 6 DoF motion range of the platform.

Once the actuators are specified, their minimum and maximum lengths are known, thus it is possible to determine the Stewart platform's workspace. By varying the lengths of all six actuators from their fully retracted to their totally extended length, forward kinematics, as described in Subsection 3.1.2, is used to calculate the position and orientation of the platform for all possible combinations of actuator lengths. Therefore, forming the platform's workspace, the boundaries in all six degrees of freedom where the platform can reach.

Figure 3.12 shows the platform translation workspace, that is, surge, sway, and heave. Here, the platform and base planes are parallel, and their centroids are connected by an imaginary line perpendicular to both of these planes. The workspace values presented in Figures 3.12 and 3.13 are the platform's reach in the specified degree of freedom, and centered around the base centroid.

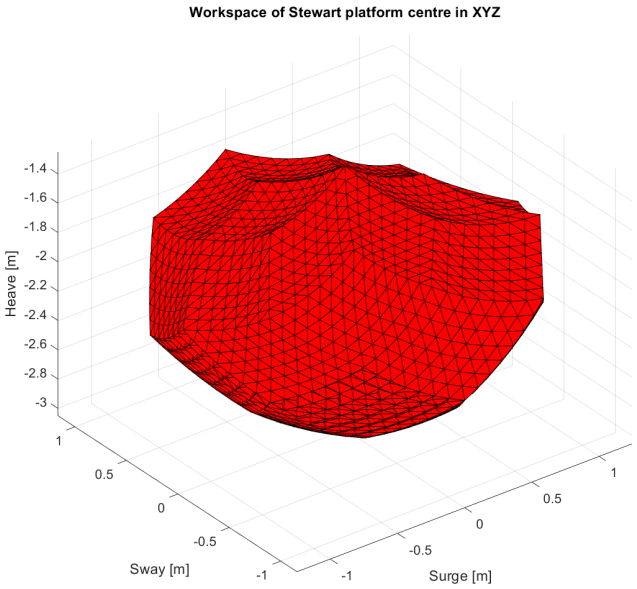


**Figure 3.12:** Workspace of the Stewart platform in $x-$, $y-$ and $z-$ axis.

Because all six degrees of freedom are limited by the actuators' lengths, it is possible to define 15 combinations of two degrees of freedom to build the workspace. The 15 two-DoF combinations are presented graphically in Figure 3.13. It is important to point out that the orientation limits of the platform's workspace (roll, pitch, and yaw) are generally broad and allow a wide range of positions. This plays an important role in the operation of the Stewart platform and its ability to maneuver the blade.

The workspace of the Stewart platform presented in this section is calculated based on the previously defined minimum and maximum lengths of the cylinders. Moreover, to increase the platform's workspace, actuators with a larger available stroke are necessary. However, as described in Section 3.7, a larger stroke means a longer minimum cylinder length, which will increase the minimum vertical distance between the base and the platform, as well as increase the loads to which the actuators are subjected, as described in Section 3.6. These parameters were thoroughly evaluated to specify actuators for the specific application of Vestas V174-9.5MW blade installation in the proposed methodology. However, further investigation is required for different wind turbine blades.

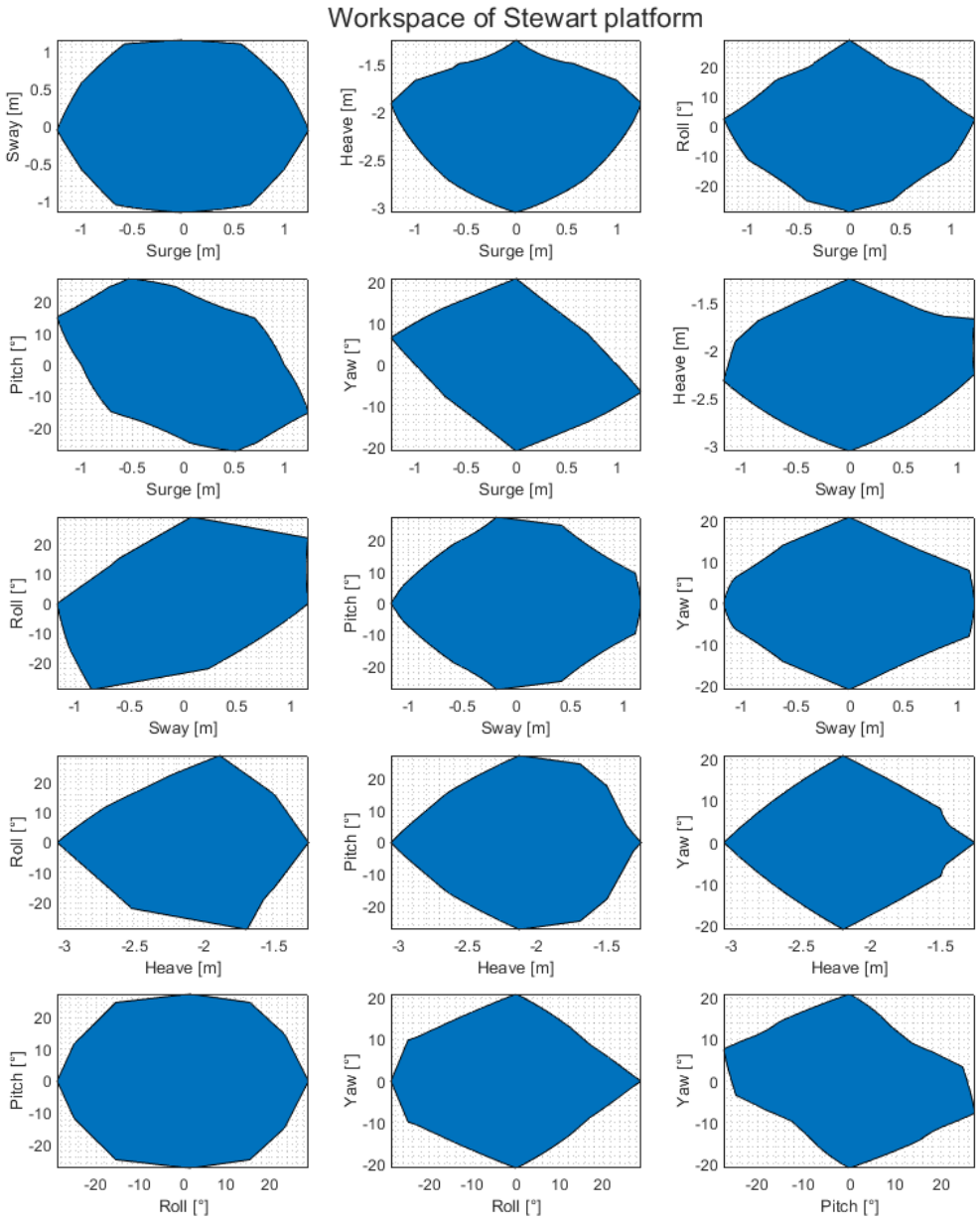


**Figure 3.13:** Stewart platform's workspace in all 15 combinations of two degrees of freedom.

### 3.8.2. Dexterity

The dexterity of a Stewart platform is an index to avoid singularity configurations. It is a characteristic value of the Stewart platform at a given position, the inverse of the condition number, $\kappa$. The condition number is calculated as follows:

$$\kappa = \|\mathbf{J}\|\|\mathbf{J}^{-1}\| \tag{3.20}$$

Where $\kappa$ is the condition number and **J** is the Jacobian matrix as defined in Equation 3.14. Hence,

the condition number is the product of the Jacobian matrix norm and the norm of its inverse. Dexterity is then defined as the inverse of the condition number:

$$Dexterity = \frac{1}{\kappa} = \frac{1}{\|\mathbf{J}\|\|\mathbf{J}^{-1}\|} \tag{3.21}$$

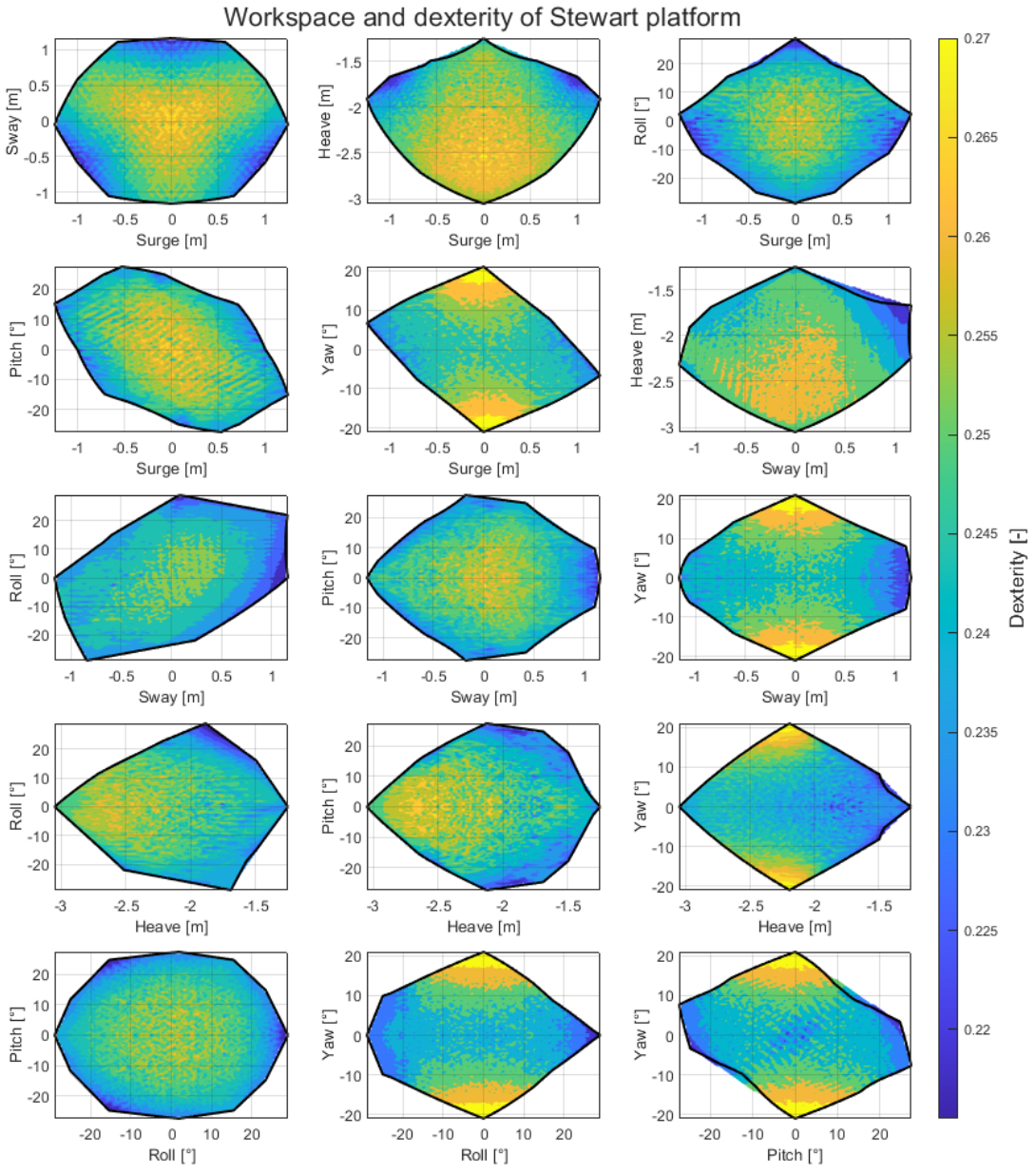


**Figure 3.14:** Stewart platform's dexterity in all 15 combinations of two degrees of freedom.

The dexterity value can vary from 0 to 1, where the maximum value of 1 means that the manipulator is *isotropic*, meaning that the position and architecture of the Stewart platform with dexterity equal to 1 is the best possible. On the other hand, a dexterity value of 0 means that the corresponding position

is a singularity. Low dexterity values mean that the forces and velocities of the actuators may not be limited to reasonable values. In [34] a minimum dexterity value of 0.2 is suggested, from Figure 3.14 it is possible to notice that the dexterity of the proposed Stewart platform is kept between **0.215** and **0.270**, not only above the literature recommendation, but also having a fairly uniform dexterity value in all possible poses inside the workspace. The uniform characteristic of the Stewart platform means that in every pose inside the workspace, the actuators are not subject to unreasonable speeds and loads. A color map of the dexterity in every possible position inside the workspace is presented in Figure 3.14.

### 3.8.3. Singularities

The singularity of a Stewart platform can be classified into three different categories, Architecture singularity, Configuration singularity, and Formulation singularity [35].

Architecture singularities are caused by a particular architecture of the Stewart platform. These kinds of singularity exist for all possible configurations in the platform's workspace, and can only be eliminated by design. One example of architecture singularities is when base and platform have a regular hexagonal shape. Configuration singularities are caused by a particular manipulator pose and, therefore, are dependent only on one individual configuration. Finally, formulation configurations are caused by the failure of the kinematic model, for example if the rotation about the $y-$ axis, as in the reference system presented in Figure 3.2a, is $\pm 90^{\circ}$, [35]. It is important to point out that the dexterity of the Stewart platform is equal zero when it is in a configuration or formulation singularity, therefore, it is possible to notice from Figure 3.14 that the proposed Stewart platform does not have configuration or formulation singularities inside its workspace. Nevertheless, these singularities can occur, but they do not become relevant. Additionally, an architecture singularity can only be solved by design.

As established previously, the maximum and minimum actuator lengths limit the workspace such that configuration and formulation singularities are avoided. In addition, architectural singularities are avoided with the proposed design of the Stewart platform's hexagon.

## 3.9. Platform's degrees of freedom

The Stewart platform must be able to manipulate the payload, i.e. the blade, in all 6 degrees of freedom in order to compensate for the relative motions between the blade root and hub. Nevertheless, the number of degrees of freedom is a function of the number of links and joints, and the number of degrees of freedom of these joints. The effective number of degrees of freedom of the platform is calculated as follows [34]:

$$F = \lambda \left( n_l - n_j - 1 \right) + \sum_{i=1}^{n_j} f_i \tag{3.22}$$

Where:

- $F$ = Effective degrees of freedom of the mechanism.
- $\lambda$ = Degrees of freedom of the space in which the mechanism operates. $\lambda = 6$.
- $n_l$ = Number of links in the mechanism.
- $n_j$ = Number of joints in the mechanism.
- $f_i$ = Number of degrees of freedom of the $i^{th}$ joint.

Introducing the number of linear actuators, $n_a$, it is possible to define the number of joints and links as a function of $n_a$. These relationships are as follows;

$$n_l = 2 + 2n_a \tag{3.23a}$$

$$n_j = 3n_a \tag{3.23b}$$

Simplifying Equation 3.22 to:

$$F = \lambda\,(1 - n_a) + \sum_{i=1}^{n_j} f_i = 6\,(1 - n_a) + \sum_{i=1}^{n_j} f_i \tag{3.24}$$

The number of joints and links is illustrated in Figure 3.15, where each line or block represents a link, connected to another link, by a red circled joint. One must observe that, in the view, three actuators are omitted.

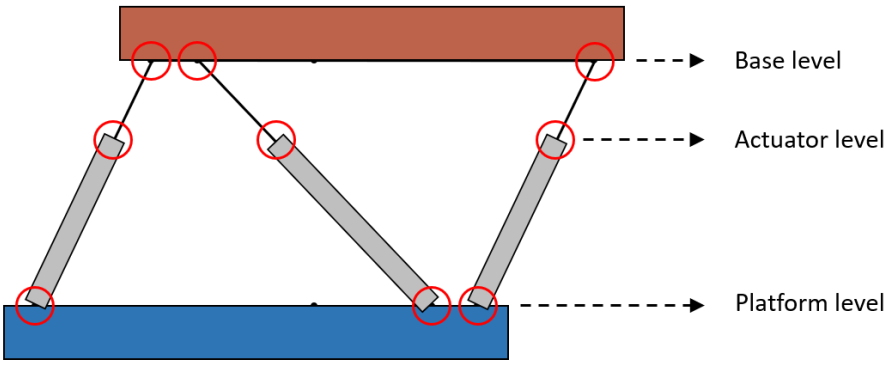


**Figure 3.15:** Location of links and joints on the Stewart platform.

The total number of degrees of freedom of all joints is calculated as follows:

$$\sum_{i=1}^{n_j} f_i = n_a\,(f_b + f_a + f_p) \tag{3.25}$$

Where $f_b$ is the number of degrees of freedom of the joint at the base level, $f_p$ is the number of degrees of freedom of the joint at the platform level and $f_a$ is the number of degrees of freedom of the joint at the actuator level. To obtain a Stewart platform with six effective degrees of freedom, $F = 6$, Equations 3.24 and 3.25 are combined to produce in:

$$f_b + f_a + f_p = 6 \tag{3.26}$$

Therefore, the number of effective degrees of freedom of the Stewart platform depends on the types of joints between the links. These joints can be separated in two groups, the joints at actuator level and the joints at base and platform levels. First, the type of joint is defined at the actuator level, where there are two main options, a cylindrical joint and a prismatic joint. The former allows for two degrees of freedom (axial translation and rotation about this same axis), while the latter only allows for one degree of freedom (axial translation), where the rotation is restricted due to the prismatic shape of the rod.

For the joints at base and platform levels, two main options are available, i.e. a universal or Cardan joint with two degrees of freedom; and a spherical joint with three degrees of freedom. Therefore, to obtain the result in Equation 3.26, only three possible joint combinations are allowed. Nevertheless, it is preferred that, at actuator level, the joints are of the cylindrical type; this is due to its familiarity (regular hydraulic cylinders, for example), large availability in the market, and reasonably simple maintenance.

Having selected the cylindrical joint for the actuator level, the only remaining option for the base and platform levels is the Cardan joint, which is therefore in compliance with Equation 3.26, where $f_b = f_a = f_p = 2$.

# 4

# The operation of the proposed system and mechanical concept

The development of a motion compensation system for blade installation must also consider the practical application of the proposed solution. These considerations are divided in two main parts, the first one being an operational feasibility study, in this part a simplified operational procedure for blade installation using the proposed system is developed. This considers equipment limitations, deck layout, possible interference with other wind turbine parts, and other factors.

The second part consists of the development of a preliminary concept of the mechanical system to be used. This includes the specification of the cylinder's joints on base and platform, the connection system between the BIT and Stewart platform, the base's support structure on the crane's boom, as well as the auxiliary system used to enable the blade connection to hub. The purpose of this section is to present how these systems can be developed. The solutions presented here are not necessarily the best ones, and further development is required, in addition, structural design of the parts, and detailed specification of those are not part of the thesis project scope.

## 4.1. The installation procedure

The main objective of this thesis project is to develop a system that enables the installation of blades in the RNA method without the use of the GREP tool, therefore, this operational procedure is developed keeping the basic assumptions of the RNA method and how it was successfully used in the WTG installations at the Arcadis Ost 1 wind farm.

Some of the constraints used are that the installation vessel does not go to port to be loaded out, a barge is towed to the project location, moored on the vessel, and all the components of three complete wind turbines are loaded onto the vessel and placed in specific positions according to the seafastening design and other project constraints. As the WTG's foundations have been previously installed, the main components loaded on the installation vessel are:

- Three sets of blades, a total of nine blades.
- Three nacelles with the hubs already connected to them.
- Three WTG's towers.

In addition, other auxiliary equipment is also included, such as lifting tools, utilities containers, and others.

One of the main advantages in utilizing installation vessels with two cranes and a large deck area is that two different scopes can be executed at the same time, shortening the critical path, in the Arcadis

Ost 1 project the towers were installed by one crane, while the other crane was being used to install the blades to the hub, and later the RNA on the tower. Therefore, the blade installation procedure is developed considering that the first tower had been installed and only two more towers remain on the deck. However, during all times, the lifted objects did not cross the space that the first tower was occupying, this is motivated in the event of a contingency where the blades must be installed with three towers on the deck.

### 4.1.1. Equipment and accessories used in the installation

In the RNA method without the GREP tool, other equipment are involved in the operation, and their role in the installation process is specified below.

#### The Stewart platform

The main equipment in operation. It is responsible for compensating the relative motions between the blade root and the hub. The Stewart platform is attached to the crane's boom via a support structure that folds to enable different operational positions, as well as folds to a space saving storage position while the system is not in use, e.g., for other operations and while the crane's boom is in the boom rest.

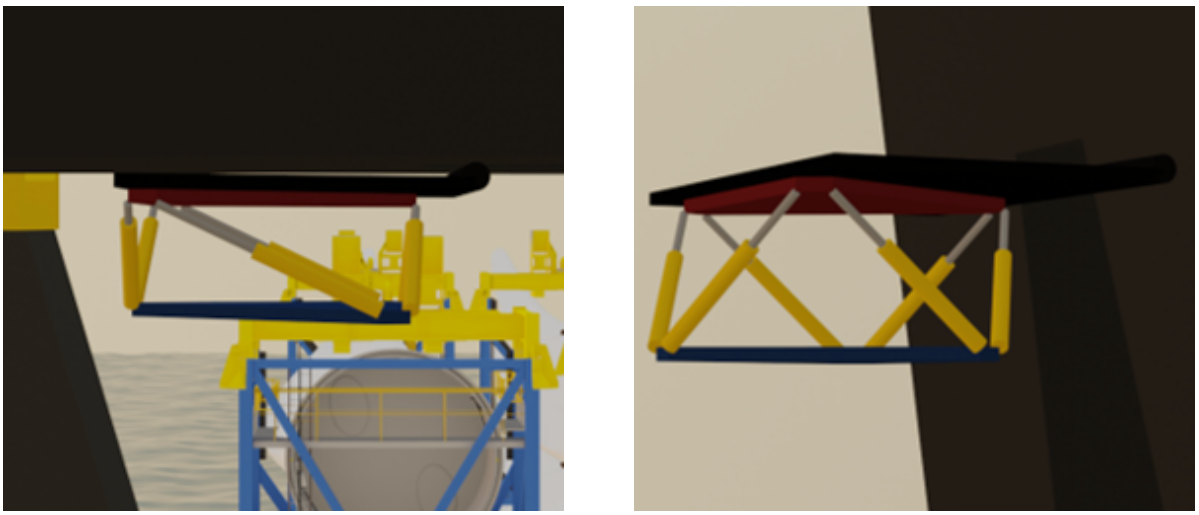

**(a)** Stewart platform on crane boom in boom rest.

**(b)** Stewart platform on crane boom in operational position.

**Figure 4.1:** Stewart platform on crane's boom in the rest and operational positions.

#### Blade installation tool - BIT

The BIT (blade installation tool) is used to hold and lift the blades. It has two claws that clamp onto the blade to keep it stable inside the BIT, and open once the blade is connected to the hub, so the BIT can be fully disconnected from the blade.

The BIT is also equipped with four lifting points at the corners of its top face and two steering arms, a red structure at both sides of the BIT in Figure 4.2, where tugger lines are connected to control its movements.

**Figure 4.2:** Blade installation tool.

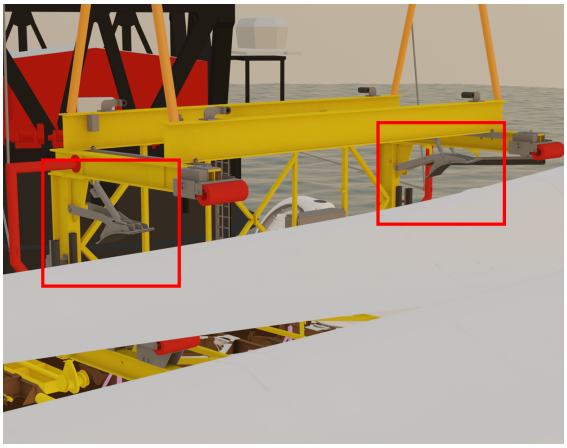

**(a)** Clamping claws open.

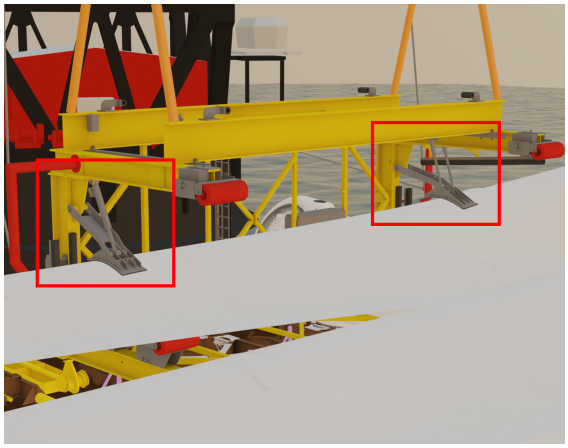

**(b)** Clamping claws closed.

**Figure 4.3:** Blade installation tool with its clamping claws open and closed, highlighted in red.

### Spreader bar

The BIT could be directly connected to the crane hook using four slings; nevertheless, some aspects of the installation procedure indicate that the use of a spreader bar is beneficial. By using a spreader bar, two advantages arise, first, while pulling the blade towards the crane boom to connect the BIT to the Stewart platform, the BIT is not tilted, hence reducing the chance of the blade slipping out, characteristic of a two-point lift. And secondly, it generates a larger space to accommodate the Stewart platform between the BIT and the Spreader bar.

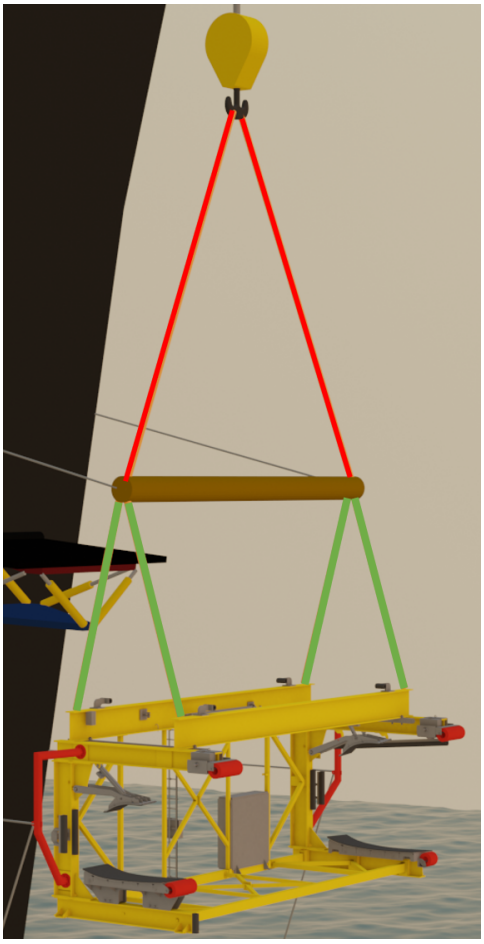

**Figure 4.4:** Spreader bar configuration. Red slings connecting the spreader bar to the crane's hook; green slings connecting the spreader bar to the BIT.

The spreader bar is connected to the crane hook using two slings (in red), as shown in Figure 4.4, the length of these slings is calculated so that their angle with the vertical axis does not exceed 30°, which is common good practice in lifting operations. To connect the spreader bar to the BIT, two pairs of double slings (in green) are used. The length of these slings is calculated to match common commercial available slings lengths and create enough space between the BIT's top face and the spreader bar for the Stewart platform; this space is necessary during the installation phase where the BIT is connected to the Stewart platform.

### Tugger winches

In the installation process, three sets of tugger winches are used, each set made of one pair of tugger winches. One set of tugger winches connects the crane boom, above the Stewart platform, to the spreader bar; the second set of tugger winches connects the crane boom, below the Stewart platform, to the BIT; and the final set of tugger winches connects the crane's rotating base / slewing platform to the BIT. The arrangement of the tug lines is depicted in Figure 4.5.

The first set of tugger lines (orange) is mainly used to pull the BIT closer to the boom to the position where it is connected to the Stewart platform. The second set of tugger (white) lines is used to control the BIT's motions once the BIT is high above deck level, and the third set of tugger lines (yellow) is used to control the BIT's motions when it is close to deck level, where the influence of white set of tugger lines is minimal.

The capacity and power of the tugger winches falls out of the scope of this thesis project, hence they are not mentioned. However, it is recommended that the third set of tugger lines uses synthetic ropes, this aims to reduce the weight of the ropes on the BIT when the lines are slacked and the BIT is controlled by the white set of tugger lines.

In the installation process explained in Subsection 4.1.2, the tugger lines connected to the spreader bar (orange) are referred to as tuggers #1 and #2, the white set of tugger lines are referred to as tuggers #3 and #4, and the yellow set of tugger lines are referred to as tuggers #5 and #6.

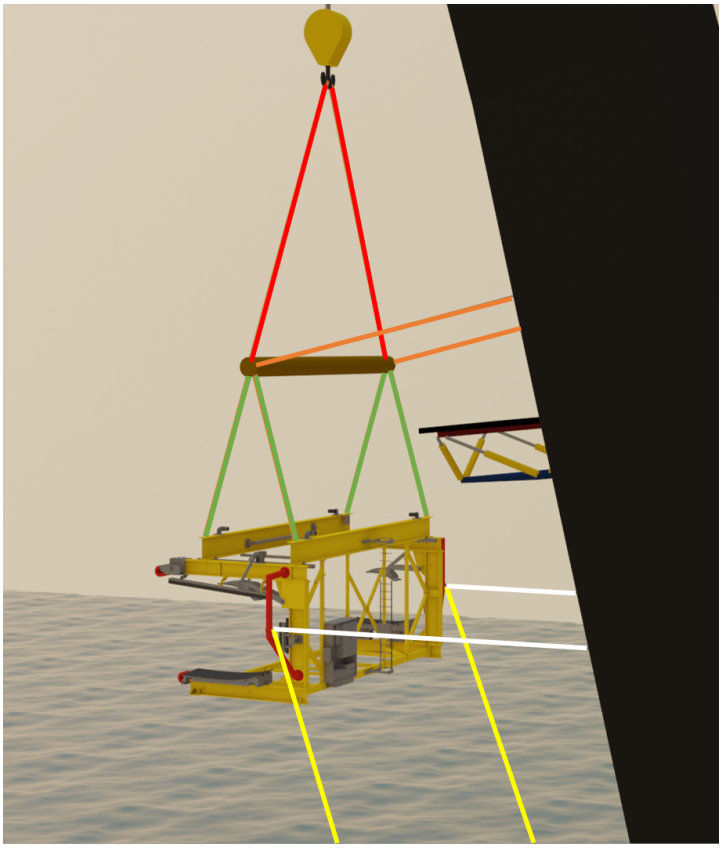

**Figure 4.5:** Tugger lines arrangement.

### 4.1.2. Task plan for blade installation

The scope of this task plan is to define the operational steps for blade installation with the motion-compensated Stewart platform. It starts with the connection of lifting devices (spreader bar and BIT) to the crane hook, the connection of the BIT to the blade, the connection of the BIT to the Stewart platform, the connection of the blade to the hub using the motion compensated Stewart platform, the disconnect of the BIT from the installed blade, the disconnect of the BIT from the Stewart platform, and finally the connection of the BIT to the second blade, where the previous steps are repeated.

As only the blade installation phase is detailed, the task plan starts considering that the following preliminary activities have already been concluded.

- Mobilization of all equipment and accessories, including mobilization of the Stewart platform on the crane boom, and the installation tower on the vessel deck.
- Load out of components from the feeder barge.
- The WTG's foundation is already installed.

- The preliminary activities have already been completed, such as removing the lifting frames from the blade racks so that the blade is free to be lifted, only secured by its seafastening.
- One WTG's tower is installed and no longer on the vessel's deck.
- The nacelle is already in position on the installation tower.

### Mobilization of the rigging arrangement

The blade installation operation begins with the mobilization of the rigging arrangement, that is, the spreader bar and the BIT. The crane hook is connected to the spreader bar, as well as tugger lines #1 and #2. The spreader bar is hoisted from deck level to the BIT, where it is connected to the BIT by two pairs of slings. Tugger lines #3, #4, #5 and #6 are connected to the BIT's arms. The final arrangement is depicted in Figure 4.5.

### BIT to blade connection

Once the spreader bar with the BIT is connected to the portside crane hook. The crane's configuration (boom and slew angles, and wire length paid out) is adjusted to position the BIT immediately aft of the 1$^{st}$ blade, in this stage the BIT's claws are fully open. Then, the BIT is connected to the blade, at its design position, and the claws are closed around the blade.


**(a)** BIT approach to blade - claws open.

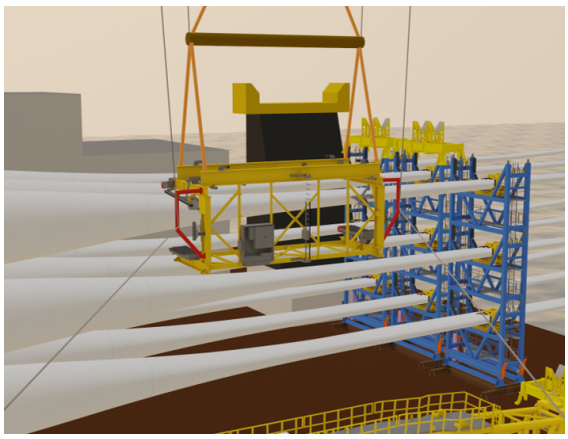

**(b)** BIT approach to blade - claws open.

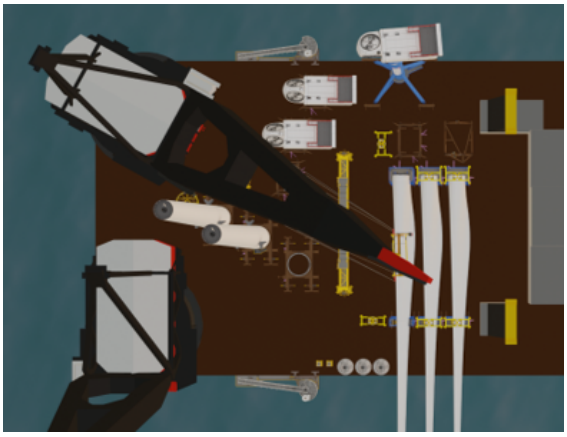

**(c)** BIT approach to blade - claws closed - top view.

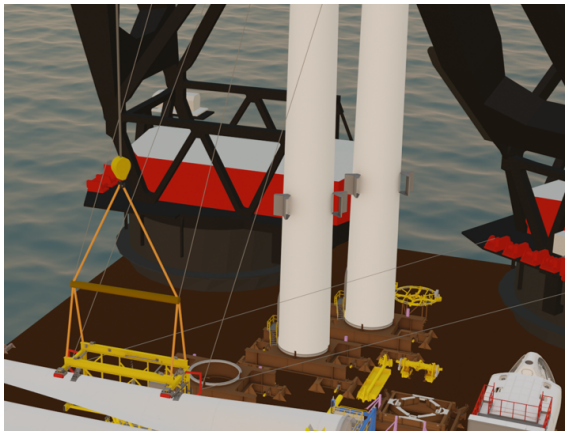

**(d)** BIT connected to blade - claws closed.

**Figure 4.6:** Connection of BIT to blade.

### Hoisting the blade for the Stewart platform connection

After the BIT is connected to the blade, both the blade's seafastening is released, and the Stewart platform support is folded to the BIT connection position. The Stewart platform's support must be in position before the blade is lifted; if there is an issue with the support's mechanism, it can be solved without having the blade hanging from the crane.

Once the Stewart platform support is in position and the blade's seafastening is released, the BIT is hoisted and tuggers #5 and #6 control the cargo, after the blade reaches a certain height, the cargo is controlled by tuggers #3 and #4, while tuggers #5 and #6 are slacked. The crane proceeds to lift the BIT while slewing counterclockwise and booming up until the blade is clear from the neighboring structures and in position to be connected to the BIT.

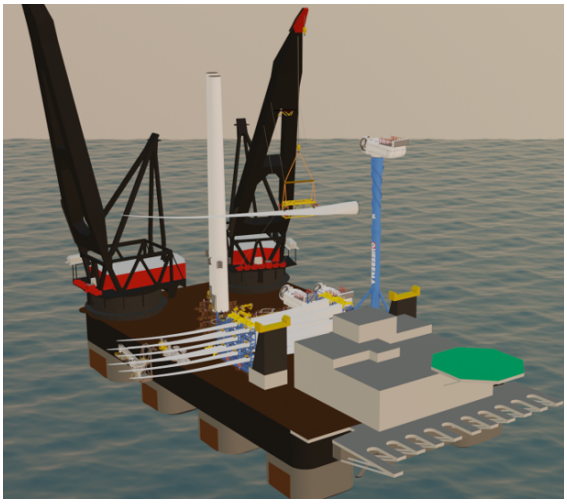

**(a)** Hoisting blade - tuggers #5 and #6 control BIT.

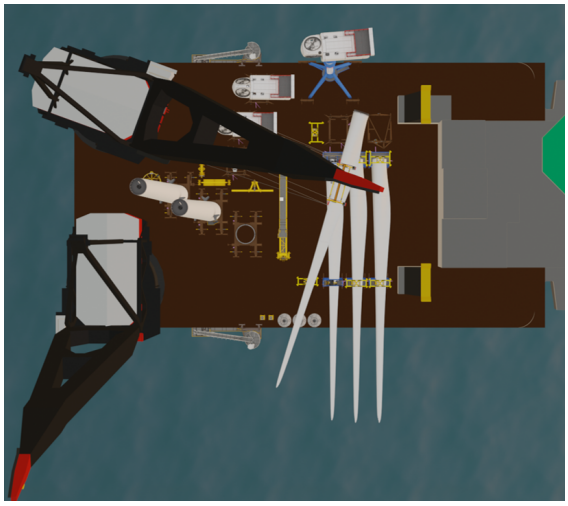

**(b)** Hoisting blade - tuggers #5 and #6 control BIT - top view.

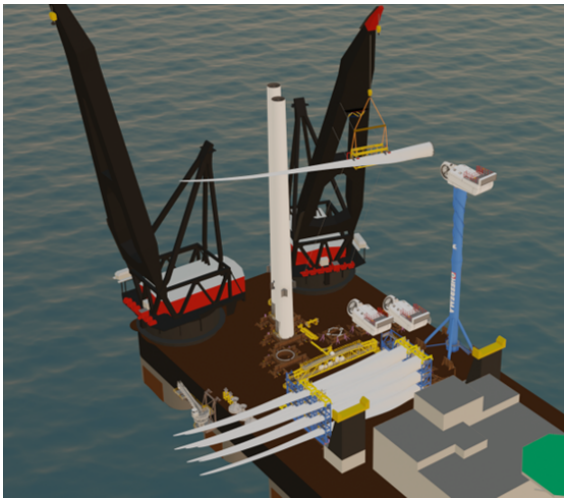

**(c)** Hoisting blade - tuggers #3 and #4 control BIT.

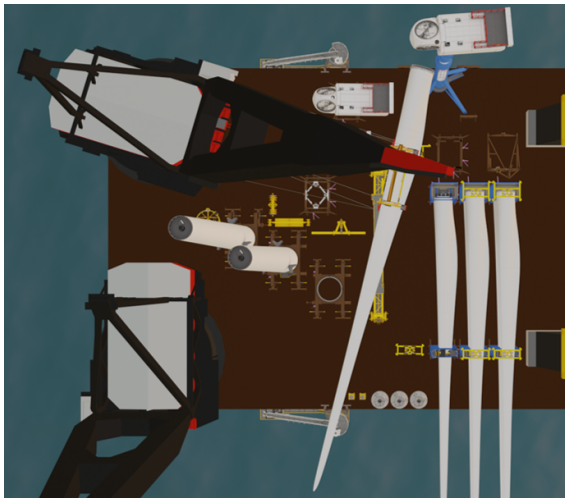

**(d)** Hoisting blade - tuggers #3 and #4 control BIT - top view.

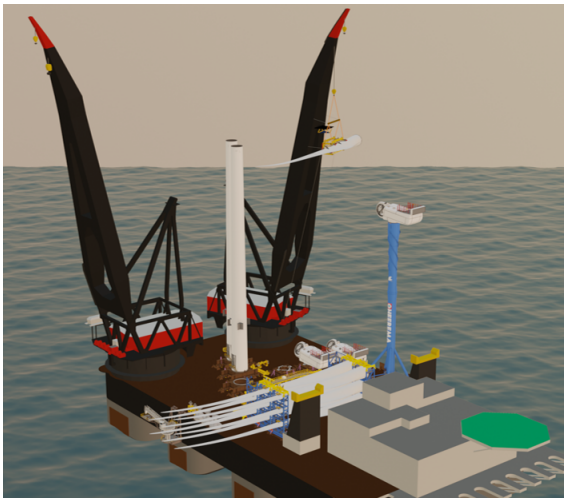

**(e)** Crane boom and BIT in position for the Stewart platform connection.

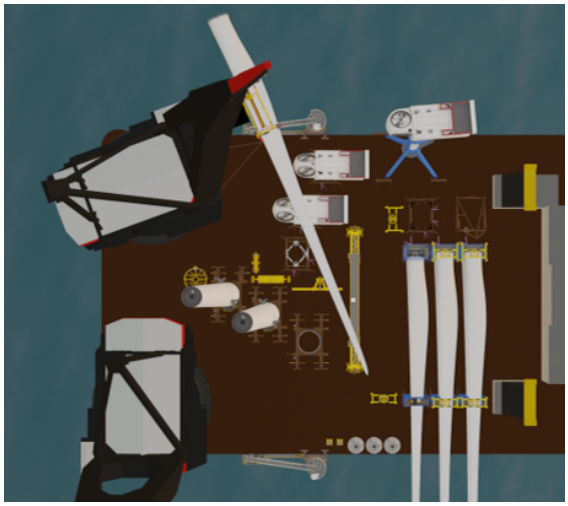

**(f)** Crane boom and BIT in position for the Stewart platform connection - top view.

**Figure 4.7:** Hoisting blade from the blade rack until to Stewart platform connection position.

### BIT connection to Stewart platform

The BIT is hoisted until the Stewart platform occupies the space between the BIT and the spreader bar. At this point, tuggers #1 and #2 pull the spreader bar towards the crane boom, bringing the BIT closer to the Stewart platform. Additionally, because the pendulum is formed between the sheave of the hoist wire and the spreader bar, the BIT remains horizontal without the risk of the blade sliding, as depicted in Figure 4.8b.

Once the BIT is in position, the Stewart platform is moved to the connection position and the parts are connected. After the platform is connected to the BIT, tugger lines #3, #4, #5 and #6 are slacked. Tugger lines #1 and #2 keep the minimum necessary tension to avoid large motions from the spreader bar; the same applies to the crane hook.

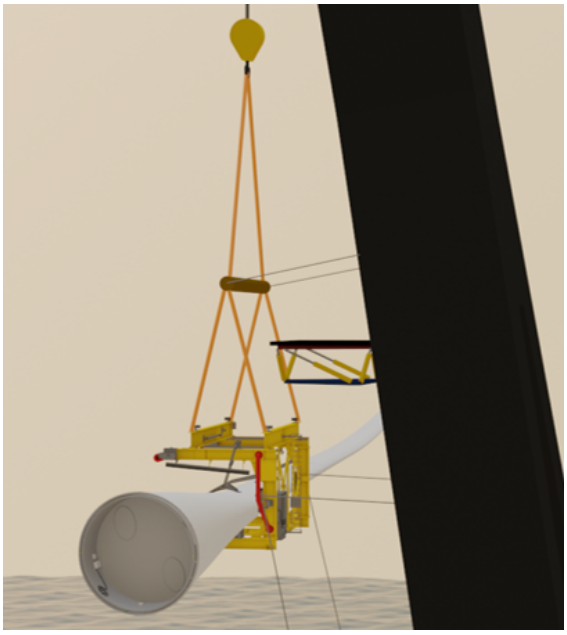

**(a)** BIT hoisted to the position for Stewart platform connection.

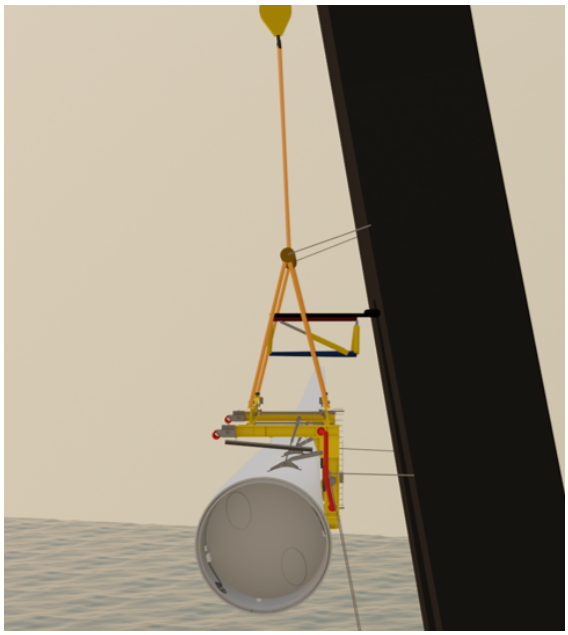

**(b)** Tuggers #1 and #2 pull the spreader bar towards the crane boom.

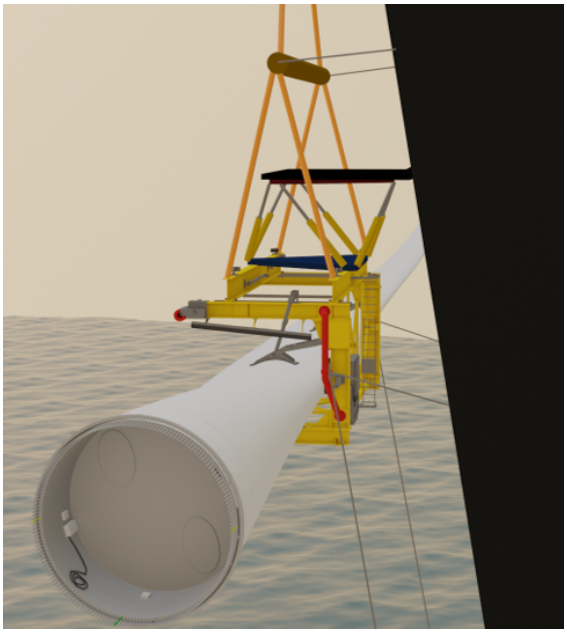

**(c)** Stewart platform extended and connected to BIT.

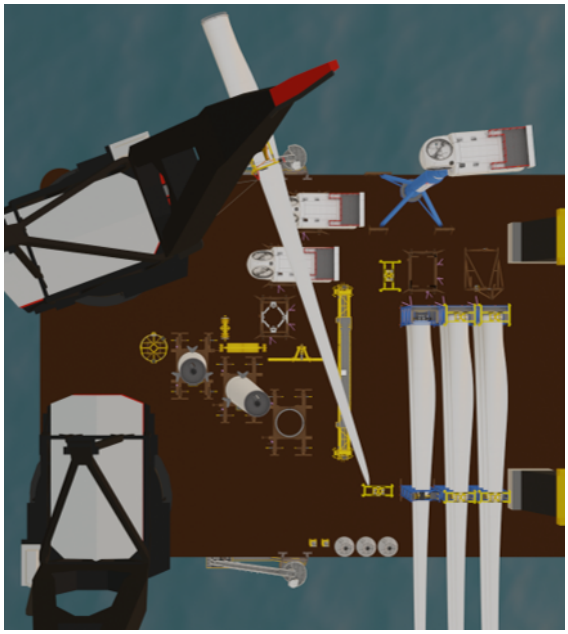

**(d)** BIT connected to blade - claws closed.

**Figure 4.8:** Stewart platform extended and connected to BIT - top view.

### Blade positioning for hub connection

At this stage, the BIT is connected to the Stewart platform. The crane's boom position is adjusted to place the blade root close to the hub, therefore, the crane slews clockwise, while the Stewart platform rotates counterclockwise about the $z-$ axis. Meanwhile, the crane also booms down, while the Stewart platform rotates about the $y-$ axis to keep the BIT aligned with the horizontal plane. Once the Stewart platform's limit to rotate about the $y-$ axis is reached, the crane stops booming down, and the support structure for the Stewart platform rotates towards its blade installation position while the Stewart platform rotates back about the $y-$ axis to keep the BIT aligned with the horizontal plane. This step is repeated once more until the crane booms down to the blade installation position.

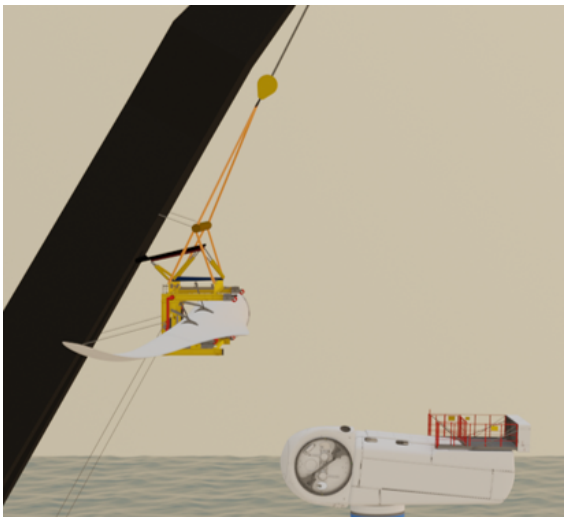

**(a)** Booming down and pitching the Stewart platform to keep the blade horizontal.

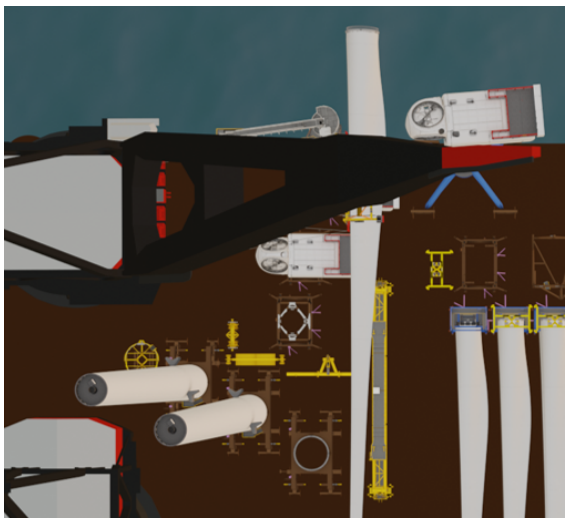

**(b)** Booming down - top view.

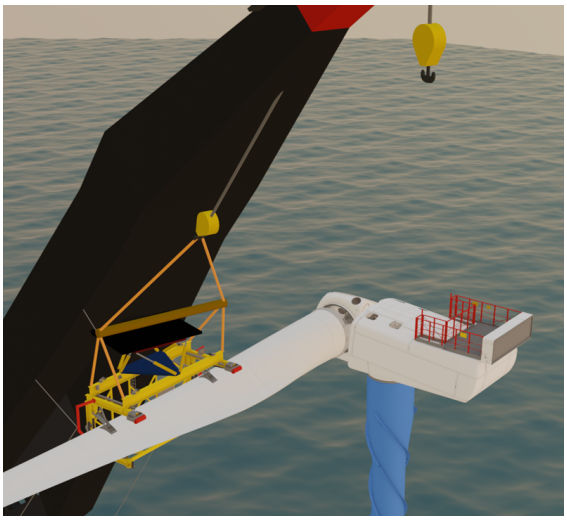

**(c)** Blade in position for the hub connection - Motion compensation system on.

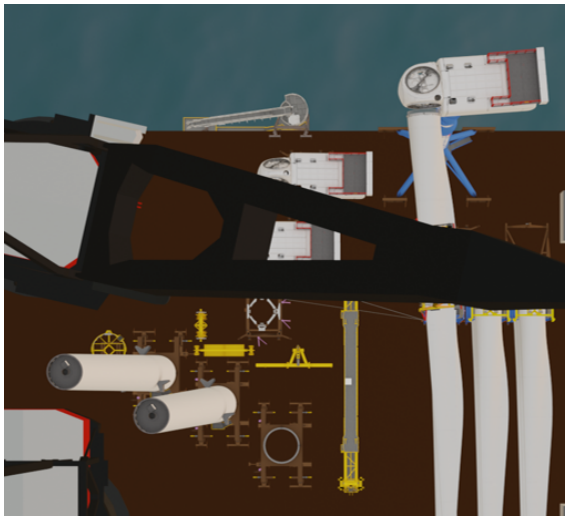

**(d)** Blade in position for the hub connection - Motion compensation system on - top view.

**Figure 4.9:** Positioning the blade for the hub connection.

### Connecting the blade to the hub

The blade root is now close to the hub, approximately 1.3 m. The motion compensation system is switched on, and the relative motions between hub and blade root are reduced. The sliding mechanism is activated, and the Stewart base slides sideways towards portside while the motion compensation system keeps functioning. Then the blade is bolted to the hub. The sliding mechanism concept is

presented in Section 4.2.

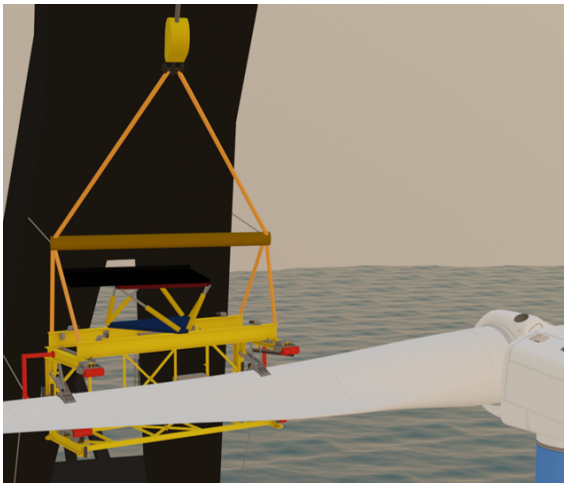

**(a)** Stewart base sliding sideways for the Blade x hub connection.

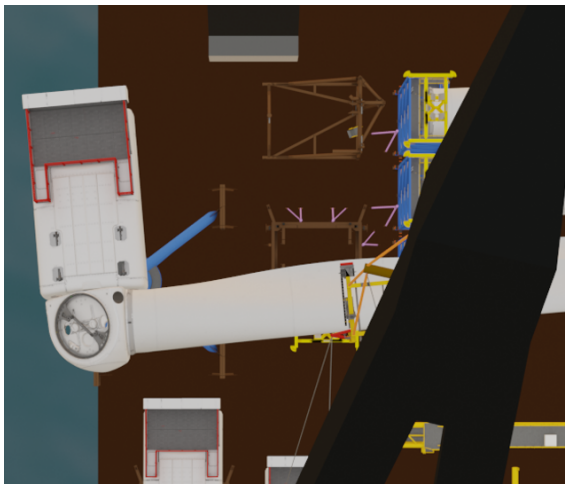

**(b)** Stewart base sliding sideways for the Blade x hub connection - top view.

**Figure 4.10:** Blade connection to hub - motion compensation system on.

### Disconnecting the BIT from the blade

Once the blade is attached to the hub, the claws of the BIT are open and the Stewart platform moves approximately 0.3 m down to increase the clearance between the blade and the internal parts of the BIT.

To completely free the blade from the BIT, the nacelle is yawed counterclockwise. Once the blade is free of the BIT, the crane booms up and the nacelle is yawed back to the previous configuration.

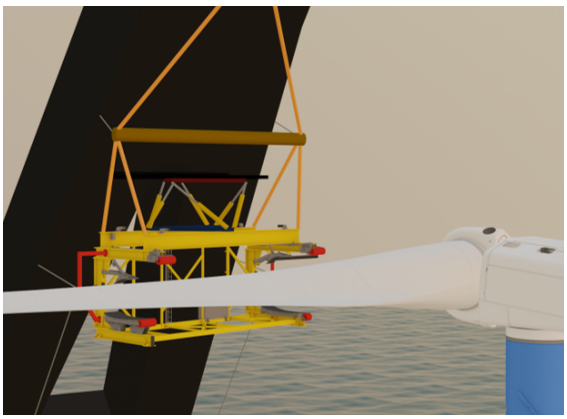

**(a)** Opening BIT's claws.

**(b)** Yawing the nacelle to free the blade from the BIT - top view.

**Figure 4.11:** BIT disconnection from blade.

### Rotating the hub for the 2$^{nd}$ blade installation

With the BIT disconnected from the blade, the rotor is spanned 120° counterclockwise, position for the second blade connection. With the rotor in that position, the port and starboard cranes uninstall the transportation skid of blade #1 from the blade rack, thus freeing blade #2 for installation.

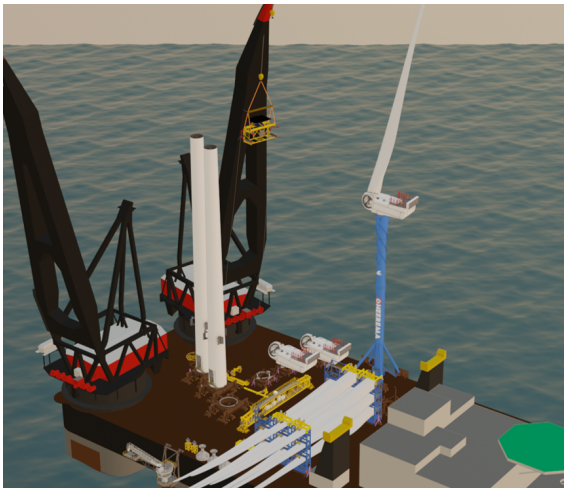

**(a)** Booming up, yawing the nacelle back, and rotating the hub for blade #2 installation.

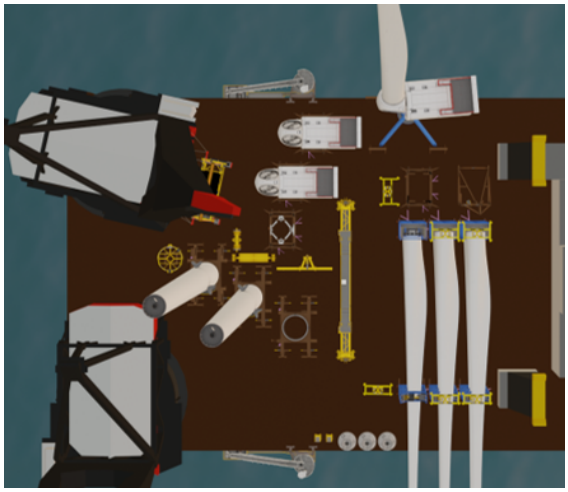

**(b)** Removing transportation skid of blade #1 to free blade #2 - top view.

**Figure 4.12:** Changing nacelle and hub's configuration for the installation of blade #2.

### Disconnect BIT from Stewart platform

To proceed with the installation of blades #2 and #3, the BIT must be disconnected from the Stewart platform, this is done by reversing the steps in the "BIT connection to Stewart platform" phase, Figure 4.8.

### Connect BIT to 2$^{nd}$ blade

Once the BIT is free from the Stewart platform and hanging from the crane hook, the BIT is positioned just aft of the 2$^{nd}$ blade, and the steps in "BIT to blade connection" are repeated. The BIT is now connected to the second blade, and the blade installation proceeds repeating the steps detailed previously.

### RNA installation

After the steps above are repeated twice, and all three blades are installed in the hub, the RNA is lifted from the installation tower with the portside crane and placed on the support structure of the wind turbine, previously installed with the starboard crane. Differently from the original concept successfully executed in the Arcadis Ost 1 wind farm, now there is a structure attached to the crane's boom, the Stewart platform. Possible interference of the Stewart platform with the RNA is verified.

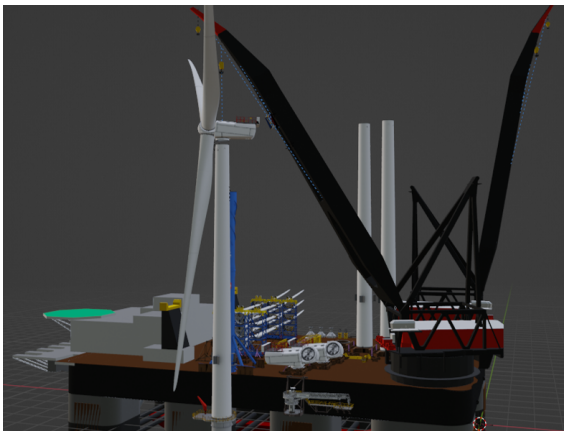

**(a)** RNA installation with Stewart platform attached to crane's boom.

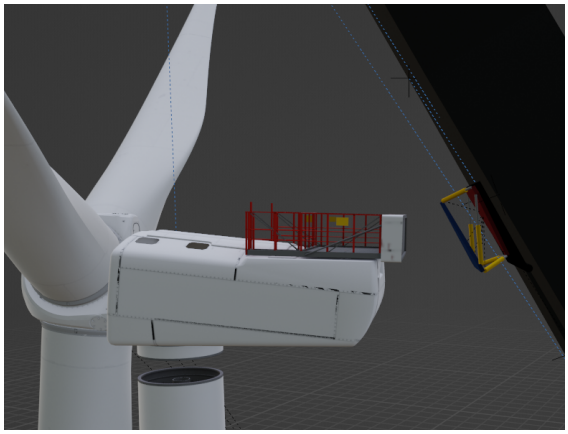

**(b)** RNA installation with Stewart platform attached to crane's boom - detail.

**Figure 4.13:** Clearance assessment of RNA and Stewart platform attached to crane's boom during final RNA installation.

Although Figure 4.13 shows that the RNA does not clash with the Stewart platform, this only happens because the platform is in its resting position, completely folded towards the crane's boom and fully retracted. Additionally, the RNA motions while hanging from the crane are not part of this thesis' scope, and the dynamic clearance between the RNA and the Stewart platform must be investigated, as well as motion control alternatives for the RNA. Furthermore, a more detailed design of the Stewart platform and its position on the crane boom can include the possibility of retracting the equipment between the legs of the crane boom, hence increasing the clearance between the RNA and the Stewart platform.

## 4.2. The mechanical system

In this section, the concepts of four mechanisms required for the development of the project are presented. They are: the cylinders joints, i.e. interface between cylinders and base / platform; the folding mechanism for the Stewart platform's support on the crane boom, the sliding mechanism between the Stewart base and its support on the crane boom, mechanism used to slide the base sideways and connect the blade to the hub; and finally the connection mechanism between BIT and Stewart platform.

### Joints

As described in Section 3.9, the joints selected for both base and platform level are joints with two degrees of freedom. For simplicity and robustness, a Cardan joint is selected; they are versatile, abundant in the market, easy to replace and can easily be connected to a hydraulic cylinder and a different structure using, for example, out of shelf flange terminations. Figure 4.14 provides and example of a Cardan joint with flange terminations.

**Figure 4.14:** Cardan joint as interface between cylinders and base / platform [36].

### Support structure folding mechanism

The folding mechanism is used to tilt the support structure mobilized on the portside crane boom, where the Stewart platform is mounted. This mechanism allows the Stewart platform to retract and be parallel to the crane boom when not in use; it also provides a wider range in the Stewart platform workspace so that the BIT can be connected to the Stewart platform with the crane boom angle at its maximum, reducing the required load of tuggers # 1 and # 2, and eliminating the need to tilt the BIT with the blade.

The support structure is connected to the crane boom with a hinge, around which the structure can rotate; therefore, the support structure can be moved parallel to the crane boom, as in Figure 4.15a, or positioned for blade installation, as in Figure 4.15b. A pair of motors drive Gear 1 directly or through a gearbox that rotates Gear 2. Gear 2 is made of a section of a circle with at least 120°. As Gear 2 is mounted on the support structure, turning Gear 1, will turn Gear 2, which will fold the support structure.

To avoid that the motor turning Gear 1 has to be functional during all times, or to demand high loads on its braking system, a locking pin activated by a small hydraulic cylinder is used in combination with a truss on the support structure, to lock the support structure in predefined tilting angles.

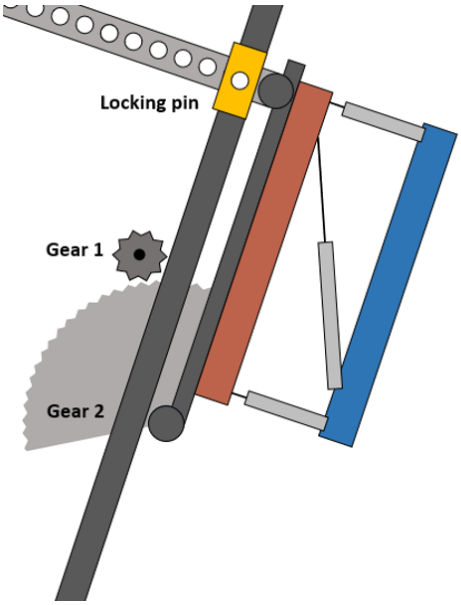


**(a)** Support structure folding mechanism fully retracted.

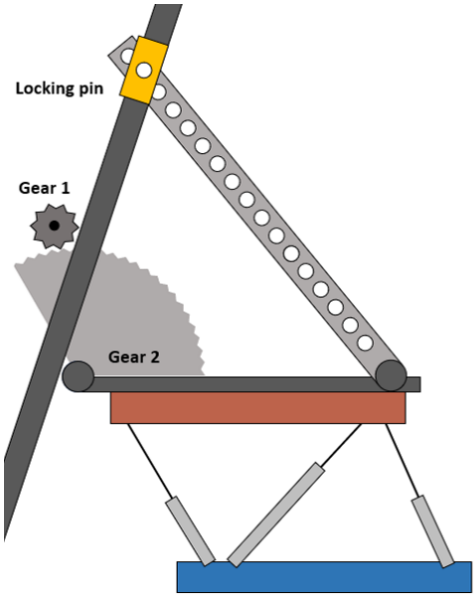


**(b)** Support structure folding mechanism in position for blade installation.

**Figure 4.15:** Stewart platform's support on crane's boom with folding mechanism.

### Sliding mechanism of the base

The sliding mechanism of the base is responsible for sliding the Stewart base sideways for the blade connection phase. By moving the base sideways, the motion control system of the Stewart platform can be simplified, this because any possible misalignment between blade and hub during the stabbing phase will cause an increase of load on the sliding mechanism, which is easier to identify. for the sliding mechanism, the support structure must contain two cuts, from which two pad eyes from the Stewart base pass through. On top of the support structure, two hydraulic cylinders connect the support structure to the Stewart base pad eyes.

To activate the sliding mechanism, the cylinders are extended simultaneously, and the base of the Stewart platform moves sideways. The base of the Stewart platform is attached to the support structure via tracks.

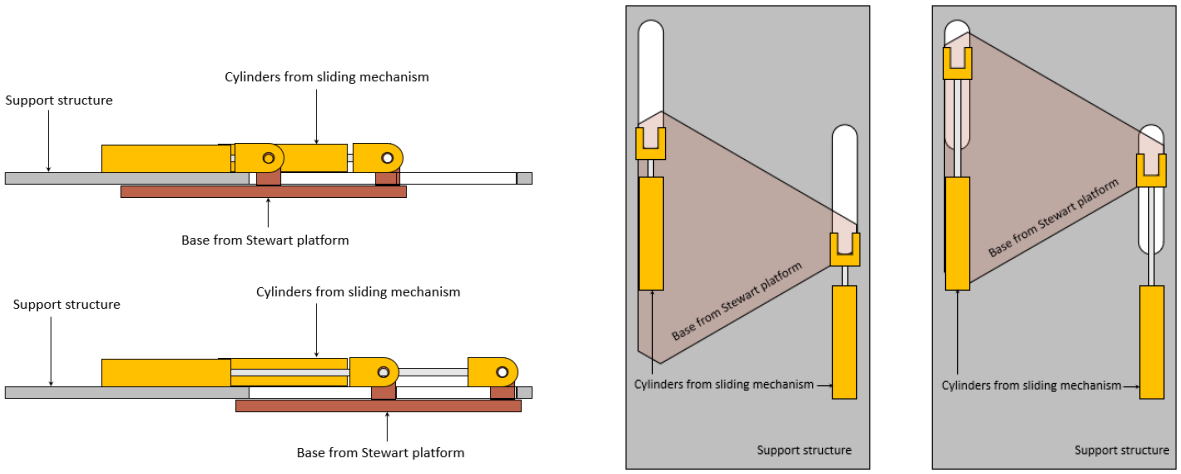


**(a)** Front view sliding mechanism - upper in neutral position and lower in stabbing position.

**(b)** Top view sliding mechanism - left in neutral position and right in stabbing position.

**Figure 4.16:** Sliding mechanism from the Stewart platform base - Stewart platform and actuators omitted for clarity.

The base sliding mechanism is designed to be on top of the support structure to allow easy access and maintenance; nevertheless, it will impose a spatial limitation to the folding mechanism.

### BIT and Stewart platform connection system

The concept for the BIT and platform connection system is elaborated with some main objectives. The first one is that the system is simple and robust, while allowing only minimal mechanical looseness between the parts. The system has two main parts; the first one are the locking pins, a total of three locking pins are individually actuated by three separate hydraulic cylinders, this part of the system is mounted on the Stewart platform. The second part of the system are the alignment posts, they are two posts (with different heights) with conical points that are fixed to the BIT's top face. Once the Stewart platform is lowered for the connection, these posts enter the conical hole on the platform providing the primary alignment between the Stewart platform and the BIT. Continuing to lower the Stewart platform, and the BIT's pad eyes will be lined up with their corresponding cuts on the Stewart platform. When the Stewart platform is lowered to the connection position, the BIT pad eyes will enter the platform's cuts. A general representation of the Stewart platform and BIT systems is presented in Figure 4.17.

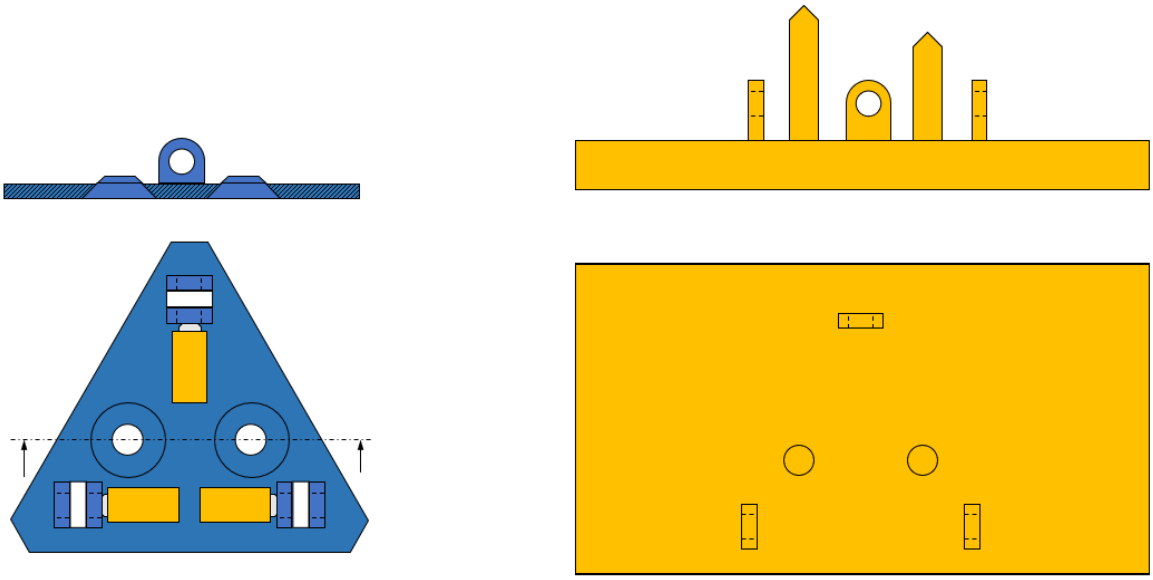

**Figure 4.17:** General arrangement of the BIT x Stewart platform connection system. Stewart platform on the left, and BIT on the right.

The BIT connection to the Stewart platform is simple; once the BIT is positioned roughly under the Stewart platform, the latter is lowered until the BIT's highest post starts entering its corresponding hole on the Stewart platform, the lowering process proceeds and the BIT's shortest post enters its corresponding hole on the Stewart platform. At this stage, the BIT is completely aligned with the Stewart platform, the platform's lowering process continues, and the BIT's pad eyes enter their corresponding holes on the Stewart platform, now the BIT's top face is matching the Stewart platform's bottom face. The three locking pins are extended, and the BIT is fully connected to the Stewart platform. It is important to point out that the locking pins have conical tips to facilitate the process of going through the three pad eyes each. The connection procedure between the BIT and the Stewart platform is presented in Figure 4.18.

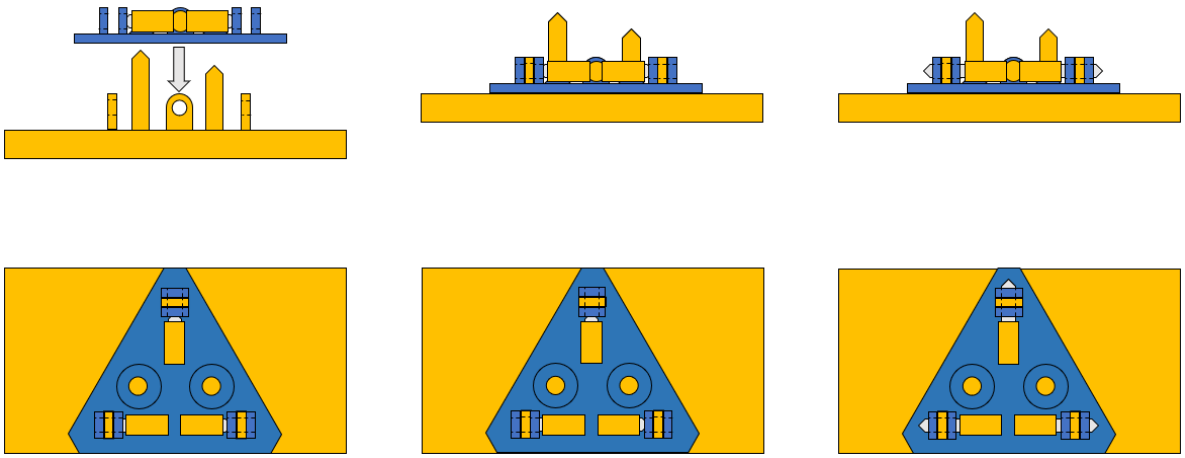

**Figure 4.18:** Schematic representation of the BIT x Stewart platform connection system.

The concept of the mechanisms proposed in this section may not be the optimal solution for the specific application. The purpose of this section is to present possible solutions for the operation. Other alternatives should be explored and / or detailed.

# 5

# Tracking the objects

The prospective model-free control system to control the Stewart platform starts by measuring the motions that will be compensated for, that is, the relative motions between hub and blade root. These motions are the input of the control system, therefore measuring and processing these motions become a fundamental part of the motion control system.

The instrumentation to measure the hub's motions must allow the calculation of the relative motions between hub and blade root, or directly measure them. It is important to point out that one of the main goals of this model-free control system is to be applicable in a wide range of scenarios, hence, at first, all three translations and three rotations of the hub are assumed to be measured. And for this reason an accurate and reliable motion tracking set-up must be specified considering the instrumentation's accuracy, sampling rate, and operational characteristics.

## 5.1. Sensors

To measure the hub's motions in all six degrees of freedom, different types of instrumentation are assessed, the selected options are chosen because of their known quality, applicability, industry knowledge, costs, and robustness for the application in an offshore environment.

From the Orcaflex simulations performed in Section 2.1 and summarized in Table 2.4, the hub motions have a relatively small amplitude, therefore the instrumentation selected must not heavily compromise the quality of the data, i.e. the sensors accuracy values shall be small when compared to the motion's amplitude.

Taking into account the above mentioned requirements, the following sensors are selected to form three different motion tracking sets-ups, initially to measure both hub's and blade's motions, individually or relative to one another.

- Total station and reflectors using the LDV (Laser Doppler vibrometer) principle.
- Laser.
- Real-time kinematics (RTK).
- Gyroscope.
- Motion reference unit (MRU).

The devices listed above are compared and selected from different suppliers based on their applicability and technical characteristics. Additionally, they may not be capable of measuring all six degrees of freedom, therefore different combination of sensors are assessed in Section 5.2. The specific cost

of the product is not taken into account in this process.

**Table 5.1:** Sensors performance parameters

| | Accuracy | Sampling frequency or period | Reference |
|---|---|---|---|
| Total station | 1”, 2 mm + 1.5 ppm | 0.8s | [37] |
| | 0.5”, 0.6 mm + 1 ppm | 2.4s | [38] |
| Laser | 1 mm | 50Hz | [39] |
| RTK | 6 mm | Up to 200 Hz | [40] |
| Gyroscope | 0.008° | Up to 200 Hz | [41] |
| MRU | 0.008° | Up to 200 Hz | [42] |

The accuracy figures presented in Table 5.1 are in the form of 67% standard deviation with zero mean following a Gaussian distribution, where the distance accuracy for the total stations has a fixed value (2mm or 0.6mm) plus an additional factor that is a function of the distance between the total station and the prism in the order of magnitude of parts per million. Additionally, the angular accuracy of the total station’s readings, in seconds, i.e. degrees divided by 3600, represents the accuracy while measuring the angle formed by the two lines between the total station and two prisms.

Other technologies, such as optical motion capture, are not considered due to possible operational issues. This includes missing readings due to marker obstruction [43], high noise and poor accuracy when markers are not in the cameras’ calibration envelope [44], requirement of multiple cameras, and poor performance in environmental conditions that are common offshore, for example, fog, poor lighting, rain, etc. Other options could be technologies such as radar based relative positioning sensors used as DP (Dynamic Positioning) references, however they are not applicable, RADius, a radar based system from Kongsberg, has an accuracy of $\pm$ 0.25 m in the standard deviation [45], therefore not being suited for the application.

In this section different instrumentation devices to measure, directly or indirectly, the relative motions between hub and blade root are specified. Those will be combined into different set-ups in order to cover all six DoF, then the performance of these set-ups will be assessed in terms of total propagated uncertainty, sampling frequency, post processing, and operational applicability to the system.

## 5.2. Measurement set-ups

From the selected instrumentation, three different set-ups are evaluated. They are detailed in the following subsections.

### 5.2.1. Set-up 1 - Total station mounted on the hub pointing towards the blade root

Set-up 1 is specified so that the final measurements directly yield the relative motions between hub and blade root. In this set-up, a total station is mounted directly inside the hub and points towards the blade root, where three prisms are mounted in a circumference, the three prisms are equally spaced.

The total station mounted inside the hub aims at the three reflectors in the blade root, and by constantly measuring the distance between the prisms and the survey equipment, as well as the angles between the lines formed by each prism and the total station, it is possible to calculate the blade root’s position in space relative to the total station, i.e. the hub. This approach only works if the prisms are not colinear; therefore, the requirement of proper prism arrangement in the blade root. The schematic of set-up 1 is presented in Figure 5.1, where the red triangle in the top view represents the working set-up.

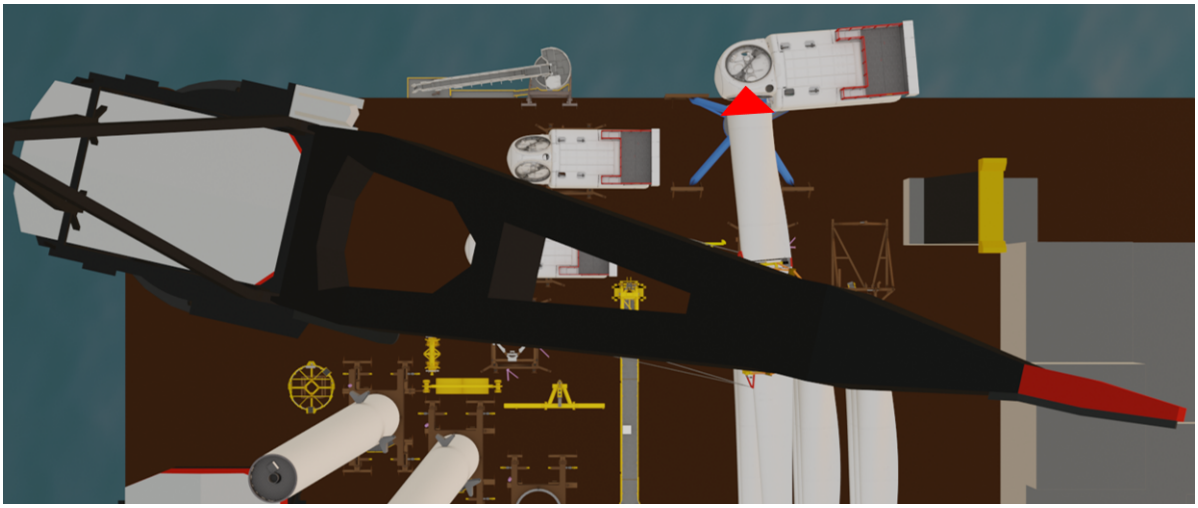

**Figure 5.1:** Motion tracking - Set up 1.

Regardless of the low sampling frequency of the total station system presented in Table 5.1, some problems may arise while using this set-up. The first one is the occurrence of speckle and shot noise when the total station is mounted on a moving object, e.g., the hub, [46] [47]. [48] successfully simulated the speckle noise when the laser head is mounted on a moving surface and proved that it grows with surface roughness to a critical value, therefore manufacturer-specified prisms are specified to overcome this issue.

Another consideration regards the operational aspects of this set-up. The prisms in the blade root must be fixed there and surveyed so their position in the blade reference system is known with accuracy, so it would be recommended that this task is performed in advance, away from the critical installation path, ideally onshore. Nevertheless, lifting operations done with the blade, and an occasional accidental light impact may slightly move the prisms from the surveyed position, and this will influence the final relative motion readings. The same applies to the total station inside the hub. Additionally, these equipment must be retrieved once the blades are installed, that is the prisms and the total station.

### 5.2.2. Set-up 2 - Individual combination of sensors for hub and blade root

Unlike set-up 1 that directly measures the relative motions between blade root and hub, set-up 2 is specified to individually measure all six degrees of freedom from both hub and blade. Two RTK devices, one on the BIT and another on the hub or nacelle, measure the bodies' motions in $x-$ and $y-$ directions. Two gyroscopes, one on the BIT and the other on the hub / nacelle, measure the bodies' yaw (rotation about the $z-$ axis). Two MRU's, again with one mounted on the BIT and the other on the hub / nacelle, measure the individual rotations about the $x-$ and $y-$ axes, respectively roll and pitch. Finally, two laser devices mounted on deck point upwards at the hub and blade root are used to measure these bodies motions in the $z-$ direction.

The schematic from set-up 2 is presented in Figure 5.2 where the sensors are represented by the red squares on the nacelle and BIT, and the laser device on the deck pointing upwards towards the hub (red square and dashed red line), the laser measuring device for the vertical motion of the blade is omitted for clarity.

**Figure 5.2:** Motion tracking - Set up 2.

It is important to point out that the sensors must be retrieved from the parts, therefore, the RTK device, MRU and gyroscope are mounted on the BIT, and not the blade root. This also allows that the same equipment is used for several blade installations, while if the sensors were mounted on each blade, at least three different sensors' assembly would be required, one for each blade. Another important factor is that the RTK device must not be obstructed, so placing it inside the blade, where it could be recovered once the blade is bolted to the hub, is not an option.

Unlike set-up 1 where the relative motion between the blade root and the hub is measured directly, in set-up 2, the hub and the blade motions are independently measured in their own local coordinate systems. Hence, their relative motions in a common reference system must be calculated.

### 5.2.3. Set-up 3 - Total station mounted on crane's slew platform measuring the BIT's motions, and set-up 2 to measure the hub's motions

The third set-up, depicted in Figure 5.3, also uses individual systems to measure the hub's motions exactly like in set-up 2, but the blade's motions are measured using a total station mounted on the crane's slew platform pointing towards the BIT, where three prisms are mounted.

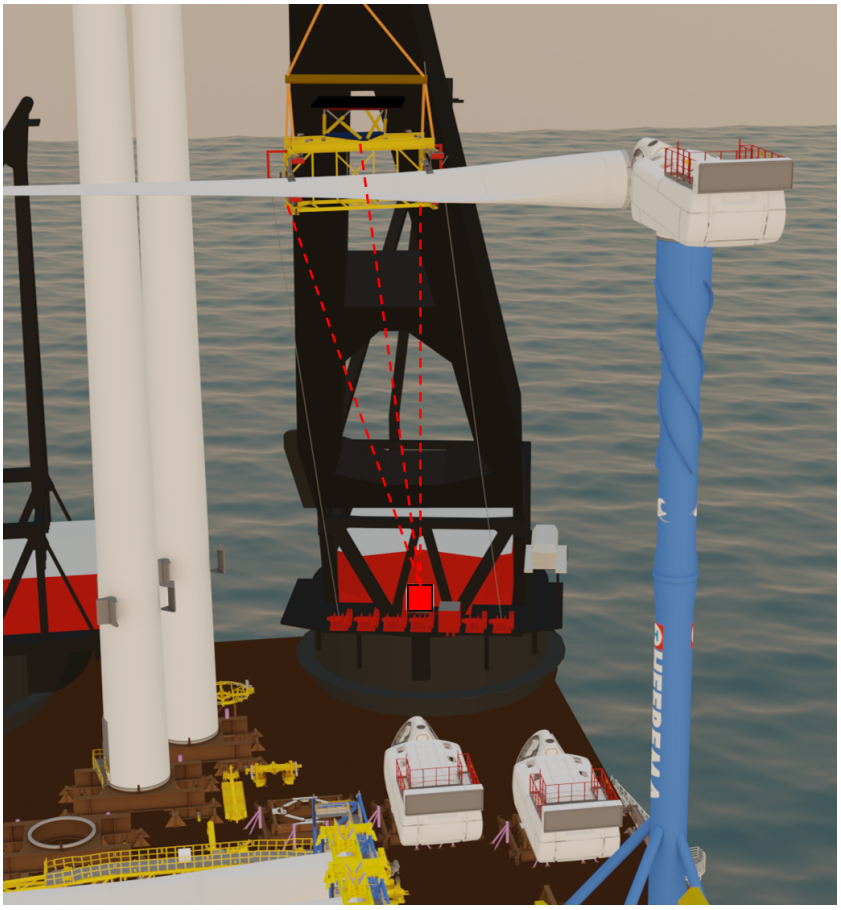

**Figure 5.3:** Motion tracking - Set up 3.

From the distance between the total station and the prisms, as well as the angles formed by the lines connecting the measuring equipment and the reflectors, it is possible to construct a plane in space with the BIT's position and orientation in the total station reference system, i.e. the crane's slewing platform reference system. Once again, there is the restriction that the prisms on the BIT must not be colinears.

In practical terms, two problems arise when measuring the blade's position with prisms on the BIT and the total station mounted on the crane's slewing platform. The first one is that if one single prism is obstructed, the BIT's position and orientation, and consequently the blade's, can no longer be calculated. The second point of concern regards contactless measuring long distances on a vessel; although the vessel is extremely stiff, over a long distance small vessel deformations may become an issue, especially when considering the required accuracy to measure the BIT's motions. The stiffness and behavior of the vessel, which will influence the final BIT's motion readings, are also influenced by the deck cargo distribution, ballast configuration, and other factors.

## 5.3. Total propagated uncertainty

Once the three different measuring set-ups are specified, the accuracy of their sensors is simulated into the hub motions obtained from the OrcaFlex runs. Generally, every simulated measurement follows the following equation:

$$X_s = X + \mathrm{rnd}(\sigma) + X \cdot ld \tag{5.1}$$

Where $X_s$ is the simulated measurement considering the specific measurement accuracy of the

instrumentation, $X$ is the original value from the Orcaflex simulations, rnd$(\sigma)$ is a random number generated with zero mean and standard deviation corresponding to the sensor performance parameter in a Gaussian distribution. Additionally, for the total stations only, the term $X \cdot ld$ indicates the error created by the additional factor that is characteristic of the total stations, from Table 5.1, 1.5ppm and 1ppm.

To calculate the total propagated uncertainty, the positioning of the devices is also considered. In Set-up 1, a 0.25mm error is randomly added or subtracted from the prisms and total station positions, and a 0.25° error is also randomly added or subtracted from the total station's orientations. This is done to simulate the machining tolerances of the equipment or sensors' mounting supports. The same approach is applied for sets 2 and 3 with the same reference values (0.25mm and 0.25°).

The performance of the three different set-ups is assessed in terms of total accumulated standard deviation of the position error between blade root and hub, as well as the influence of one degree of freedom error on another, for example, the error while measuring the BIT's roll influences the blade root vertical motion error. Constant deviations are not considered in this evaluation, as they can be easily observed due to previous knowledge of the static condition of the system.

The accuracy of all instrumentation is simulated in the hub motions taken from all 30 load cases, Table 2.2, using the configurations of Set-ups 1, 2, and 3. Next, the propagated error from the specific set-ups is calculated to the points of interest, i.e., blade root and hub flange, considering that the Stewart platform perfectly compensates the hub motions to keep a constant distance between blade root and hub. The standard deviation of the positional error caused by the accuracy of the sensors is presented in Figures 5.4 and 5.5.

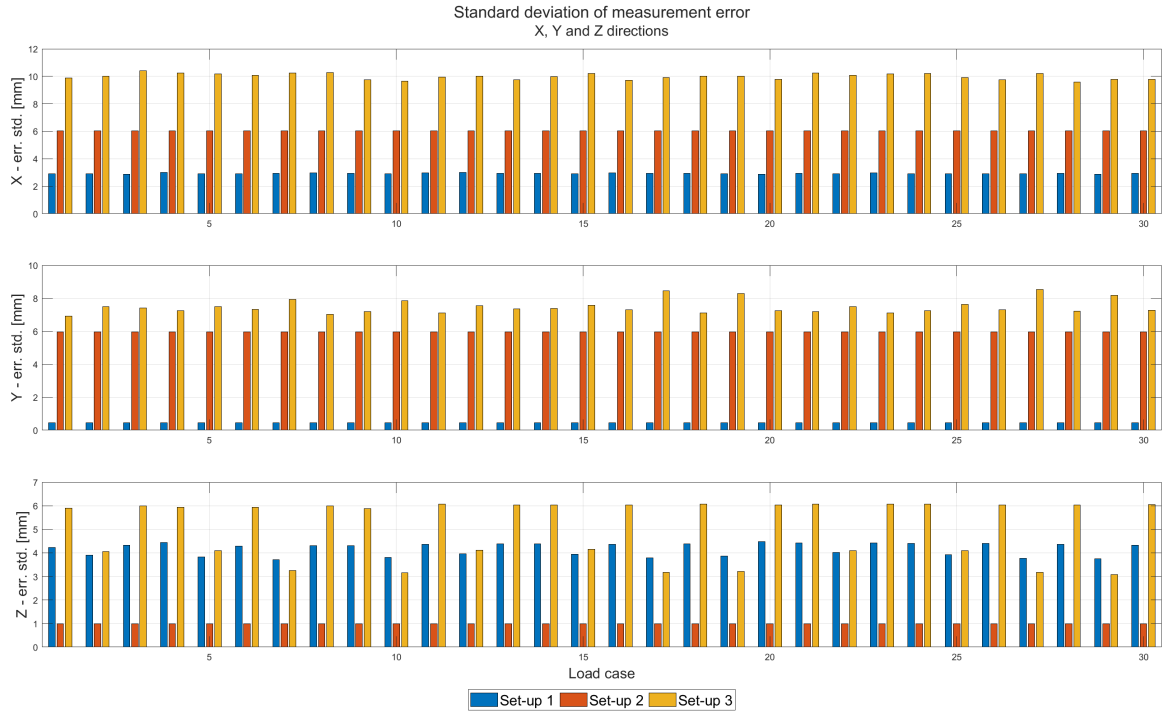


**Figure 5.4:** Accumulated standard deviation of position error between blade root and hub in X, Y and Z directions for the three different measuring set-ups.

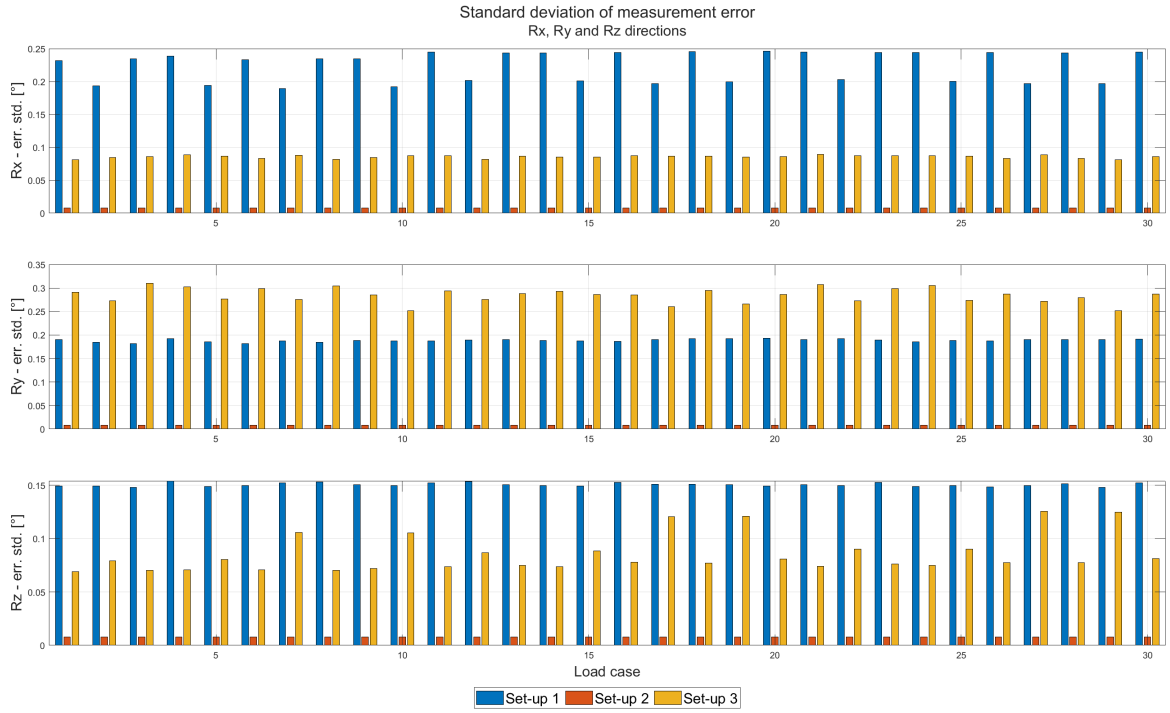


**Figure 5.5:** Accumulated standard deviation of position error between blade root and hub in Rx, Ry and Rz directions for the three different measuring set-ups.

It can be observed from Figures 5.4 and 5.5 that the standard deviation of the error for set-up 2 remains nearly unchanged in all degrees of freedom for all load cases, with overall best performance while measuring rotations and motion in the $z-$ direction. From Figure 5.5 it is also concluded that the use of a total station to measure the rotations result in a poor performance when compared to set-up 2 that has dedicated sensors for that. In set-up 3, measuring the motions in $x-$ and $y-$ directions result in the overall worst performance due to the characteristics of the total station while measuring long distances, opposing the performance of set-up 1. It is also observed that the standard deviation of the error measuring the motions in the $z-$ direction with set-ups 1 and 3 follows the trend of the motions' amplitudes, i.e. the larger the amplitude, bigger the error.

## 5.4. Final motion tracking set-up

Nevertheless, not only the accuracy performance indicators are considered in the choice of the final motion tracking set-up, factors such as sampling frequency, output information, and operational considerations are taken into account. For the latter, the set-ups were specified to enable an easy retrieval of the sensors and accessories after the blades are installed, the issue becomes when the accessories must be pre-assembled, for example, prisms mounted on the blade root (set-up 1) in port that can be damaged or knocked out of place somewhere between the port and the blade installation phase.

The sensors sampling frequency also plays an important role; the OrcaFlex simulations also provide the frequencies in which the hub motions occur, very low frequency due to wind influence, wave peak frequency, and installation tower's natural frequencies in Table 2.3, as depicted in Figure 2.4. Therefore, it is important that the sensor sampling frequency is at least double of the frequencies observed in the PSD plots with significant influence. Thus, from Figure 2.4 and the data presented in Table 5.1, it is possible to conclude that the total stations do not provide a sampling frequency high enough to be used in the proposed application.

Another important factor is the output data format, while the RTK, MRU, gyroscope, and laser pro-

vide direct measurements of their corresponding degree of freedom, with the total station (set-ups 1 and 3) the position and orientation of the part must be calculated from the angles and distances measured by the total station. This process requires solving a non-linear system of nine equations with nine unknowns, which requires a reasonable computational effort and adds a delay to the final data, hence being another downside of the total station when time is critical to enable real time motion tracking and compensation.

The option becomes to use individual combination of sensors providing adequate sampling frequency, reasonably good accuracy measuring all six degrees of freedom, and being easy to work with. Instruments can be mounted on predefined structures on the nacelle and on the BIT.

However, a fourth option is considered. Motion control strategies of Stewart platforms [26] [27] may assume that the controllable platform's position and orientation may not be updated and confirmed; hence only the target's motions must be measured, in this case the hub. This approach simplifies the motion tracking set-up and only the hub's motions are measured. Additionally, as detailed in Sections 2.2 and 2.3, the influence of the blade and crane in the relative motions between hub and blade root can be neglected when compared to the hub's motions. Hence only the hub motions are measured in the final set-up. The final motion measurement set-up used to generate the Stewart platform actuators' set-points is defined as follows:

- BIT / blade: not measured to generate the Stewart platform actuators' set-points.
- Hub: Motion in $x-$ and $y-$ directions measured with RTK. Motion in $z-$ direction measured with a laser device mounted on deck point upwards at the hub. Rotation about $x-$ and $y-$ axes (roll and pitch respectively) measured with a MRU. Rotation about the $z-$ axis (yaw) measured with a gyroscope.

## 5.5. Measurements simulations and filtering

Once the measurement set-up is defined, noise is added to the hub motions simulated in OrcaFlex using Equation 5.1. For these measurements to be used as set-points in the control system, they need to be filtered in order to reduce the noise influence in the performance of the motion compensation control system.

From the hub motions obtained from the OrcaFlex simulations, the response's frequencies are easily identified as the installation tower's first natural frequencies, the wave excitation frequency, and a response in low frequency due to wind. Therefore, a low-pass filter becomes a good candidate to reduce the sensors noise in the control system.

A Butterworth low-pass filter is designed with different orders and cut-off frequencies. The noise signal from the hub then passes through the filter, and the result is compared with the original hub motions from Orcaflex.

A total of 32 filters are designed, combining the following filter's orders and cut-off frequencies:

- Filters orders: 1$^{st}$, 2$^{nd}$, 3$^{rd}$ and 4$^{th}$
- Cut-off frequencies: 1Hz, 2Hz, 4Hz, 6Hz, 8Hz, 10Hz, 15Hz and 25Hz

Load case 29 is used to assess the filter's performance, this load case is chosen because it presents the overall largest amplitude in either $x-$ or $y-$ directions as presented in Table 2.4. Noise is added to this load case's hub motions, then it passes through the 32 possible combinations of filter order and cut-off frequencies. The results are compared with the original hub motions in terms of the error standard deviation, as well as the with unfiltered noise. Figures 5.6 and 5.7 depict the performance of the different filters designs for hub motion in the $x-$ direction in load case 29. From the figures it is confirmed that the higher the filter order, smoother the signal, however, higher filter orders introduce a larger phase shift.

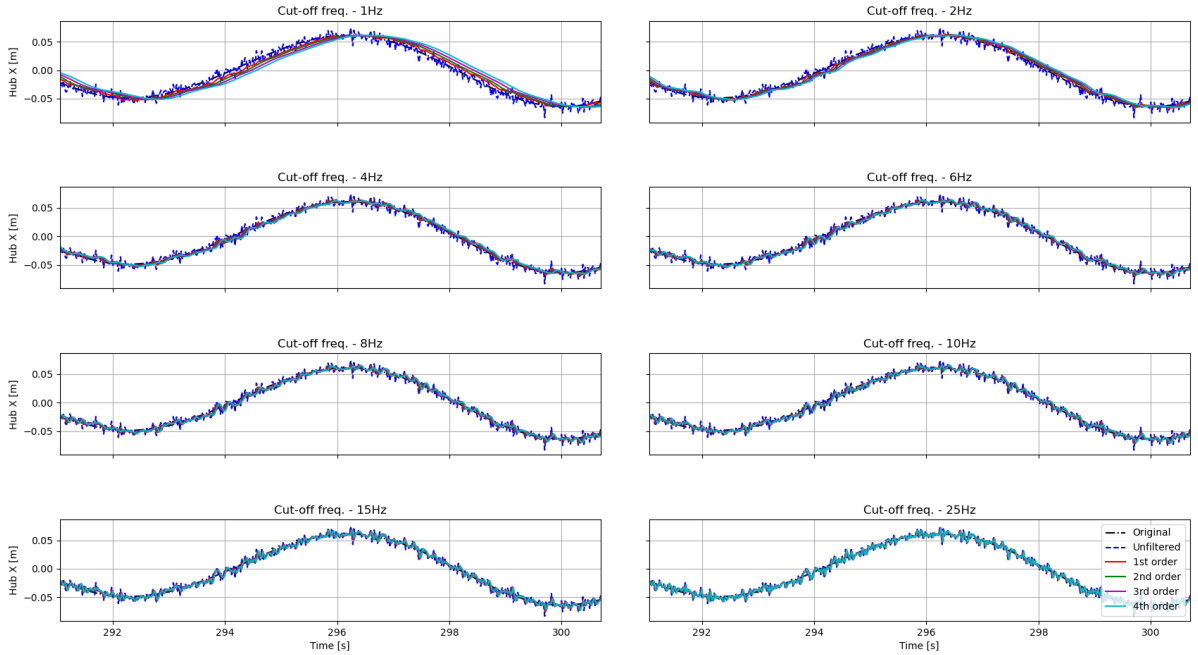


**Figure 5.6:** Sample of filtered and original hub motion in X direction - Load case 29.

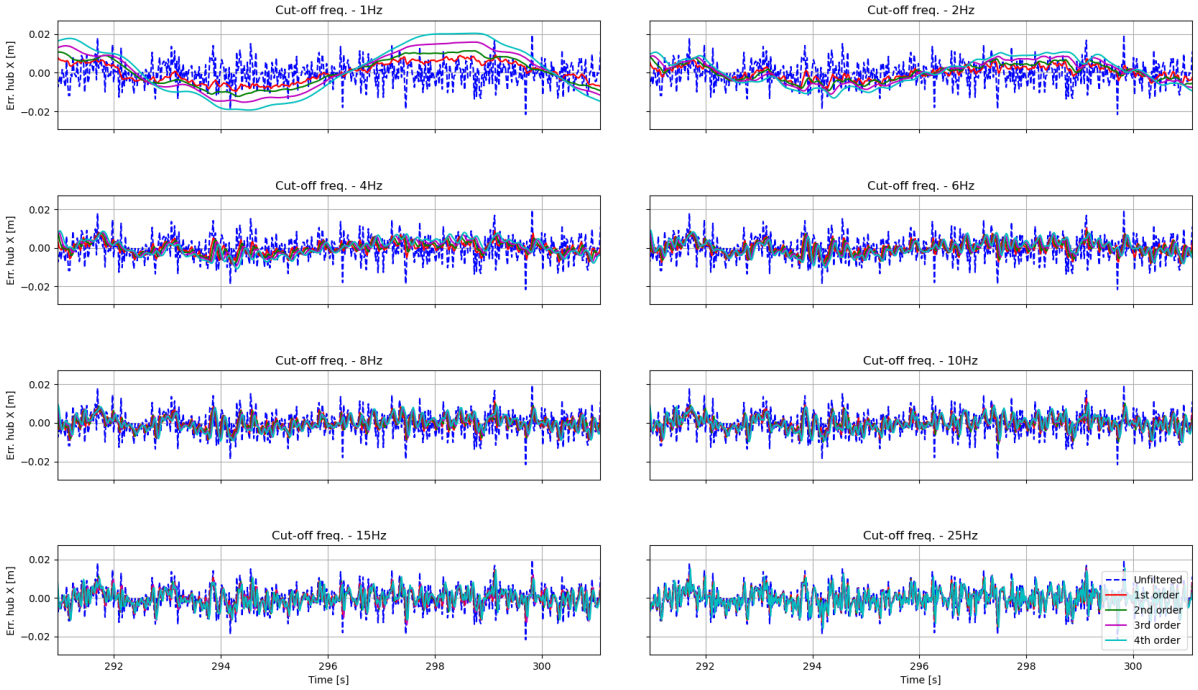


**Figure 5.7:** Sample of error between filtered and original hub motion in X direction - Load case 29.

The filter's performance is assessed for the hub's motions in all 6 degrees of freedom in terms of maximum absolute error and standard deviation of this error. As a reference, the unfiltered signal (with noise) is also processed to provide a comparison indication. Figures 5.8 and 5.9 present the maximum absolute error and the error standard deviation in all six degrees of freedom for all 32 filter designs.

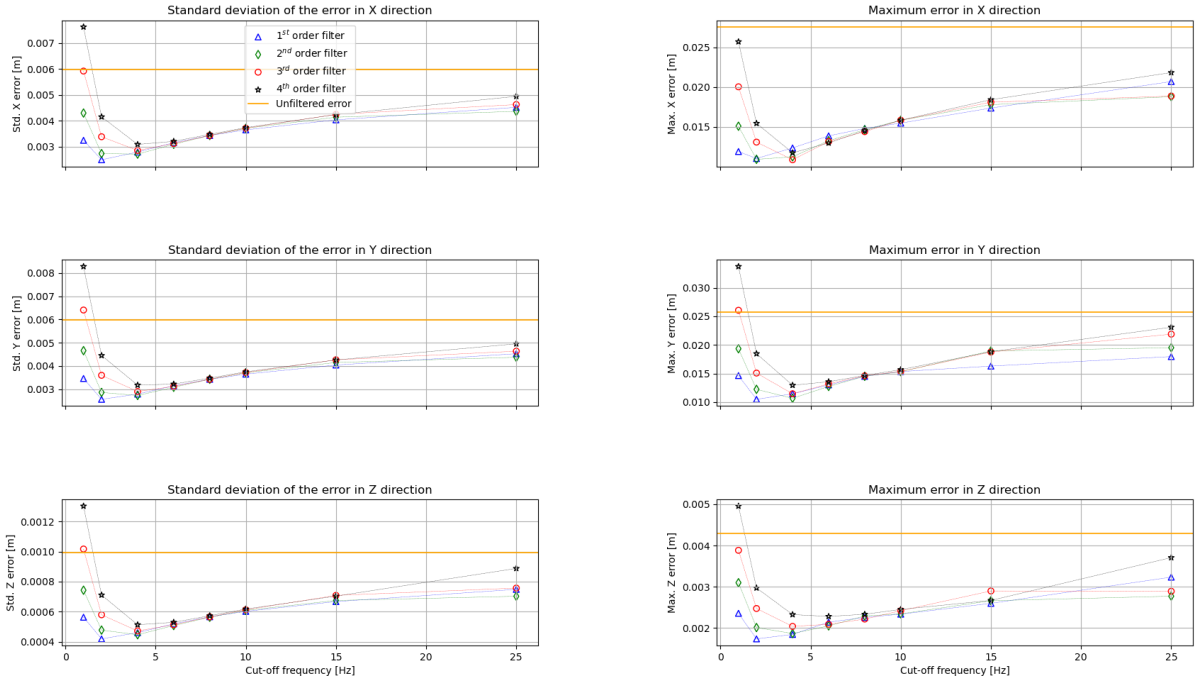


**Figure 5.8:** Maximum absolute and standard deviation of the low-pass filters - Load case 29 - X, Y and Z directions.

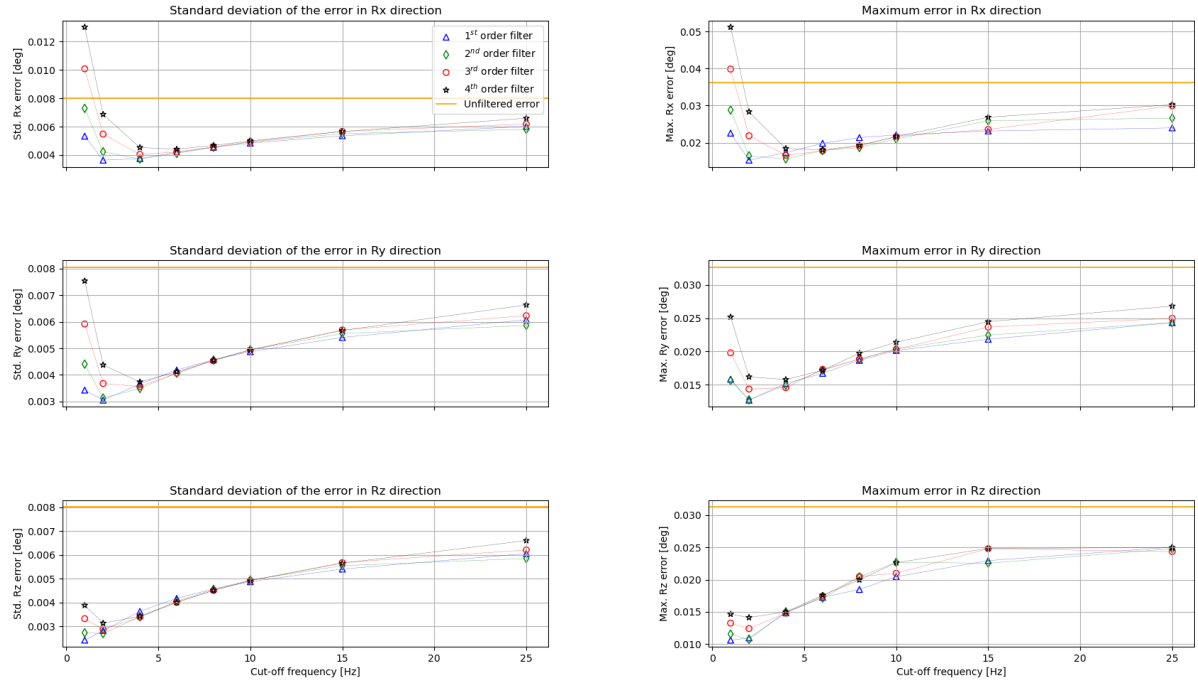


**Figure 5.9:** Maximum absolute and standard deviation of the low-pass filters - Load case 29 - Rx, Ry and Rz directions.

It can be observed that, as expected, the filter performance to reduce the maximum absolute error and the error's standard deviation is very similar. Additionally, it can be noticed that the performance of low-order filters is advantageous because they introduce a smaller phase shift on the signal, this can be confirmed by the Bode plot of the low-pass filter transfer function in Figure 5.10. Regarding the cutoff frequency, it is observed that the closer the cutoff frequency is from the frequencies in which the motions occur, the better, since no relevant frequencies are filtered out, this can be clearly observed in Figures 5.8 and 5.9 when the cutoff frequencies are set to 1Hz and 2Hz.

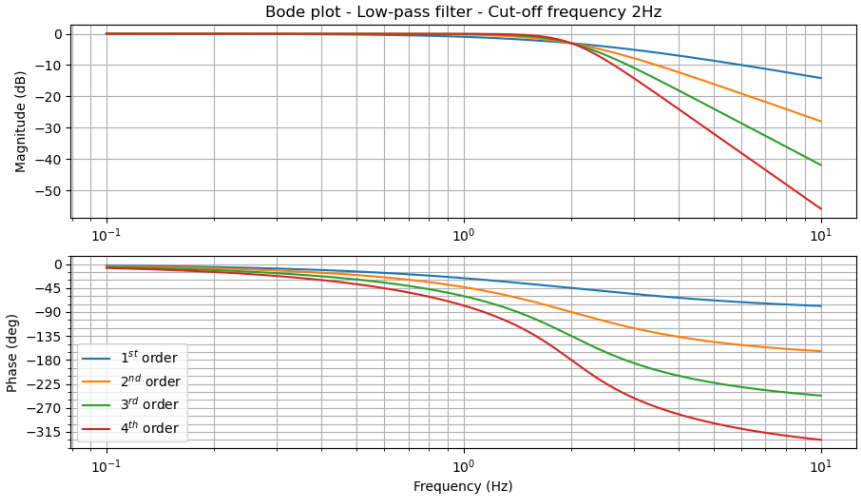


**Figure 5.10:** Bode plot of the $1^{st}$, $2^{nd}$, $3^{rd}$ and $4^{th}$ orders Butterworth low-pass filters with cut-off frequency of 2Hz.

Assessing the performance of all the filter options tested, the final Butterworth filter is of $1^{st}$ order and cut-off frequency of 2Hz.

# 6

# The motion control system

The main purpose of this thesis project is to develop and simulate a motion control system in order to reduce to a minimum the relative motions between the hub on top of the installation tower and the blade root connected to the crane's boom via the BIT and Stewart platform.

## 6.1. Motion control strategy

The motion control strategy is developed to reduce the relative motions between the hub and the root of the blade. This can be achieved by controlling the Stewart platform's position and velocity, where the BIT is connected; therefore, the main purpose of the control system is to achieve the required cylinders' lengths and velocities such that the blade root remains as motionless as possible compared to the hub. The following control plant, Figure 6.1, is designed to achieve this based on common control strategies for hydraulic cylinders.

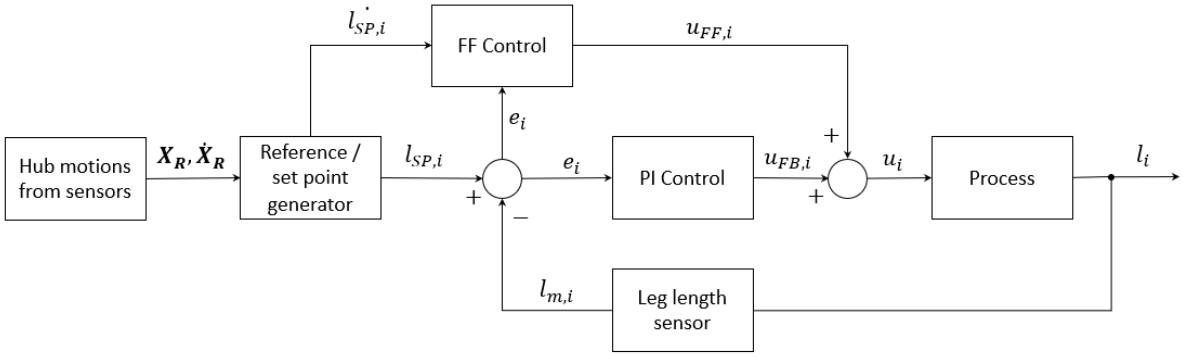


**Figure 6.1:** Stewart platform control strategy for blade installation.

In the control plant, the motions (positions and velocities) are measured in the "Motion tracking" block resulting in $\mathbf{X_R}$ and $\dot{\mathbf{X}}_{\mathbf{R}}$, these motions are used to calculate the actuators' set points, i.e. cylinders' lengths and velocities, in the "Reference / set point generator" block, respectively $l_{SP}$ and $\dot{l}_{SP}$. The actuators' velocities set points are used to calculate the feedforward control variable resulting in $u_{FF}$, while the lengths set points are used to calculate the error between the set point and the actual length; then the feedback control signal is calculated by the use of a proportional-integral (PI) controller, i.e. "PI Control" block, resulting in $u_{FB}$.

Finally, the control variable $u$ (4-way servo valve position) is used as input for the process plant that simulates the functioning of a hydraulic cylinder controlled by a 4-way servo valve. The result of the

process is the actual length of the cylinder, $l$. The cylinder is then measured by the "Leg length sensor", returning $l_m$, that is subtracted from the new cylinder length set-point ($l_{SP}$), resulting in the cylinder length error ($e$) used as input for the PI controller and to calculate the adaptive feedforward controller gain.

This control system is developed to assess the feasibility of GREPless blade installation by proposing a motion compensation system using a Stewart platform; therefore, the control strategy does not consider all aspects necessary before the system is ready for real-life application. It can be mentioned that external forces are not considered in the control plant, that is, the disturbance rejection performance of the closed-loop system is not analysed. Additionally, actuator dynamics is not taken into account in the design of the control system.

The motion control strategy is developed to control the moving element of the Stewart platform using six identical hydraulic actuators, previously specified in Chapter 3. The control plant is designed to receive the hub position, calculate where the blade root should be in order to keep a fixed and safe relative position between the parts, i.e. no relative motion. From the blade root desired position, the controllable Stewart platform position is calculated, next the desired actuators' lengths and velocities are calculated using inverse kinematics, the process input is specified, and finally the process is simulated, outputting the actuators' lengths. The control strategy is presented in Figure 6.1 and is detailed in the following sections.

The control strategy can be divided into three main parts, the reference generator, which will receive the hub motion data and calculate the required actuators' lengths and velocities to eliminate the relative motions between hub and blade root. The second being the actuator control that, from the actuators' set points will output the process variable, i.e. the servo valve position. And finally, the process part that receives the required position of the servo valve and moves it to allow the corresponding flow through the spool so that the hydraulic actuator moves to the desired position at the required velocity. The system's dynamics is not considered in the plant, therefore the hydraulic actuators length response should be able to reach the set-point after a certain amount of time. However, due to the constant changes in the cylinders' lengths set-points, the actuators' lengths errors are never zero.

### 6.1.1. Hub motions and reference generator

The motions of the hub acquired by the set-up of the sensors and instrumentation specified in Section 5.4 are used to determine the lengths and velocities of the actuators following the process in Figure 6.2.

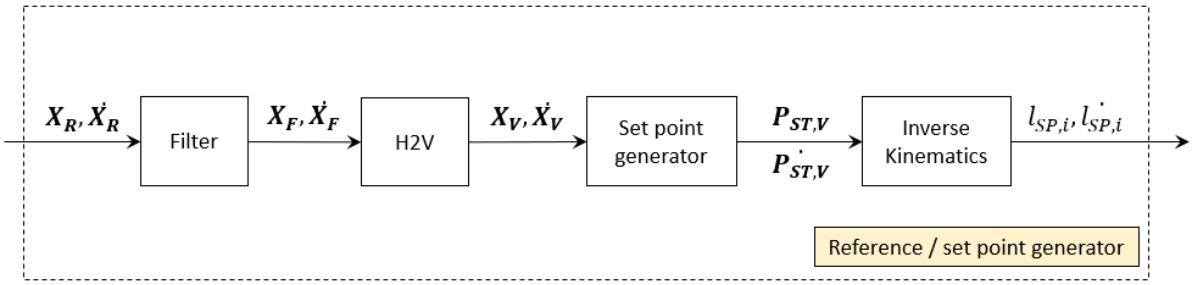


**Figure 6.2:** Motion control strategy - Reference generator.

#### Filtering

The motions of the hub in all six degrees of freedom, $\mathbf{X_R}$ and $\dot{\mathbf{X}}_\mathbf{R}$, are measured in the hub's own reference system. Here $\mathbf{X_R}$ and $\dot{\mathbf{X}}_\mathbf{R}$ are 6-by-1 arrays containing hub's position and orientation, and linear and angular velocities, respectively. Due to intrinsic noise from the sensors, they are filtered using a low-pass 1$^{st}$ order Butterworth filter with a cutoff frequency of 2Hz. The results are the variables $\mathbf{X_F}$

and $\dot{\mathbf{X}}_\mathbf{F}$.

By applying the filter as early as possible in the control strategy, the influence of nonlinear transformation, for example, on the instrumentation noise is reduced.

### Common reference system and Set point generator

Once the hub motions are filtered, they are transformed into a common reference system that will also be used by the other parts of the system. To calculate the actuator lengths and velocities, the position and orientation of both the base and the platform must be written in a common reference system. Therefore, the hub motions are transformed from its own reference system to the reference system of the vessel in the block 'H2V', receiving the variables $\mathbf{X_F}$ and $\dot{\mathbf{X}}_\mathbf{F}$ and outputting $\mathbf{X_V}$ and $\dot{\mathbf{X}}_\mathbf{V}$.

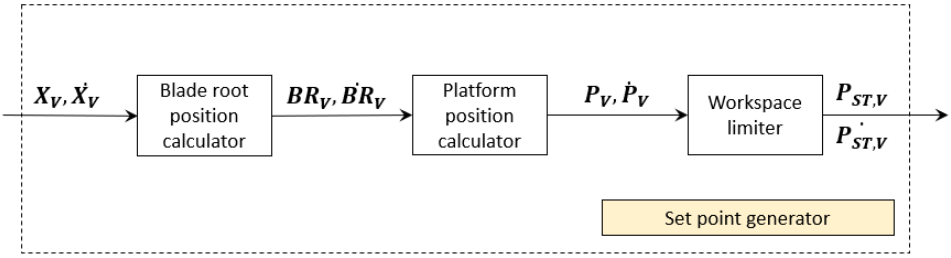


**Figure 6.3:** Motion control strategy - Set point generator.

The "Set point generator" block in Figure 6.2 is detailed in Figure 6.3. Once the hub motion is calculated in the vessel reference system, it is possible to calculate the required platform position. As the main goal is to keep the blade root motionless compared to the hub, a fixed distance between them is specified. This fixed distance is approximately 1.3m and considers the length of the blade bolts and a safety distance between the bolts and the hub of 0.5m. Hence, the required blade root position and velocity in the vessel reference system, in all six degrees of freedom, are calculated in the block "Blade root position calculator", outputting $\mathbf{BR_V}$ and $\dot{\mathbf{BR}}_\mathbf{V}$.

As confirmed in Section 2.2, the blade and BIT system can be considered a rigid system, with all relative distances and orientations known. Following the schematic presented in Figure 6.4, the required position and orientation of the platform, as well as its velocities, are calculated in the block "Platform position calculator", outputting the variables $\mathbf{P_V}$ and $\dot{\mathbf{P}}_\mathbf{V}$.

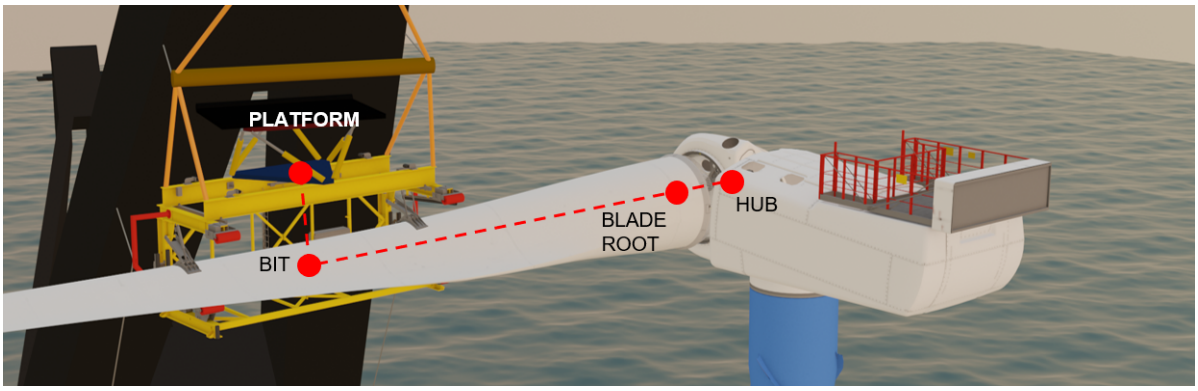


**Figure 6.4:** Representation of the relationship between hub and Stewart platform.

Finally, the variables $\mathbf{P_V}$ and $\dot{\mathbf{P}}_\mathbf{V}$ are verified against the platform workspace defined in Subsection 3.8.1. If one or more degrees of freedom of the platform is outside its workspace, the platform's

set points ($\mathbf{P_{ST,V}}$ and $\dot{\mathbf{P}}_{\mathbf{ST,V}}$) are changed to match this spatial restriction. If $\mathbf{P_V}$ and $\dot{\mathbf{P}}_{\mathbf{V}}$ are inside the workspace, $\mathbf{P_{ST,V}}$ and $\dot{\mathbf{P}}_{\mathbf{ST,V}}$ are the same as the former.

### Inverse Kinematics

The final step in the reference generator part is to calculate the actuators' set points, length, and velocity. The starting point is that the base's position and velocity are known in the vessel reference system. As the crane boom, where the base is attached, remains motionless during the final blade installation phase, its velocity is zero, and its position is known based on boom and slew angles, as well as where the base is connected on the crane's boom. From the platform's set-points ($\mathbf{P_{ST,V}}$ and $\dot{\mathbf{P}}_{\mathbf{ST,V}}$), and base's position, Equations 3.6 and 3.7 are used to calculate the actuators' lengths. The actuator velocities are calculated using Equation 3.15. From these steps, $l_{IK,i}$ and $\dot{l}_{IK,i}$ are calculated for the $i^{\text{th}}$ cylinder.

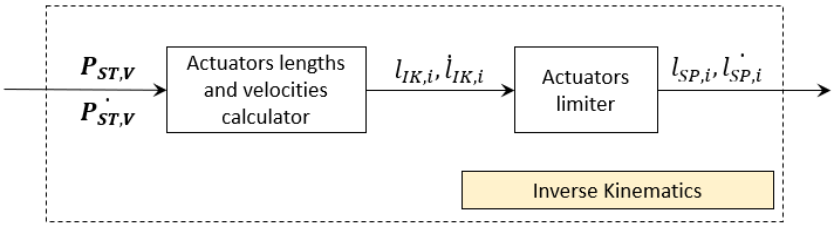


**Figure 6.5:** Motion control strategy - Set point generator.

The "Actuators limiter" block is used to ensure that the actuators' lengths and velocities do not infringe the system's limits regarding length and velocity. First, $l_{IK,i}$ is compared with the minimum and maximum length of the cylinder specified in Table 3.5, if $l_{IK,i}$ is within the maximum and minimum lengths, $l_{SP,i} = l_{IK,i}$, otherwise $l_{SP,i}$ is equal to the maximum or minimum lengths.

$$
\begin{aligned}
l_{SP,i} &= l_{min} \quad \text{if} \quad l_{IK,i} < l_{min} \\
l_{SP,i} &= l_{IK,i} \quad \text{if} \quad l_{min} \leq l_{IK,i} \leq l_{max} \\
l_{SP,i} &= l_{max} \quad \text{if} \quad l_{IK,i} > l_{max}
\end{aligned}
$$

Where $l_{min}$ and $l_{max}$ are, respectively, the minimum and maximum actuator lengths specified in Table 3.5. It is important to point out that the cylinder length verification is an added redundancy, when the platform's position and orientation is limited to its workspace in the block "Workspace limiter", the cylinders' lengths will be within their boundaries.

The next limitation to be considered is the cylinder velocity; this limitation is not only specified by the manufacture due to the mechanical system, like the seals, but also related to the maximum available flowrate from the HPU (hydraulic power unit). In a reverse approach the HPU's flowrate may be specified based on the maximum required cylinder's velocity. In the control system, the HPU's flow rate has been specified based on different criteria, with a maximum value of 450 liters per minute, therefore, the limitation for cylinder velocity is calculate as follows.

$$
\dot{l}_{lim} = \frac{Q_{max}}{A_{cyl}} \tag{6.1}
$$

Where $\dot{l}_{lim}$ is the limit velocity of the cylinder, $Q_{max}$ is the maximum flow rate of the HPU, and $A_{cyl}$ is the cross-section area of the cylinder. It is important to point out that the limiting cylinder velocity is different when the cylinder is expanding or retracting due to the different cross-section areas of the

cylinder's bore and rod sides, therefore the cylinder's velocity limits are:

$$-0.29\text{m/s} \leq \dot{l} \leq 0.20\text{m/s} \tag{6.2}$$

### 6.1.2. Actuator control

The Stewart platform's actuators, in this case hydraulic cylinders, are the most critical part of the motion control strategy. By changing their lengths and velocities, the control strategy aims to eliminate any relative motion between the blade root and the hub. The actuator control strategy presented in Figure 6.6 is divided into two parts, the first being the feedback loop and the second being the feedforward control. They are later summed to calculate the final control variable, the position of the servo-valve to move each cylinder to its desired position.

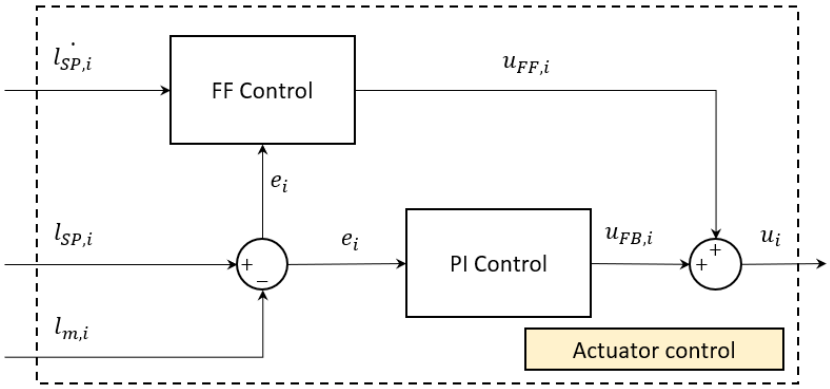


**Figure 6.6:** PI feedback and adaptive feedforward actuator control.

#### Actuator feedback control

The first part of the actuator control system is the common Proportional-Integral feedback control, acting on the positional error between the actuator length set point ($l_{SP,i}$) and the actual measured actuator length ($l_{m,i}$), resulting in the feedback control variable $u_{FB,i}$.

In a feedback-only control loop for a hydraulic cylinder, where the set point is constantly changing, it is impossible to reduce the error to zero, one may even say that an error is needed to obtain the cylinder response [49]. This is due to the fact that the cylinder velocity for a tracking control system is always non-zero, hence there is always a remaining error. In PI feedback control only, the transfer function from cylinder length error to cylinder response length is:

$$l_i = \frac{Q_{max}}{s}\left(k_P + \frac{k_P}{\tau s}\right)e_i \tag{6.3}$$

Where $s$ is the complex frequency domain parameter from the Laplace transform, $k_P$ is the proportional gain, and $\tau$ is the integral term from the integral control gain. Equation 6.3 can be rewritten as:

$$e_i = \frac{dl_i/dt}{Q_{max}\left(k_P + \frac{k_P}{\tau_i s}\right)} \tag{6.4}$$

From Equation 6.4 it can be observed that, whenever the cylinder length set-point changes in time, an error will exist. As it can be observed, the larger the gain $k_P$ and smaller $\tau$, smaller the error $e$. However, because there is a limit for these values due to instability limits, positional error always exists in pure feedback control when the system is moving [49]. To reduce this error, actuator feedforward

control is introduced.

#### Actuator feedforward control

The most common approach for feedforward control is to use a fixed gain ($k_{FF}$) multiplying the velocity set point ($u_{FF} = k_{FF} \cdot \dot{l}_{SP}$), this result is then summed to the feedback part to compose the total control variable $u$. This is a common industry practice for motion tracking, as seen in [27] and [49]. However, [50] developed an adaptive feedforward control strategy for hydraulic cylinders based on the MIT-rule [51] and the sign-sign algorithm [52] that proved to provide improved results compared to fixed feedforward gain, both in simulations and validated experimentally. The feedforward actuator control used for the Stewart platform is based on that presented in [50] and depicted in Figure 6.6.

The adaptive feedforward control law used to calculate the control variable $u_{FF,i}$ is:

$$\dot{z}_{ff} = \gamma \cdot \dot{l}_{SP} \cdot e \tag{6.5}$$

$$u_{FF} = z_{ff} \cdot \dot{l}_{SP} \tag{6.6}$$

Where $\gamma$ is the fixed parameter of the control law, $\dot{z}_{ff}$ is the time derivative of $z_{ff}$, which is the adaptive feedforward control gain, and $\dot{l}_{SP}$ is the cylinder velocity set-point. By implementing this control rule, the feedforward gain ($z_{ff}$) changes depending on the variation of the cylinder length error and velocity set-point over time, that is, larger the error, larger the gain; being reduced or increased by the cylinder velocity set-point. This provides the advantage to rapidly react to the increase in the cylinder positional error, as well as changes in the velocity set-point.

### 6.1.3. Process

Once the feedback and feedforward control variables are calculated, they are summed and used as input in the process plant. The process plant, block 'Process' from Figure 6.1, mimics the behavior of a four-way servo valve, i.e. it controls a spool that moves from -1 (fully open retracting the cylinder), passing through 0 (fully closed - no cylinder motion) to 1 (fully open expanding the cylinder).

The valve in question is modeled in a simple way, with the spool being zero lap, i.e., no overlap or underlap. Although not the most realistic choice, this allows the relationship between hydraulic flow passing from the HPU to the valve, and valve position to be modeled linearly with the following equation:

$$Q = u \cdot Q_{max} \tag{6.7}$$

$$-1 \leq u \leq 1 \tag{6.8}$$

Where $Q$ is the flow that passes through the servo-valve going to the cylinder, and $u$ is the control variable resulted from the sum of $u_{FF}$ and $u_{FB}$. From Equation 6.7 and it is important to point out that, as shown in Equation 6.8, the control variable $u$ is forced to remain between -1 and 1. Additionally, when $u < 0$ it means that the cylinder is retracting, while when $u > 0$ means that the cylinder is expanding, that is, it has negative and positive velocities. This definition becomes important because the cross-section areas (rod and cylinder sides) of the cylinder are different, but the maximum flow rate provided by the HPU does not change regardless of whether the cylinder is retracting or expanding. The cylinder's velocity can then be calculated as follows:

$$\dot{l} = \frac{Q}{A_{cyl}} = \frac{u \cdot Q_{max}}{A_{cyl}} \tag{6.9}$$

$$A_{cyl} = A_{bore} \quad \text{if} \quad u > 0 \tag{6.10}$$

$$A_{cyl} = A_{rod} \quad \text{if} \quad u < 0 \tag{6.11}$$

where $A_{bore}$ is the cross section area of the cylinder on the bore side and $A_{rod}$ the cross section on the rod side, the diameters of both the bore and the rod are specified in Table 3.5. Another important factor to consider is the time it takes for the valve to move from its fully closed ($u = 0$) position to its fully open position ($u = 1$ or $u = -1$). From different valve manufacturers catalogs, a time is chosen as 25 ms, that is, it takes 25 milliseconds for the valve to go from fully closed to fully open position, and with this value, Equation 6.10 can be solved to obtain the output cylinder length $l$ that is later measured and equal to $l_m$.

## 6.2. Motion control results

From the set-up of motion measurements specified in Section 5.4 and the motion control strategy detailed in Section 6.1, the motion compensation system for blade installation is initially simulated.

The simulations were carried out starting from load case 29, the one that presented the highest double amplitude in a degree of freedom in the $X - Y$ plane, in that case, in the $y-$ direction. Initially the actuator set points were generated considering that the measured hub motions did not present noise, the actuators' length responses were assessed, and, following, the blade root motions were calculated based on the responses. This allowed comparison of the relative blade root and hub motions for the case without motion control and with motion control. Next, noise was introduced to the hub's motions, their effect on the motion control system was assessed, with and without the low-pass Butterworth filter, in the actuators' response and the residual relative motion between blade root and hub. The position and orientation of the platform due to the response of the actuators is calculated using forward kinematics as detailed in Subsection 3.1.2.

The final performance assessment of the proposed motion control system is done by evaluating the residual relative motions between the blade root and hub with and without the motion compensation control system. The case without motion control represents that the Stewart platform is not working to compensate the relative motions generated by the hub's response on top of the installation tower, that is, the platform's actuators are kept with a constant length, and the relative residual motion is equal to the hub's motions in its own reference system.

### 6.2.1. Motion control results - without noise

The performance of the motion control system is assessed starting with the base case of no instrumentation noise, hence no filtering, for load case 29. Figure 6.7 shows a sample of actuator length control results and Table 6.1 presents the standard deviation of the error and the maximum absolute error between the length set point and the length response per cylinder.

**Table 6.1:** Maximum absolute error and error standard deviation per actuator - No noise - Load case 29.

| Actuator | #1 | #2 | #3 | #4 | #5 | #6 |
|---|---|---|---|---|---|---|
| Error std. [mm] | 1.9 | 8.5 | 3.1 | 1.5 | 8.4 | 3.3 |
| Max. abs. error [mm] | 6.0 | 28.4 | 9.1 | 5.2 | 28.7 | 10.1 |

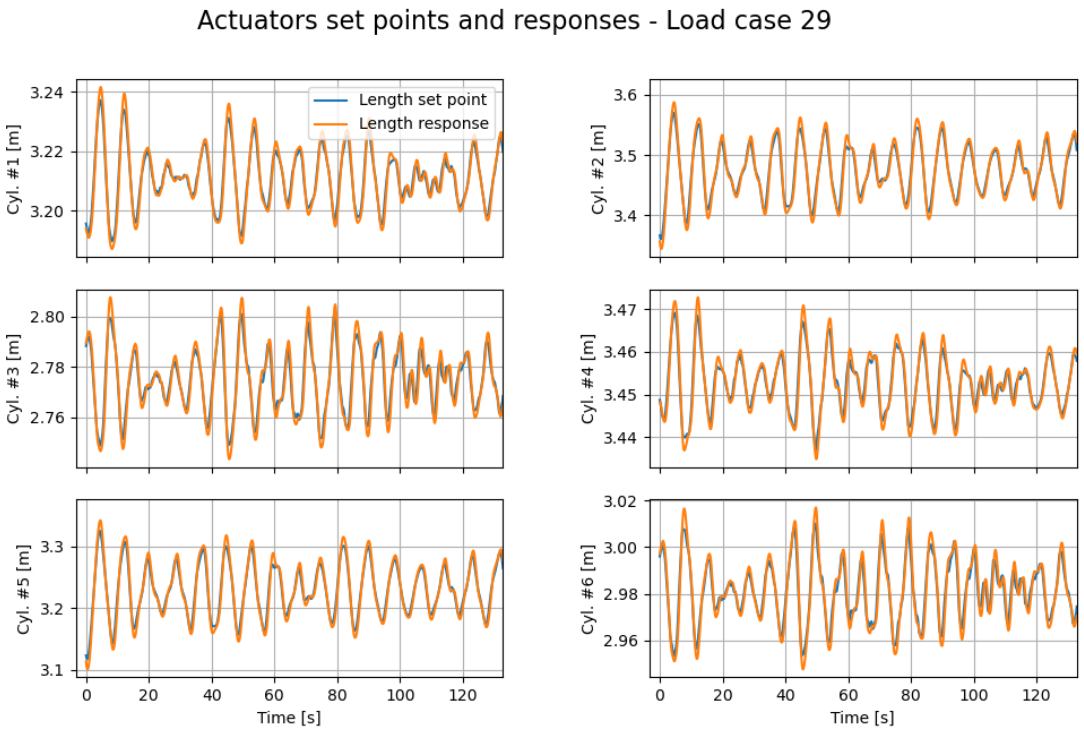


**Figure 6.7:** Actuators' set points and responses without noise - Load case 29.

Although the actuators' figures, comparison between set points and actual response, provide a reasonable indication of the motion control system's performance, the final indication must be the residual relative motion between blade root and hub. Therefore, with the cylinders' responses the platform's position and orientation is calculated using forward kinematics, and then the blade root's position and orientation are also calculated. This makes it possible to calculate the residual motion between the blade root and the hub.

**Table 6.2:** Maximum absolute error and error standard deviation per degree of freedom with and without the proposed motion control system - No noise - Load case 29.

| | Degree of freedom | X [mm] | Y [mm] | Z [mm] | Rx [°] | Ry [°] | Rz [°] |
|---|---|---|---|---|---|---|---|
| W/o motion control | Error std. | 26.4 | 22.8 | 11.8 | 0.02 | 0.04 | 0.01 |
| | Max. abs. error | 81.9 | 64.9 | 40.7 | 0.06 | 0.13 | 0.03 |
| With proposed control | Error std. | 5.9 | 4.8 | 3.5 | 0.01 | 0.01 | 0.00 |
| | Max. abs. error | 22.0 | 12.9 | 13.3 | 0.02 | 0.03 | 0.01 |

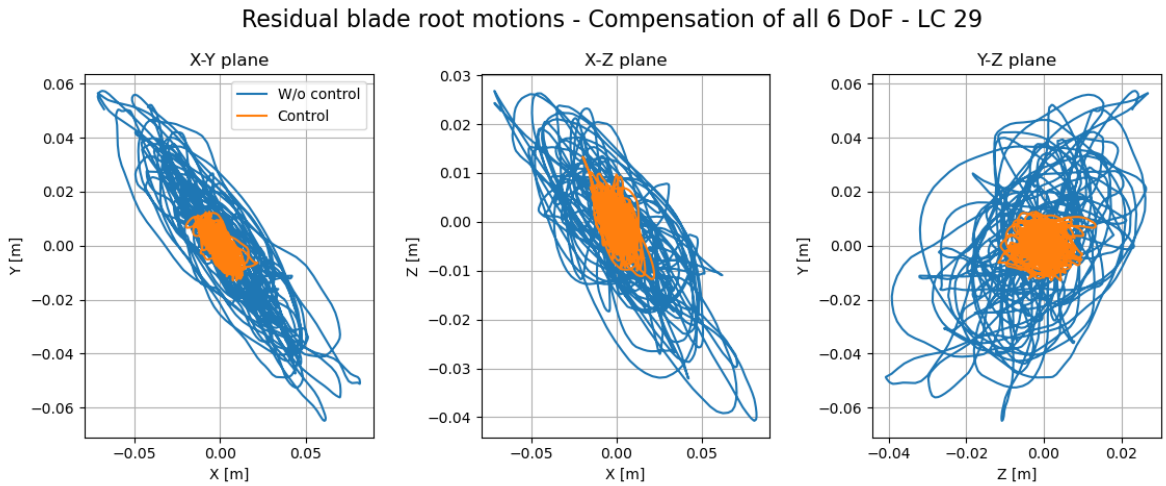


**Figure 6.8:** Blade root residual motion without motion control (blue) and with the proposed control system (orange) - No instrumentation noise - Load case 29.

From Figure 6.8 and Table 6.2 it is possible to confirm that the proposed control system significantly reduces relative motions between the blade root and the hub, making the installation process considerably easier even with a significant wave height of 2.5 meters from the beam and wind speeds averaging 14 m/s from the stern. Nevertheless, the influence of the sensors' noise is not yet evaluated.

### 6.2.2. Motion control results - with noise

Even if the results presented in Subsection 6.2.1 provide a good indication of the proposed motion control performance to reduce the relative motions between blade root and hub, the figures do not consider the influence of the instrumentation accuracy while measuring the hub motions. In this section, the proposed control system is simulated including the unfiltered instrumentation noise and its influence on the actuators' responses and blade root residual motions, as well as the improvement when this noise is filtered using a simple low-pass Butterworth filter.

The motion control results for the actuators' lengths considering the instrumentation noise, unfiltered and filtered, are presented below in Figure 6.9 and Table 6.3.

**Table 6.3:** Maximum absolute error and error standard deviation per actuator without noise, with unfiltered noise and with filtered noise - Load case 29.

| | Actuator | #1 | #2 | #3 | #4 | #5 | #6 |
|---|---|---|---|---|---|---|---|
| No noise | Error std. [mm] | 1.9 | 8.5 | 3.1 | 1.5 | 8.4 | 3.3 |
| | Max. abs. error [mm] | 6.0 | 28.4 | 9.1 | 5.2 | 28.7 | 10.1 |
| Filtered noise | Error std. [mm] | 2.3 | 8.6 | 3.4 | 2.0 | 8.5 | 3.6 |
| | Max. abs. error [mm] | 7.6 | 30.8 | 11.3 | 7.9 | 29.7 | 11.3 |
| Unfiltered noise | Error std. [mm] | 2.6 | 10.3 | 3.9 | 2.2 | 10.3 | 4.2 |
| | Max. abs. error [mm] | 8.1 | 32.3 | 13.3 | 7.6 | 34.0 | 13.5 |

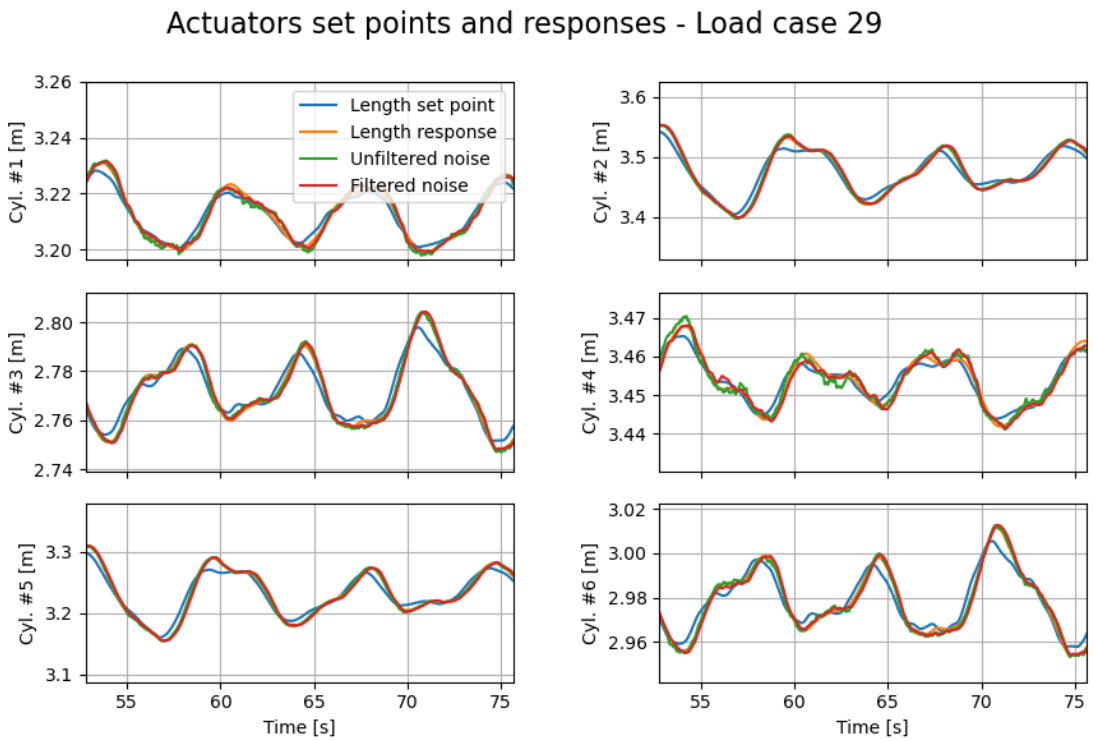


**Figure 6.9:** Actuators' set points (blue) and responses without noise (orange), unfiltered (green) and filtered noise (red) - Load case 29.

From the actuators' responses with filtered and unfiltered sensors' noise, the corresponding platform's, and later blade root's position and orientation are calculated. The residual motion between the root of the blade and the hub is calculated with the filtered and unfiltered instrumentation noise.

**Table 6.4:** Maximum absolute error and error standard deviation per degree of freedom without motion control, with the proposed motion control without instrumentation noise, with unfiltered noise and with filtered noise - Load case 29.

| | Degree of freedom | X [mm] | Y [mm] | Z [mm] | Rx [°] | Ry [°] | Rz [°] |
|---|---|---|---|---|---|---|---|
| W/o motion control | Error std. | 26.4 | 22.8 | 11.8 | 0.02 | 0.04 | 0.01 |
| | Max. abs. error | 81.9 | 64.9 | 40.7 | 0.06 | 0.13 | 0.03 |
| W/o noise | Error std. | 5.9 | 4.8 | 3.5 | 0.01 | 0.01 | 0.00 |
| | Max. abs. error | 22.0 | 12.9 | 13.3 | 0.02 | 0.03 | 0.01 |
| With unfiltered noise | Error std. | 7.5 | 5.6 | 6.5 | 0.02 | 0.01 | 0.01 |
| | Max. abs. error | 32.9 | 20.1 | 28.0 | 0.07 | 0.06 | 0.04 |
| With filtered noise | Error std. | 7.4 | 6.3 | 5.5 | 0.01 | 0.01 | 0.01 |
| | Max. abs. error | 22.9 | 19.5 | 19.1 | 0.05 | 0.05 | 0.03 |

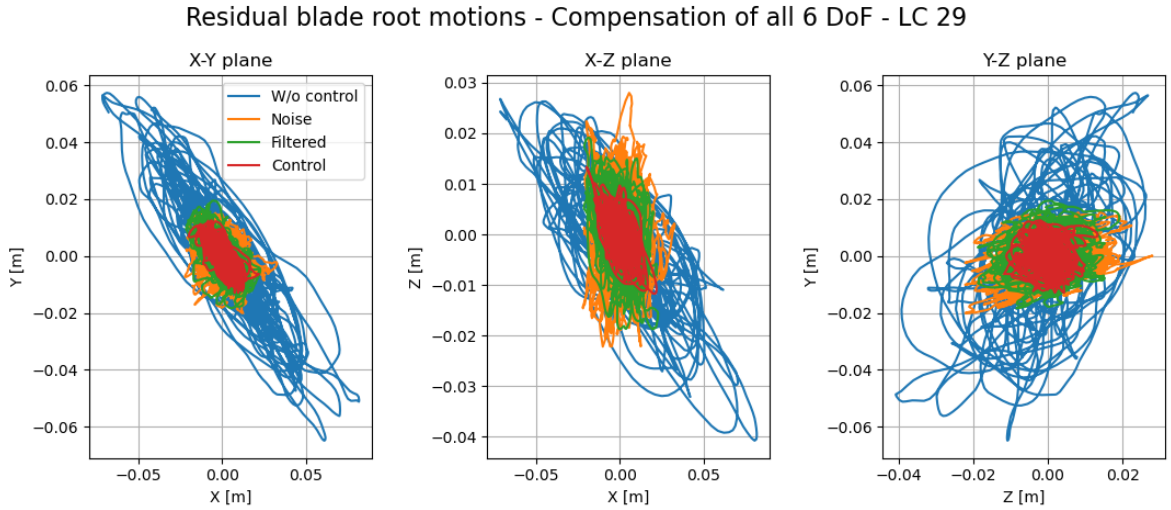


**Figure 6.10:** Blade root residual motion without motion control (blue), with the proposed motion control system without instrumentation noise (red), with unfiltered instrumentation noise (orange), and filtered noise (green) - Load case 29.

From the results depicted in Figure 6.10 and Table 6.4 it is possible to observe the clear benefit of implementing a motion compensation control system to reduce the relative motions between the hub and the blade root in the blade installation operation. Without motion control, the hub response due to the vessel's motions and wind loads make the blade installation operation not possible, even considering that the blade is attached to the crane boom and not hanging from the crane's hoist wire. This method enables the blade - hub mating operation even in reasonably rough metocean conditions.

When the instrumentation noise is introduced, it is possible to notice that even when the sensor signal is not filtered, the motion control system is able to significantly reduce the relative motions between hub and blade root, this is related to the selection of the instrumentation used to measure the hub's motions, their accuracy affects the performance of the motion control system, but even when unfiltered, the relative motions in the $X-Y$ plane are still reasonably compensated for. When the filter is introduced, the relative motions are reasonably improved when compared to the unfiltered hub signal, but still fall short of the case without instrumentation noise.

## 6.3. Motion control results compensating for the motions in $x-$, $y-$ and $z-$ directions

By using real performance parameters from sensors to measure the hub motions and generate the actuator's set points for the Stewart platform, it affects the platform's residual motions and therefore the relative motions between hub and blade root, even if slightly. analyzing the hub motions from the 30 OrcaFlex simulations, it is observed that the amplitudes of the hub's rotations are particularly small, to a degree that they do not influence the blade - hub connection operation.

When considering the small amplitude of the hub rotations and the influence that the accuracy of the sensors measuring the rotations may have over the other degrees of freedom, it is reasonable to evaluate the overall motion compensation capabilities of the system when the actuators set points are generated with the intention of compensating for the relative motions only in the $x-$, $y-$ and $z-$ directions, that is, the translations. The Stewart platform's residual motion about the $x-$ axis, caused by a sensor noise, may have a reasonable influence over the blade root motion in the $z-$ direction, for example.

The performance of the motion control system is then assessed to compensate for the hub motions only in the $x-$, $y-$ and $z-$ directions. That is, only the hub's translations are measured, while the rota-

tions remain unchanged over time in its static configuration, i.e. not susceptible to sensor noise. In this scenario, the control system is simulated for the case without sensor noise, with unfiltered sensor noise, and filtered sensor noise. One again load case 29 is simulated in order to provide a good comparison to the case where all six DoF are compensated for.

**Table 6.5:** Maximum absolute error and error standard deviation per actuator without noise, with unfiltered noise and with filtered noise. Actuators set points generated for motion compensation of $x-$, $y-$ and $z-$ directions - Load case 29.

| | Actuator | #1 | #2 | #3 | #4 | #5 | #6 |
|---|---|---|---|---|---|---|---|
| No noise | Error std. [mm] | 2.2 | 5.3 | 3.8 | 2.4 | 4.9 | 4.1 |
| | Max. abs. error [mm] | 9.2 | 17.5 | 9.8 | 10.1 | 16.4 | 10.6 |
| Filtered noise | Error std. [mm] | 2.4 | 5.4 | 3.9 | 2.7 | 5.0 | 4.2 |
| | Max. abs. error [mm] | 11.3 | 18.2 | 11.0 | 12.5 | 18.9 | 13.4 |
| Unfiltered noise | Error std. [mm] | 2.8 | 6.4 | 4.6 | 3.0 | 6.0 | 5.0 |
| | Max. abs. error [mm] | 11.4 | 19.7 | 12.6 | 12.2 | 18.4 | 13.6 |

The actuator results are presented in Table 6.5. The numerical values may lead to the conclusion that there was an performance improvement; however, the set points differ from the ones used in the motion compensation of all six DoF, therefore, evaluating this alternative's performance based on the actuator's errors does not provide an appropriate indication. This assessment must be done by evaluating the residual motions between the blade root and the hub.

Figure 6.11 shows the residual relative motions between the blade root and the hub when the motion control system works only to compensate for the motions of the hub in the $x-$, $y-$ and $z-$ directions. It is observed that the residual motions in all degrees of freedom increase, a smaller increase in the $x-$ and $y-$ directions, but a large loss of performance with respect to the residual motions in the $z-$ direction. The increase in the relative motions in the $z-$ direction is directly related to the Stewart platform not compensating for the hub's rotation about the local $x-$ axis. By not following the hub's rotation about the $x-$ axis, the Stewart platform presents a "residual" angular motion in that direction, when compared to the case where all six DoF are compensated. This residual angular motion on the platform creates a larger translational motion in the $z-$ direction on the blade root. In conclusion, not using the hub's rotations as inputs to generate the actuators' set points will lead to an amplification of the residual translational motions between blade root and hub. The numerical values of the relative residual motions between the blade root and the hub corroborating these arguments are presented in Table 6.6.

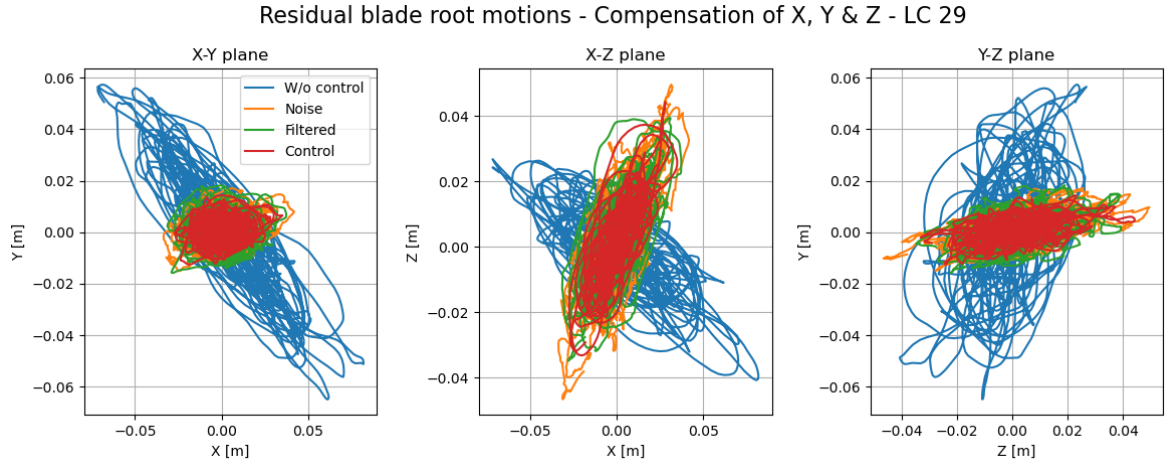


**Figure 6.11:** Blade root residual motion without motion control (blue), with the proposed motion control system without instrumentation noise (red), with unfiltered instrumentation noise (orange), and filtered noise (green) when compensating for the hub motions in the $x-$, $y-$ and $z-$ directions - Load case 29.

Similarly, occurs when relating the platform's residual rotation about the $z-$ in the blade root residual motion in the $x-$ direction. These figures are explained by a few factors. The first one is that the Stewart platform is a parallel mechanism, that is, even if the goal is to move it in one direction only, all six actuators must move, therefore the motion compensation of a single degree of freedom can not be isolated to a single set of actuators. The second factor is the distance between the controllable platform and the blade root, approximately 20 meters, and a small rotation on the platform will greatly influence the blade root motions. Finally, because the sensors specified to measure the hub's rotations, those are the MRU and the gyroscope, have only a small error and provide readings with great accuracy and sampling frequency.

**Table 6.6:** Maximum absolute error and error standard deviation per degree of freedom without motion control, with the proposed motion control without instrumentation noise, with unfiltered noise and with filtered noise. Actuators set points generated for motion compensation of $x-$, $y-$ and $z-$ directions - Load case 29.

| | Degree of freedom | X [mm] | Y [mm] | Z [mm] | Rx [°] | Ry [°] | Rz [°] |
|---|---|---|---|---|---|---|---|
| W/o motion control | Error std. | 26.4 | 22.8 | 11.8 | 0.02 | 0.04 | 0.01 |
| | Max. abs. error | 81.9 | 64.9 | 40.7 | 0.06 | 0.13 | 0.03 |
| W/o noise | Error std. | 10.3 | 4.6 | 11.6 | 0.02 | 0.04 | 0.01 |
| | Max. abs. error | 35.0 | 14.3 | 44.3 | 0.06 | 0.13 | 0.04 |
| With unfiltered noise | Error std. | 10.9 | 5.0 | 12.2 | 0.03 | 0.04 | 0.01 |
| | Max. abs. error | 41.8 | 17.1 | 49.6 | 0.08 | 0.14 | 0.07 |
| With filtered noise | Error std. | 11.1 | 5.8 | 11.6 | 0.02 | 0.04 | 0.01 |
| | Max. abs. error | 37.4 | 18.2 | 39.4 | 0.08 | 0.14 | 0.04 |

In conclusion, due to the operation and equipment set-up, it is important that all six degrees of freedom from the hub are used as inputs in the control system, even if this implies in the mobilization of more sensors and having to filter their signals. Without compensating for all six DoF, the residual motions between the blade root and the hub are such that the blade - hub mating operation may be restricted to very calm metocean conditions when the hub motions are smaller.

# 7

# Conclusion and recommendations

In this work, a new method is proposed for wind turbine installation using a floating vessel. This method makes use of the already developed concept of preassembly of the RNA on a temporary support structure on the WTIV's deck (installation tower). Starting from this point, a motion-compensated Stewart platform is implemented connecting the crane boom to the blade installation tool (BIT) to guide the blade to the hub while compensating for the relative motions between the blade root connected to the Stewart platform and the WTG's hub on the installation tower.

## 7.1. Conclusion

The purpose of this thesis project was to develop a blade installation method in complement to HMC's RNA method that does not require the GREP tool. This was achieved by implementing a motion compensated Stewart platform connecting the BIT to the crane boom. The process is structured by answering the main research questions, and the two sub-questions.

The technical feasibility of using a motion-compensated Stewart platform for blade installation is initiated by quantifying the motions to be compensated for, that is, source, amplitude and frequencies. This is done by running implicit time domain simulations in OrcaFlex for fixed significant wave height and peak period, but varying the incident direction. The wind fields used were generated in TurbSim with mean wind speeds of 12 m/s and 14 m/s, and varying the incident angle. Additionally, the hub motions on top of the installation tower are obtained from the OrcaFlex simulations in the three possible configurations prior to a blade installation, that is, no blades connected to the hub, one blade connected to the hub, and two blades connected to the hub. As the motions to be compensated for are the relative motions between blade root and hub, the influence blade root motions are studied by assessing the crane boom's stiffness and the blade deflection in the length between the BIT and the blade root. A study of the crane boom horizontal stiffness is carried on and verified that it is approximately 12 times more stiff than the installation tower. Furthermore, the blade deflection under its own weight is calculated to be less than 0.5 mm. These studies conclude that the only relevant source of relative motions between hub and blade root originate due to the installation towers response.

The project proceeds by setting design constraints to the Stewart platform, i.e. its main dimensions, and providing its kinematic formulation. This allows the calculation of the Stewart platform actuator's parameters to perfectly compensate the motions between hub and blade root, that is, calculating the required stroke and speeds of the six actuators for 30 different load cases and hub's responses. Next, the dynamic behaviour of the Stewart platform is formulated to allow the calculation of loads imposed to the actuators while moving the Stewart platform to perfectly compensate for the motions between hub and blade root. In this part of the study, inertia and external forces are considered, for the latter, the aerodynamic loads are calculated for a wind speed of 16 m/s and different combinations of angle of attack and wind incidence angle. Next, a sensitivity analysis is carried on varying the static vertical

distance between base and platform to assess how it changes the required stroke, minimum, and maximum length of the actuators, as well as their required speeds, and loads imposed to them. Finally the actuators are selected based on commercially available products.

The reach of the Stewart platform is calculated by analysing its workspace, and next the mechanism dexterity is calculated in all workspace to evaluate possible singularity points and positions where the actuators could be subjected to unnecessary high loads. Next, the actuators' HPU's are selected based on the required rated pressure and flow rate, two criteria are used, the first one is that both flowrate and rated pressure are according to the requirements, and the second one is a small enough HPU that can still be mounted on the cylinder.

The feasibility study of using a Stewart platform for blade installation proceeds by developing an operational procedure, proving that the task can be executed without introducing much complexity. Furthermore, concepts are developed for the main mechanical systems of the Stewart platform.

The project proceeds with the assessment of different combination of sensors to measure the motions to be compensated for. Different techniques and products are evaluated according to their performance parameters such as accuracy and sampling frequency. An optimal set-up of sensors is specified to measure the hub's motions. Furthermore, a low-pass Butherworth filter is designed to reduce the instrumentation noise, and therefore its influence on the motion compensation control system.

Finally, a motion compensation control strategy for the Stewart platform is developed and simulated using a feedback PI controller together with an adaptive feedforward controller for the actuators. Upon simulating the control system, it was observed that the relative motions between the blade root and the hub are drastically reduced.

The steps used in the thesis project answer the main research question and conclude that it is technically feasible to use a motion compensated Stewart platform attached to the crane boom for blade installation by a floating vessel with the nacelle on top of a temporary structure, i.e. the installation tower, on the vessel's deck.

Although the relative motions between the blade root and the hub are significantly reduced, they are not kept within $\pm$2mm, which is the tolerance between the hub and the blade when no primary alignment system is used. This is obtained initially by removing the pendular motions of the blade by attaching it to the crane boom, and then by implementing the motion compensation control system. It is clear that in the offshore environment with corresponding metocean conditions, as well as the sizes and masses of the equipment involved, this tolerance is virtually impossible to be reached at all moments. Therefore, the motion compensation control system does not need to eliminate all and every relative motion between the blade root and the hub, the system must only reduce it to a value where a primary alignment system can be used, such as the shark fins depicted in Figure 7.1.

Another benefit of the proposed solution is that tugger winches are not used in a critical applications; therefore, failures possible to occur with tuggers have reduced consequences. Common failures of tuggers include breaking of wire ropes, brake failure, system overload, control system malfunction, amongst others.

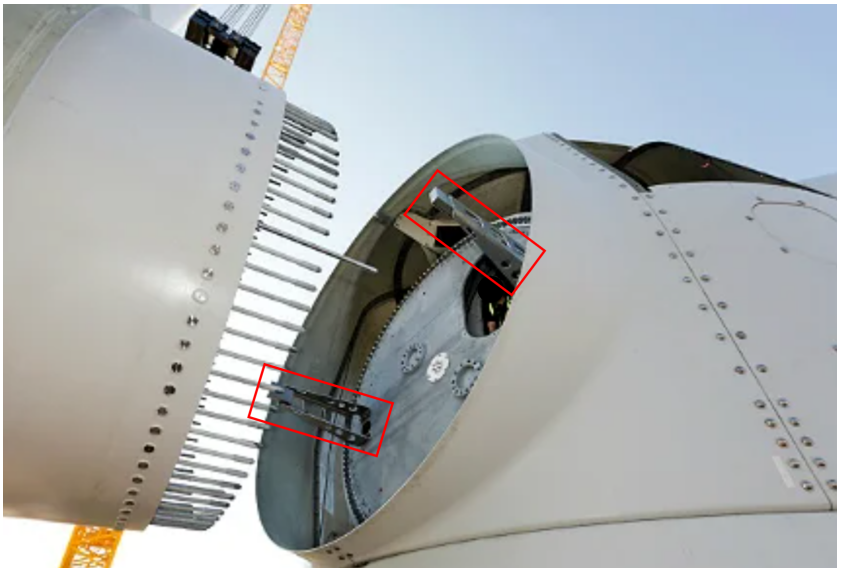

**Figure 7.1:** Blade - hub alignment accessory. Shark fins squared in red [53].

## 7.2. Recommendations

This project provides a robust initial development of a motion compensated Stewart platform connecting the crane's boom to the blade installation tool to be used for blade installation, until this moment similar methodology for blade installation has not been developed. It encompasses preliminary studies, development of an operational procedure, as well as conceptual design of mechanical systems, development of motion control systems and assess the performances of the different parts. However, further development is still required, both technical and general and / or economical.

### 7.2.1. Technical recommendations

The technical recommendations start by highlighting that this project was developed based on a specific model of wind turbine, the Vestas V174-9.5MW wind turbine, therefore some parameters may change when varying the wind turbine model. Namely, a nacelle with different characteristics may result in different hub motions, which will result in different actuator behavior. Additionally, if the blade length is increased, more specifically the distance between the blade root and the blade's center of gravity, this will result in a different crane's boom configuration, and as consequence a different yaw angle between the fixed base and controllable Stewart platform. This variation has to be evaluated to verify if the current selected actuators will have enough available stroke, as well as if it will not infringe on their minimum and / or maximum length.

An unwanted and uncontrolled accidental impact between blade root and hub during the stabbing phase may damage the WTG's components, thus a protection system must be implemented. Due to the complexity of the loads acting on the actuators of the Stewart platform, and how they can be influenced simply by a wind gust or a higher acceleration response of the vessel, it is recommended that an overload protection system be implemented in the sliding mechanism cylinders. A frontal impact of the root of the blade on the hub will generate a peak pressure on these cylinders, which is easier to identify and solve. A possible solution is to implement a pressure relief valve to avoid peak pressures, and as a consequence reduce this possible impact force.

The dynamics of the systems are not considered in the control system. The external forces acting on the system that are transmitted to the Stewart platform's actuators are not simulated in the control system. Therefore, their influence on the control system's performance is not assessed; this can play an important role in the system's overall performance. Additionally, the only part of the hydraulic system modeled is the 4-way servo valve, the other parts shall also be modeled and included in the

control system, the hydraulic system parameters such as piping lengths, stiffness, fluid characteristics, and other factors. A P (proportional) feedback controller that includes the dynamics of a mass loaded hydraulic cylinder is presented in Figure 7.2 and can be used as a reference.

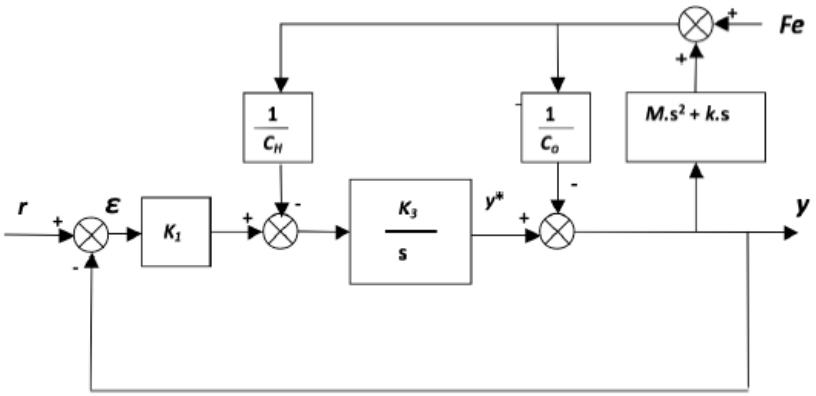


**Figure 7.2:** Basic block diagram of a feedback P controller of a mass loaded hydraulic cylinder [49].

Alternatives to improve the performance of the motion control system by dealing with the delay and anticipating the hub motions may be implemented. These alternatives are model based and can be achieved by, mainly by implementing model predictive control or feedforward control with the current baseline controller. For this purpose the installation tower equations of motion are developed and presented in Appendix A.

### 7.2.2. General and economical recommendation

The technical challenges for the application of the proposed solution, as well as the technical recommendations before its implementation, are well known and defined. Nevertheless, the overall performance of the system must be evaluated in terms of vessel hours, i.e., how much time does the proposed solution might take to install the blades, is it faster or slower than the already existing RNA method? Additionally, is the initial investment on the motion compensated Stewart platform worth it in terms of vessel hours, even when considering the GREP tool as a one project specific equipment? Not only should an economical assessment be done, but also an evaluation of ways to improve the installation times of the proposed system as familiarity with the method reduces the task duration.

The proposed solution, however, may be more complex than required. The system without motion compensation will result in relative motions between blade root and hub to be the same as the hub motions. Therefore, if these motions can be accepted by the primary alignment system, such as shark fins, an active motion compensation system may not be necessary, and a passive system to avoid the transmission of high loads to the blade and BIT due to bumper loads in the stabbing phase. This approach is equivalent to a passive heave compensator acting to keep the crane load constant during lifting operations acting on the variation of added mass and external forces on the payload. Alternatively, if the primary alignment system can not directly accommodate the relative motions between hub and blade root, a tuned mass damper device can be mobilized on the installation tower to reduce the amplitude of its motions. The concept and effectiveness of this device is detailed in [54] and [55].

# References


1. Europe, W. *Offshore Wind in Europe. Key trends and statistics 2020* (2021).
2. Europe, W. *Offshore wind energy 2021 statistics* (2022).
3. Europe, W. *Wind energy in Europe - 2022 statistics and the outlook for 2023-2027.* (2023).
4. Europe, W. *Offshore wind energy 2022 statistics* (2023).
5. Mikkel Gleerup, C. o. C. *Rocking the boat: The role of vessels in driving offshore wind growth* https://gwec.buzzsprout.com/1229717/6911426-rocking-the-boat-the-role-of-vessels-in-driving-offshore-wind-growth. GWEC - Global Wind Energy Council, Dec. 2020.
6. AS, C. *Windfarm Installation Vessel (WIV) Wind Osprey* (2022).
7. Windcarrier, F. O. *Windfarm Installation Vessel (WIV) Blue Tern* (2022). www.windcarrier.com.
8. Oelker, S., Sander, A., Kreutz, M., Ait-Alla, A. & Freitag, M. Evaluation of the impact of weather-related limitations on the installation of offshore wind turbine towers. *Energies* **14.** ISSN: 19961073 (13 July 2021).
9. *Hywind | Saipem* https://www.saipem.com/en/projects/hywind. Accessed: 2023-07-20.
10. *Wind Turbine Installation Vessel - Huisman Equipment* https://www.huismanequipment.com/en/products/renewables/offshore_wind/windfarm-installation-vessel. Accessed: 2023-07-20.
11. *offshoreWIND.biz Thialf Installs First V174-9.5 MW Turbine at Arcadis Ost 1 Using Floating Installation Method* https://www.offshorewind.biz/2022/11/25/thialf-installs-first-v174-9-5-mw-turbine-at-arcadis-ost-1-using-floating-installation-method/. Accessed: 2022-12-15.
12. *LT870 - Blade Yoke | Liftra* https://liftra.com/products/lt870-blade-yoke. Accessed: 2023-07-13.
13. Stewart, D. A Platform with Six Degrees of Freedom. *Proceedings of the Institution of Mechanical Engineers* **180,** 371–386. eprint: https://doi.org/10.1243/PIME_PROC_1965_180_029_02. https://doi.org/10.1243/PIME_PROC_1965_180_029_02 (1965).
14. Meskers, G. *A DAMPING TUGGER SYSTEM FOR OFFSHORE HEAVY LIFTS* in (ASME 2012 31st International Conference on Ocean, Offshore and Arctic Engineering, 2012). http://www.asme.org/about-asme/terms-of-use.
15. Ren, Z., Verma, A. S., Ataei, B., Halse, K. H. & Hildre, H. P. Model-free anti-swing control of complex-shaped payload with offshore floating cranes and a large number of lift wires. *Ocean Engineering* **228.** ISSN: 00298018 (May 2021).
16. Bron, M. T. *Model-free Positioning Control of a Payload by use of Wires Thesis report* (2022).
17. Jiang, Z. Installation of offshore wind turbines: A technical review. *Renewable and Sustainable Energy Reviews* **139.** ISSN: 18790690 (Apr. 2021).
18. Contractors, H. M. *RNA flight Path with Thialf PS Crane - CP0532.00000 HI-156-15-01 Rev. C* 2022.
19. DHI. *Arcadis Ost 1 Offshore Wind Farm, Germany. Metocean Study for Detailed Design* tech. rep. 11822849 Rev. 2.2 (Oct. 2019).
20. Equinor. *Dogger Bank C Metocean Design Basis* tech. rep. C264-EQ-Z-SP-00001 Rev. 01 (Jan. 2021).
21. Equinor. *Lease Area OCS-A 0512, Metocean Design Basis* tech. rep. C218-ST-Z-SP-00001 Rev. 04 (Jan. 2021).

22. Equinor. *Lease Area OCS-A-0520, Metocean Design Basis* tech. rep. C251-EQ-Z-FD-00001 Rev. 01 (Feb. 2022).
23. SE, H. M. C. N. *Crane Stiffness* tech. rep. MAE-HM03-MEM-003 Rev. 2 (May 2021).
24. Lee, T.-Y. & Shim, J.-K. Forward kinematics of the general 6–6 Stewart platform using algebraic elimination. *Mechanism and Machine Theory* **36,** 1073–1085. ISSN: 0094-114X. https://www.sciencedirect.com/science/article/pii/S0094114X01000349 (2001).
25. Jakobovic, D. Forward Kinematics of a Stewart Platform Mechanism (May 2002).
26. Lie, K. W. L. *Inverse Dynamics Control for the Ampelmann System* (TU Delft, Jan. 2017). http://resolver.tudelft.nl/uuid:4f7d57fa-0579-4d76-a7cf-669903cedd97.
27. Salzmann, D. J. C. *Ampelmann : development of the access system for offshore wind turbines.* (TU Delft, Oct. 2010). ISBN: 9789088911941. http://resolver.tudelft.nl/uuid:28576ef7-dee4-4ab4-a824-36f7b94ab21f.
28. Fichter, E. A Stewart Platform- Based Manipulator: General Theory and Practical Construction. *The International Journal of Robotics Research* **5,** 157–182. eprint: https://doi.org/10.1177/027836498600500216. https://doi.org/10.1177/027836498600500216 (1986).
29. Offshore, M. V. *Blade 85m* tech. rep. 300041245 Rev.03 (May 2021).
30. Offshore, M. V. *Blade Installation Tool - V164-V174 - 8.0 - 10MW WTG* tech. rep. MVOW-V164-V174-TOOL-03004-R00 (Oct. 2020).
31. Gaunaa, M., Heinz, J. & Skrzypiński, W. *Toward an Engineering Model for the Aerodynamic Forces Acting on Wind Turbine Blades in Quasisteady Standstill and Blade Installation Situations* in. **753** (Institute of Physics Publishing, Oct. 2016).
32. *Lifting Operations (VMO Standard - Part 2-5)* Standard (Det Norske Veritas, 2014).
33. Vremac. *Vremac Cylinders - Cylinder Catalogue 210 bar / 320 bar* https://vremac.com/product/hydraulic-cylinders/. Accessed: 2023-04-19. 2023.
34. Advani, S. K. *The Kinematic Design of Flight Simulator Motion-Bases* (Delft University of Technology, Apr. 1998).
35. Ma, O. & Angeles, J. *Architecture singularities of platform manipulators* in. **2** (Publ by IEEE, 1991), 1542–1547.
36. *UNIVERSAL JOINTS (CROSSES), CARDAN SHAFTS AND COMPONENTS | Sicit* https://www.sicit.it/en/our-products. Accessed: 2023-07-13.
37. *Leica Viva TS15 - Data sheet | Leica* https://www.gefos-leica.cz/ftp/Monitoring/TS15_DAT_en.pdf. Accessed: 2023-07-13.
38. *Leica Nova TS60 - Data sheet | Leica* https://leica-geosystems.com/id-id/products/total-stations/robotic-total-stations/leica-nova-ts60. Accessed: 2023-07-13.
39. *Laser Distance Sensor LDI-V110 - Series. Technical Reference Manual | Waycon* https://www.waycon.de/fileadmin/laser-sensors/Manual-LDI-Series.pdf. Accessed: 2023-07-13.
40. *Hydrins - Navigation-grade INS for hydrographic survey - Data sheet | iXblue* https://www.ixblue.com/wp-content/uploads/2021/12/hydrins-ins-datasheet.pdf. Accessed: 2023-07-13.
41. *MGC R5 COMPASS - Data sheet | Kongsberg* https://www.kongsberg.com/contentassets/9c7466e11a8d427bb564104e1a0a9f4a/datasheet_mgc_r5gc.pdf. Accessed: 2023-07-13.
42. *MRU 5+ MK-II - Data sheet | Kongsberg* https://www.kongsberg.com/globalassets/maritime/km-products/product-documents/mru-5-mk-ii---the-ultimate-marine-motion-sensor. Accessed: 2023-07-13.
43. Bosma, B. & Lomonaco, P. Motion Tracking Above and Below Water Dataset. https://www.osti.gov/biblio/1843796 (Apr. 2021).
44. Maletsky, L. P., Sun, J. & Morton, N. A. Accuracy of an optical active-marker system to track the relative motion of rigid bodies. *Journal of Biomechanics* **40,** 682–685. ISSN: 00219290 (3 2007).

45. Kongsberg. *RADius - Short-Range relative positioning system* (). https://www.kongsberg.com/contentassets/afb048f8c2584b379af4b51eed83d2e7/datasheet_radius.pdf.

46. Maes, K., Roeck, G. D. & Lombaert, G. Motion tracking of a wind turbine blade during lifting using RTK-GPS/INS. *Engineering Structures* **172,** 285–292. ISSN: 01410296. https://linkinghub.elsevier.com/retrieve/pii/S0141029617301827 (Oct. 2018).

47. Jiang, L. A., Albota, M. A., Haupt, R. W., Chen, J. G. & Marino, R. M. *Laser vibrometry from a moving ground vehicle* (2011).

48. Jin, Y., Dollevoet, R. & Li, Z. Numerical simulation and characterization of speckle noise for laser Doppler vibrometer on moving platforms (LDVom). *Optics and Lasers in Engineering* **158.** ISSN: 01438166 (Nov. 2022).

49. Albers, P. *Motion Control in Offshore and Dredging* 1st ed. ISBN: 978-90-481-8803-1 (Springer Dordrecht, June 2010).

50. Jensen, K. J., Ebbesen, M. K. & Hansen, M. R. Adaptive feedforward control of a pressure compensated differential cylinder. *Applied Sciences (Switzerland)* **10,** 1–19. ISSN: 20763417 (21 Nov. 2020).

51. Mareels, I. M., Anderson, B. D., Bitmead, R. R., Bodson, M. & Sastry, S. S. Revisiting the Mit Rule for Adaptive Control. *IFAC Proceedings Volumes* **20.** 2nd IFAC Workshop on Adaptive Systems in Control and Signal Processing 1986, Lund, Sweden, 30 June-2 July 1986, 161–166. ISSN: 1474-6670. https://www.sciencedirect.com/science/article/pii/S1474667017559546 (1987).

52. Lucky, R. W. Techniques for adaptive equalization of digital communication systems. *The Bell System Technical Journal* **45,** 255–286 (1966).

53. *In pictures – the world's longest wind turbine rotor blades | Power Technology* https://www.power-technology.com/features/featurein-pictures-longest-wind-turbine-rotor-blades. Accessed: 2023-07-13.

54. Jiang, Z., Gao, Z., Ren, Z., Li, Y. & Duan, L. A parametric study on the final blade installation process for monopile wind turbines under rough environmental conditions. *Engineering Structures* **172,** 1042–1056. ISSN: 18737323 (Oct. 2018).

55. Sander, A., Meinhardt, C. & Thoben, K. D. *Monitoring of offshore wind turbines under wave and wind loading during installation* in. **1** (European Association for Structural Dynamics, 2020), 2189–2205. ISBN: 9786188507203.

56. SE, H. M. C. N. *RNA Support Tower Detailed Design* tech. rep. CP0532-NI500-RP02 Rev. A (Nov. 2021).

57. *Environmental conditions and environmental loads* Standard (Det Norske Veritas, 2017).

# Nomenclature

## Abbreviations

| Abbreviation | Definition |
|---|---|
| Abs. | Absolute |
| AeroDyn | Aerodynamics software library from NREL |
| BEM | Blade Element Momentum |
| BIT | Blade Installation Tool |
| CoG | Center of Gravity |
| Cyl. | Cylinder |
| DAF | Dynamic Amplification Factor |
| DoF | Degrees of Freedom |
| DP | Dynamic Positioning |
| FB | Feedback |
| FF | Feedforward |
| GREP | Guided Root End Positioning |
| HMC | Heerema Marine Contractors |
| HPU | Hydraulic Power Unit |
| JONSWAP | Joint North Sea Wave Analysis Project |
| LC | Load Case |
| LDV | Laser Doppler Vibrometry |
| Max. | Maximum |
| Min. | Minimum |
| MIT(-rule) | Massachusetts Institute of Technology |
| MRU | Motion Reference Unit |
| NREL | National Renewable Energy Laboratory |
| Num. | Number |
| OpEx | Operating expense |
| PI | Proportional-Integral |
| ppm | Parts per million |
| PSD | Power Spectral Density |
| RNA | Rotor Nacelle Assembly |
| RTK | Real Time Kinematics |
| SSCV | Semi-submersible Crane Vessel |
| Std. | Standard deviation |
| Vel. | Velocity |
| WITV | Wind turbine Installation Vessel |
| WTG | Wind Turbine Generator |

## Symbols

| Symbol | Definition |
|---|---|
| $\mathbf{a}$ | Vector containing the third column of the rotation matrix |
| $A$ | Cross-section area |
| $A_{bore}$ | Cylinder's cross section area in the piston side |
| $A_{cyl}$ | Hydraulic cylinder, actuator, cross section area |
| $\mathbf{A_{Nacelle}}$ | Nacelle's area subjected to aerodynamic drag |

| Symbol | Definition |
|---|---|
| $\mathbf{a_P}$ | Platform's acceleration in platform reference system |
| $A_{rod}$ | Cylinder's cross section area in the rod side (ring area) |
| $\mathbf{B_B}$ | Base's joint coordinate in the base reference system |
| $\mathbf{B_V}$ | Base's joint coordinate in the vessel reference system |
| $\mathbf{BR_V}$ | Blade root position set point in vessel reference system |
| $\dot{\mathbf{BR}}_\mathbf{V}$ | Blade root velocity set point in vessel reference system |
| $\mathbf{C}$ | Structural dampiung matrix |
| $C_D$ | Drag coefficient |
| $\mathbf{C_{D,Nacelle}}$ | Nacelle's drag coefficient |
| $\mathbf{C_{IP}}$ | Axuliary vector containing inertia properties, in platform reference system |
| $\mathbf{C_{PE}}$ | Vector with external moments acting on the platform in the platform reference system |
| $D$ | Diameter |
| $d$ | Blade distributed aerodynamic drag |
| $E$ | Young's modulus |
| $e$ | Error between actuator length response and set point |
| $\mathbf{f}$ | Vector containing the forces on each actuator |
| $F$ | Effective degrees of freedom of the mechanism |
| $f$ | Joint's number of degrees of freedom |
| $f_a$ | Number of degrees of freedom at actuator level |
| $f_b$ | Number of degrees of freedom at base level |
| $\mathbf{F_{Drag,Nacelle}}$ | Aerodynamic drag force on nacelle |
| $f_p$ | Number of degrees of freedom at platform level |
| $\mathbf{a_P}$ | Vector with external forces acting on the platform in the platform reference system |
| $\mathbf{f_{TD}}$ | Aerodynamic drag distributed along installation tower height |
| $G$ | Shear modulus |
| $\mathbf{g_P}$ | Gravity vector in platform reference system |
| $H_S$ | Significant Wave height |
| $I$ | Cross-section moment of inertia |
| $\mathbf{I_P}$ | Matrix with the mass moment of inertia of the bodies controlled by the platform, in platform reference system |
| $\mathbf{I}_r$ | Mass moment of inertia tensor |
| $\mathbf{J}$ | Jacobian |
| $J$ | Polar moment of inertia |
| $J_t$ | Torque constant |
| $k$ | Variable in the cross-flow correction factor |
| $\mathbf{K}$ | Stiffness matrix |
| $K_{A-frame}$ | Crane's A-frame horizontal stiffness |
| $K_{Boom}$ | Crane's boom horizontal stiffness |
| $K_{Crane}$ | Equivalent crane horizontal stiffness |
| $K_{Derrick}$ | Crane's derrick wires horizontal stiffness |
| $k_{FF}$ | Feedforward fixed control gain |
| $k_P$ | Proportional feedback control gain |
| $l$ | Actuator length response. Or Blade distributed aerodynamic lift |
| $L_b$ | Length of base long side |
| $l_b$ | Length of base short side |
| $l_{dead}$ | Cylinder dead length |
| $l_{IK}$ | Desired actuator length |
| $\dot{l}_{IK}$ | Desired actuator velocity |
| $\dot{l}_{lim}$ | Limit actuator velocity |
| $l_m$ | Actuator response measurement |
| $l_{max}$ | Cylinder maximum length |
| $l_{min}$ | Cylinder minimum length |
| $L_p$ | Length of platform long side |
| $l_p$ | Length of platform short side |

| Symbol | Definition |
|---|---|
| $l_{P,SP}$ | Actuator length set point from hub's predicted motions |
| $\dot{l}_{P,SP}$ | Actuator velocity set point from hub's predicted velocities |
| $l_{SP}$ | Actuator length set point |
| $\dot{l}_{SP}$ | Actuator velocity set point |
| $ld$ | Steady error from sensor measurements |
| $m$ | Mass. Or blade distributed aerodynamic moment |
| $\mathbf{M}$ | Mass matrix. Or external bending moment |
| $\mathbf{M_V}$ | Normalized leg moment vector in vessel reference system |
| $\mathbf{M'_V}$ | Leg moment vector in vessel reference system |
| $\mathbf{n}$ | Vector containing the first column of the rotation matrix |
| $n_a$ | Number of linear actuators |
| $n_j$ | Number of joints in the mechanism |
| $n_l$ | Number of links in the mechanism |
| $\mathbf{o}$ | Vector containing the second column of the rotation matrix |
| $\mathbf{P}$ | External force |
| $\mathbf{P_P}$ | Platform's joint coordinate in the platform reference system |
| $\mathbf{P_{P,ST}}$ | Platform position set point in the vessel reference system from hub's predicted motions |
| $\dot{\mathbf{P}}_{\mathbf{P,ST}}$ | Platform velocity set point in the vessel reference system from hub's predicted velocities |
| $\mathbf{P_{ST}}$ | Platform position set point in vessel reference system |
| $\dot{\mathbf{P}}_{\mathbf{ST}}$ | Platform velocity set point in vessel reference system |
| $\mathbf{P_V}$ | Platform's joint coordinate in the vessel reference system. Or corresponding platform position, in vessel reference system, to $\mathbf{BR_V}$ |
| $\dot{\mathbf{P}}_{\mathbf{V}}$ | Corresponding platform velocity, in vessel reference system, to $\dot{\mathbf{BR}}_{\mathbf{V}}$ |
| $Q$ | HPU flowrate |
| $Q_{max}$ | Maximum HPU flowrate |
| $\mathbf{R}$ | Rotation matrix about z, y, x axes |
| $R$ | Cross-flow correction factor |
| $\mathbf{R_{V2B}}$ | Rotation matrix from base to vessel reference system |
| $\mathbf{R_{V2P}}$ | Rotation matrix from platform to vessel reference system |
| $\mathbf{R_{P2B}}$ | Rotation matrix from platform to base reference system |
| $\mathbf{R}_x$ | Rotation matrix about x axis |
| $\mathbf{R}_y$ | Rotation matrix about y axis |
| $\mathbf{R}_z$ | Rotation matrix about z axis |
| $s$ | Blade span coordinate. Or the complex frequency domain parameter from the Laplace transform. |
| $s_{tip}$ | Blade tip span coordinate |
| $\mathbf{S_V}$ | Leg vector in vessel reference system |
| $\mathbf{s_V}$ | Normalized leg vector in vessel reference system |
| $\mathbf{T}$ | Translation vector |
| $t$ | Time |
| $T_P$ | Wave peak period |
| $\mathbf{T_{V2B}}$ | Translation vector from base to vessel reference system |
| $\mathbf{T_{V2P}}$ | Translation vector from platform to vessel reference system |
| $u$ | Control variable, servo valve position. Or Installation tower displacement along its height in the local x direction |
| $\mathbf{u}$ | Installation tower displacement along its height |
| $u_{FB}$ | Control variable from feedback control loop |
| $u_{FF}$ | Control variable from feedforward control loop |
| $\mathbf{U_P}$ | Normalized vector of Plücker coordinates in platform reference system |
| $\mathbf{U_V}$ | Normalized vector of Plücker coordinates in vessel reference system |
| $v$ | Installation tower displacement along its height in the local y direction |
| $\mathbf{V_{wind,global}}$ | Wind velocity at reference height |

| Symbol | Definition |
|---|---|
| $\mathbf{V_{wind,rel}}$ | Relative wind velocity |
| $\mathbf{X}$ | Position and orientation vector |
| $\dot{\mathbf{X}}_{B1V}$ | Base 6 DoF velocity vector in vessel reference system |
| $\mathbf{X_F}$ | Filtered hub motions |
| $\dot{\mathbf{X}}_\mathbf{F}$ | Filtered hub velocities |
| $\mathbf{X_P}$ | Predicted hub motions |
| $\dot{\mathbf{X}}_\mathbf{P}$ | Predicted hub velocity |
| $\dot{\mathbf{X}}_{P1V}$ | Platform 6 DoF velocity vector in vessel reference system |
| $\mathbf{X_R}$ | Raw hub motions from sensors |
| $\dot{\mathbf{X}}_\mathbf{R}$ | Raw hub velocities from sensors |
| $X_s$ | Simulated measurement |
| $\mathbf{X_V}$ | Filtered hub motions in vessel reference system |
| $\dot{\mathbf{X}}_\mathbf{V}$ | Filtered hub velocities in vessel reference system |
| $z_{ff}$ | Adaptive feedforward control gain |
| $\dot{z}_{ff}$ | Time derivative of the adaptive feedforward control gain |
| $z_{hub}$ | Hub height, hub on top of the installation tower |
| $z_{ref}$ | Reference height |
| $\alpha$ | Angle about x axis. Or wind shear exponent. Or angle of attack. |
| $\beta$ | Angle about y axis. Or blade pitch angle |
| $\gamma$ | Angle about z axis. Or constant parameter of the adaptive feedforward control gain |
| $\eta_{tb}$ | Vessel's response on the installation tower's base |
| $\theta$ | Wind direction as observed by blade |
| $\theta'$ | Wind direction |
| $\kappa$ | Stewart platform's condition number |
| $\lambda$ | Degrees of freedom of the space in which the mechanism operates. Or structural damping stiffness proportionality constant |
| $\mu$ | Structural damping mass proportionality constant |
| $\nu$ | Poisson ratio |
| $\xi$ | Structural damping ratio |
| $\rho$ | Density |
| $\rho_{air}$ | Air density |
| $\sigma$ | Leg length |
| $\sigma$ | Standard deviation of sensor measurement error |
| $\dot{\sigma}$ | Leg speed |
| $\tau_i$ | Integral term from the integral feedback control gain. |
| $\phi$ | Orientation vector |
| $\psi$ | Installation tower rotations along its height |
| $\omega$ | Angular frequency |
| $\omega_P$ | Platform's rotational velocity vector in platform reference system |
| $\dot{\omega}_P$ | Platform's rotational acceleration vector in platform reference system |

# List of Figures

# List of Tables

# A

# Derivation of Equations of Motion for the installation tower

## A.1. Vessel response due to installation tower

The installation tower is modeled as a dynamic beam containing an inertial lumped mass on top representing the nacelle, hub, and possibly up to two blades installed.

In order to consider that the installation tower can be modeled as an isolated body from the vessel, where the vessel's responses (surge, sway, heave, roll, pitch and yaw) are transmitted to the tower's base as boundary conditions to solve the equations of motion, it becomes necessary to verify if the set (nacelle, hub and two blades) mounted on the installation tower influences the vessel's response. To assess the possible influence of the installation tower on the vessel's response, 24 simulations were carried out using OrcaFlex, where 12 simulations were performed with the vessel only, and the other 12 simulations were done under the same environmental conditions and the complete set mounted on the vessel. The two configurations are shown in Figure A.1.

The 12 different configurations of the environmental conditions simulated are presented in Table A.1. Simulations were performed using a uniform and constant wind field, as well as regular waves. The directions are: $0^\circ$ coming from the stern and $-90^\circ$ coming from the portside.

The vessel response (surge, sway, heave, roll, pitch, and yaw) is processed for all 24 simulations, and the difference in the response between the cases with and without the blade installation facility (installation tower) is analyzed. Because the response of the vessel, under these environmental loads, is mainly cyclical around zero, the mean response is not considered. The parameters chosen to as-

**Table A.1:** Environmental conditions used in the simulations

| Configuration # | Wave height [m] | Wave period [s] | Wave direction [°] | Wind speed [m/s] | Wind direction [°] |
|---|---|---|---|---|---|
| 1 | 4.0 | 8 | 0 | 0 | 0 |
| 2 | 4.0 | 8 | 0 | 12 | 0 |
| 3 | 4.0 | 8 | 0 | 12 | -30 |
| 4 | 4.0 | 8 | -30 | 0 | 0 |
| 5 | 4.0 | 8 | -30 | 12 | -30 |
| 6 | 4.0 | 8 | -30 | 12 | -60 |
| 7 | 4.0 | 8 | -60 | 0 | 0 |
| 8 | 4.0 | 8 | -60 | 12 | -60 |
| 9 | 4.0 | 8 | -60 | 12 | -90 |
| 10 | 4.0 | 8 | -90 | 0 | 0 |
| 11 | 4.0 | 8 | -90 | 12 | -90 |
| 12 | 4.0 | 8 | -90 | 12 | -120 |

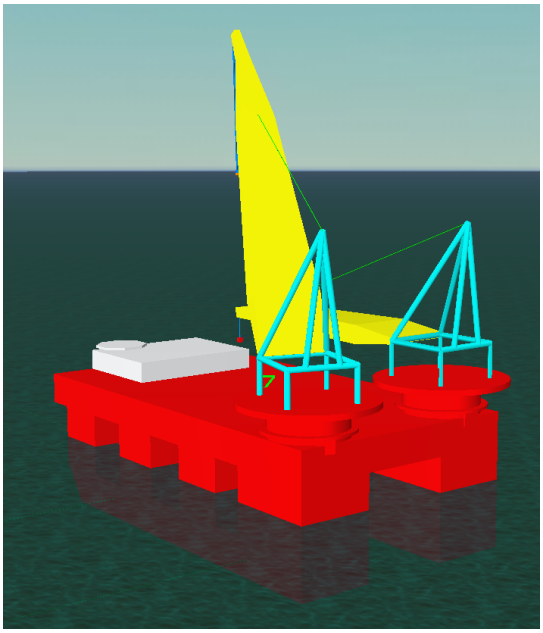

**(a)** SSCV Thialf without installation tower.

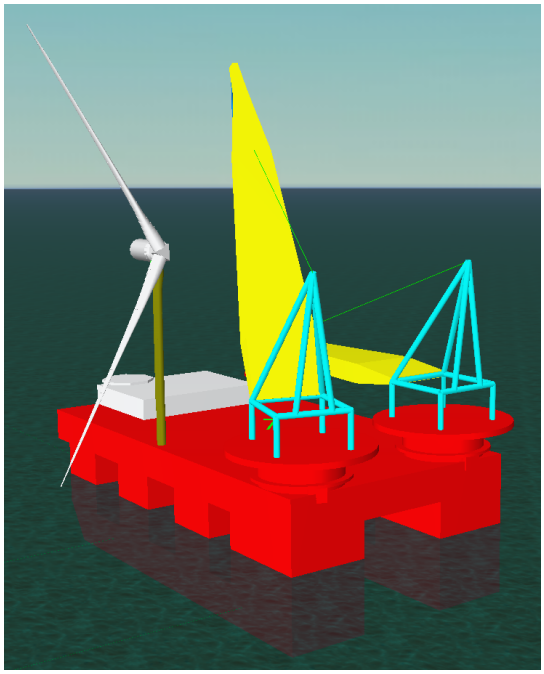

**(b)** SSCV Thialf with installation tower, nacelle, hub and two blades.

**Figure A.1:** OrcaFlex models of SSCV Thialf and same vessel with installation tower, nacelle, hub and blades mounted.

sess the influence of the installation tower in the vessel response are the standard deviation and the double amplitude of the difference between vessel's response with and without the installation tower. The results are presented in Figures A.2 and A.3.

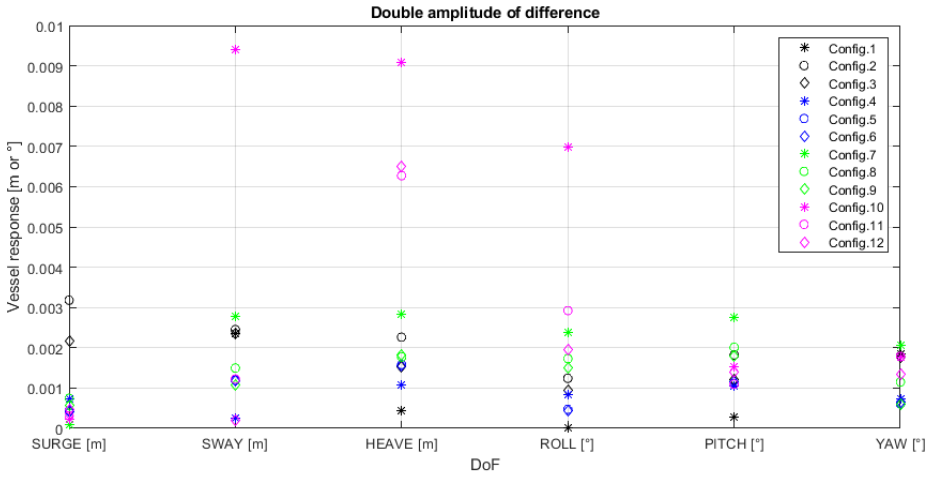


**Figure A.2:** Double amplitude of the difference in vessel response with and without the installation tower, nacelle, hub and two blades.

Analyzing the results presented in Figures A.2 and A.3, it is possible to notice that the influence of the set of 3rd blade aid installation sets (installation tower, nacelle, hub, and two blades) makes a minimum difference in the response of the vessel. Therefore, the equations of motion of the installation tower can be set up independently from the vessel in a way that the vessel response is directly translated to the tower base as excitation (boundary conditions).

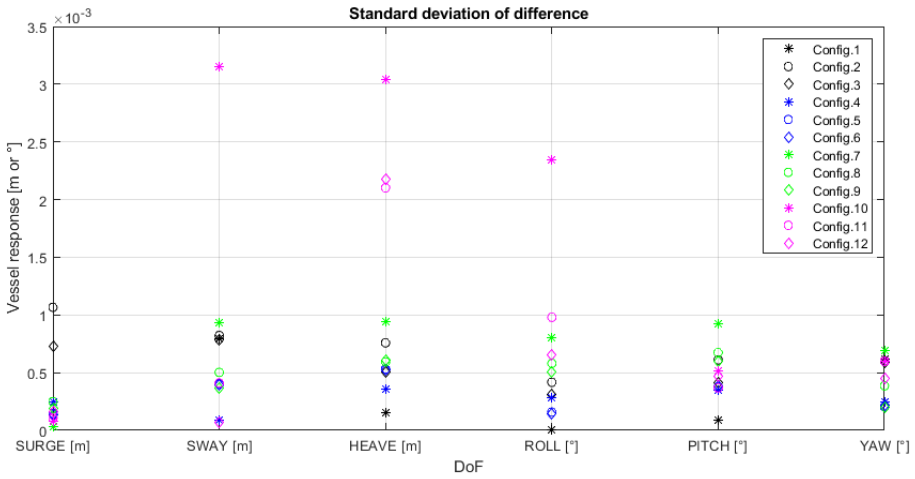


**Figure A.3:** Standard deviation of the difference in vessel response with and without the installation tower, nacelle, hub and two blades.

## A.2. Setting up the Equations of Motion (EoM)

The installation tower is modeled as a fully elastic body, using the superposition principle and the Euler-Bernoulli theory of beams. The local coordinate system is chosen to have its origin where the elastic part of the installation tower begins, with the $x-$ axis positive towards the bow, the $y-$ axis positive towards the portside, and the $z-$ axis positive upward along the longitudinal axis of the installation tower coinciding with its center line as depicted in Figure A.4.

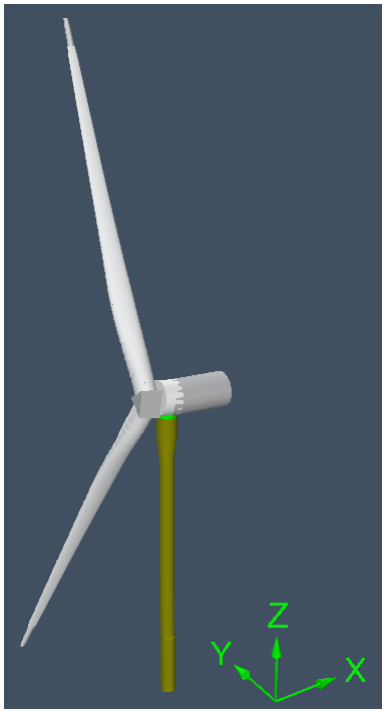


**Figure A.4:** Local coordinate system of the installation tower.

The installation tower's model will be used to calculate and/or estimate the gains of the controller used in motion-compensated Stewart platform for blade installation. As the system aims to compensate the relative motions between the blade root and the hub, the former connected to the crane's boom via the motion compensated Stewart platform, the elastic longitudinal motion of the installation tower can be neglected, therefore only five degrees of freedom of the installation tower are modeled, i.e. displacements in the $x-$ and $y-$ directions, as well as rotations around the $x-$, $y-$ and $z-$ axis.

The displacement along the installation tower in $x-$ and $y-$ directions is:

$$\mathbf{u} = (u, v)$$

The rotation along the installation tower around $x-$, $y-$ and $z-$ axis is:

$$\boldsymbol{\psi} = \left(\frac{\partial u}{\partial z}, \frac{\partial v}{\partial z}, \psi\right)$$

Furthermore, the response of the vessel at the base of the installation tower is defined as:

$$\boldsymbol{\eta}_{tb} = (\eta_{tb,1}, \eta_{tb,2}, \eta_{tb,3}, \eta_{tb,4}, \eta_{tb,5}, \eta_{tb,6})$$

Where $\eta_{tb,1}$, $\eta_{tb,2}$, $\eta_{tb,3}$, $\eta_{tb,4}$, $\eta_{tb,5}$ and $\eta_{tb,6}$ are, respectively, the surge, sway, heave, roll, pitch and yaw of the vessel translated to the base of the tower.

From the Euler-Bernoulli beam theory, the tower deflections in the $x-$ and $y-$ directions are modeled as follows:

$$\rho A \frac{\partial^2 \mathbf{u}}{\partial t^2} + \frac{\partial^2}{\partial z^2}\left(EI \frac{\partial^2 \mathbf{u}}{\partial z^2}\right) = \mathbf{f_{TD}} \tag{A.1}$$

Where $\rho$ is the mass density of the installation tower material, $A(z)$ is the cross-sectional area of the installation tower, $E$ is the Young's modulus of the material, and $I(z)$ is the moment of inertia of the cross section. One must note that, due to the symmetrical properties of the installation tower, the moment of inertia of the cross section is equal in the $x-$ and $y-$ directions. $f_{TD}$ is the distributed aerodynamic load acting on the installation tower, i.e. tower drag.

The boundary conditions at the base of the tower $(z = 0)$ for the bending problem are:

$$u(z=0) = \eta_{tb,1}(t) \tag{A.2a}$$

$$v(z=0) = \eta_{tb,2}(t) \tag{A.2b}$$

$$\left.\frac{\partial u}{\partial z}\right|_{z=0} = \eta_{tb,5}(t) \tag{A.2c}$$

$$\left.\frac{\partial v}{\partial z}\right|_{z=0} = \eta_{tb,4}(t) \tag{A.2d}$$

Meanwhile, at the hub height $(z = L)$, the boundary conditions are:

$$\left.\frac{\partial^2 \mathbf{u}}{\partial z^2}\right|_{z=L} = -\frac{\mathbf{I_r}}{EI}\left.\frac{\partial^3 \mathbf{u}}{\partial t^2 \partial z}\right|_{z=L} \tag{A.3a}$$

$$\left.EI\frac{\partial^2 \mathbf{u}}{\partial z^2}\right|_{z=L} = -\mathbf{M}(t) \tag{A.3b}$$

$$\left.EI\frac{\partial^3 \mathbf{u}}{\partial z^3}\right|_{z=L} = -\mathbf{P}(t) \tag{A.3c}$$

Where $\mathbf{I_r}$ is the tensor that contains the mass moment of inertia around the body's local coordinate system $x-$ and $y-$ axis, respectively $I_{xx}$ and $I_{yy}$. $\mathbf{M}$ is the vector containing the external bending moment around the $x-$ and $y-$ axes that act on top of the installation tower, and $\mathbf{P}$ is the vector containing the external force in $x-$ and $y-$ directions that act on top of the installation tower.

Similarly, for the torsion along the installation tower, it is modeled as a rod under torsion, following the constitutive equation below:

$$\rho J \frac{\partial^2 \psi}{\partial t^2} = \frac{\partial \psi}{\partial z}\left(GJ_t \frac{\partial \psi}{\partial z}\right) \tag{A.4}$$

Where $J(z)$ is the polar moment of inertia along the installation tower, $G$ is the shear modulus of the tower material, and $J_t(z)$ is the torque constant. For a circular cross section, such as the installation tower, $J(z) = J_t(z)$, therefore, Equation A.4 can be written as:

$$\rho J \frac{\partial^2 \psi}{\partial t^2} = \frac{\partial \psi}{\partial z}\left(GJ \frac{\partial \psi}{\partial z}\right) \tag{A.5}$$

The boundary condition for the torsion problem at the base of the tower $(z = 0)$ is:

$$\psi(z = 0) = \eta_{tb,6}(t) \tag{A.6}$$

Meanwhile, at the hub height $(z = L)$, the boundary conditions are:

$$GJ\frac{\partial\psi}{\partial z}\bigg|_{z=L} = M_t^{ext} \tag{A.7a}$$

$$GJ\frac{\partial\psi}{\partial z}\bigg|_{z=L} = -I_t\frac{\partial^2\psi}{\partial t^2} \tag{A.7b}$$

Where $M_t^{ext}$ is the external torque around the $z-$ axis due to aerodynamic loads acting on top of the installation tower, and $I_t$ is the moment of inertia of the body on top of the installation tower that opposes the torque.

## A.3. Installation tower properties

The installation tower is a steel structure with homogeneous and isotropic material. It is composed of circular cross sections that may differ not only in diameter but also in thickness. The installation tower is 65 m high and its schematic representation can be seen in Figure A.5.

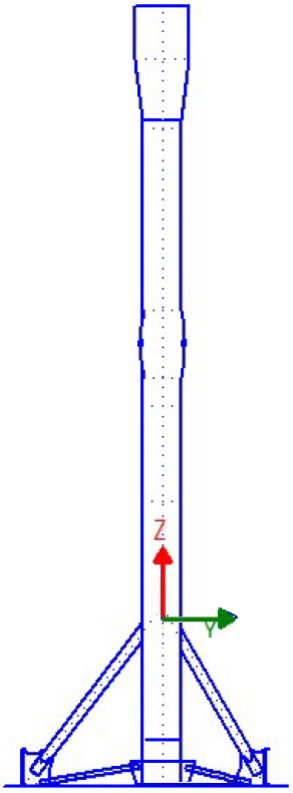


**Figure A.5:** installation tower schematic representation [56].

The structural steel used in the installation tower has a Young modulus of $E = 212$ GPa, a Poisson ratio of $\nu = 0.293$ and therefore a shear modulus of $G = 82$ GPa. The mass density of the material is $\rho = 7.85$ te / m.

From Figure A.5 it can be observed that there are bracings connecting the installation tower to the deck of the vessel, and therefore this specific section of the installation tower can be considered to be rigid in both bending and torsion. The vertical distance, along the local $z-$ axis, from the deck of the vessel and where the bracings are welded to the tower structure is $13.08$m, this position is the origin of the local coordinate system, that is, $(x, y, z) = (0, 0, 0)$, and the position where the installation tower is welded to the deck of the vessel is $(0, 0, -13.08)$, while the top of the tower is at $(0, 0, 51.92)$.

The physical properties of the installation tower are graphically presented in Figure A.6 with numerical values in Table A.2. The collection of data presented was chosen specifically due to their relevance for the equations in Section A.2.

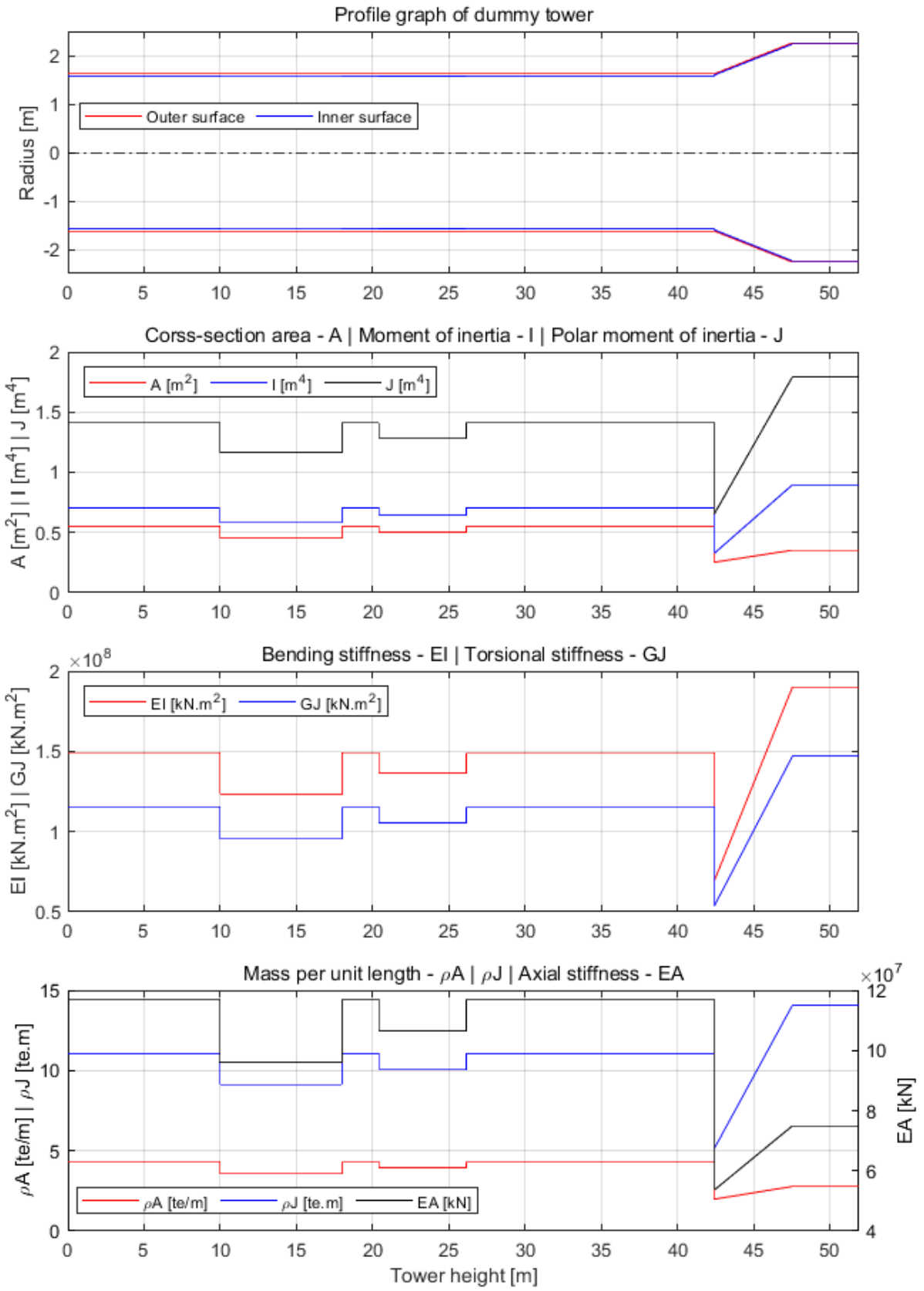


**Figure A.6:** installation tower structural and physical properties.

**Table A.2:** installation tower structural and physical properties

| Tower height [m] | Inner diameter [m] | Outer diameter [m] | Thickness [mm] | A [$m^2$] | $\rho$A [te/m] | EA [kN] | I [$m^4$] | EI [kN.$m^2$] | J [$m^4$] | $\rho$J [te.m] | GJ [kN.$m^2$] |
|---|---|---|---|---|---|---|---|---|---|---|---|
| 0 | 3.14 | 3.25 | 55 | 0.55 | 4.33 | $117{\cdot}10^6$ | 0.70 | $149{\cdot}10^6$ | 1.41 | 11.06 | $116{\cdot}10^6$ |
| 10 | 3.16 | 3.25 | 45 | 0.45 | 3.56 | $96{\cdot}10^6$ | 0.58 | $123{\cdot}10^6$ | 1.16 | 9.14 | $95{\cdot}10^6$ |
| 18 | 3.14 | 3.25 | 55 | 0.55 | 4.33 | $117{\cdot}10^6$ | 0.70 | $149{\cdot}10^6$ | 1.41 | 11.06 | $116{\cdot}10^6$ |
| 20.4 | 3.15 | 3.25 | 50 | 0.50 | 3.94 | $106{\cdot}10^6$ | 0.64 | $136{\cdot}10^6$ | 1.29 | 10.10 | $106{\cdot}10^6$ |
| 26.145 | 3.14 | 3.25 | 55 | 0.55 | 4.33 | $117{\cdot}10^6$ | 0.70 | $149{\cdot}10^6$ | 1.41 | 11.06 | $116{\cdot}10^6$ |
| 42.445 | 3.2 | 3.25 | 25 | 0.25 | 1.99 | $54{\cdot}10^6$ | 0.33 | $70{\cdot}10^6$ | 0.66 | 5.17 | $54{\cdot}10^6$ |
| 47.561 | 4.479 | 4.529 | 25 | 0.35 | 2.78 | $75{\cdot}10^6$ | 0.90 | $190{\cdot}10^6$ | 1.79 | 14.08 | $147{\cdot}10^6$ |
| 51.92 | 4.479 | 4.529 | 25 | 0.35 | 2.78 | $75{\cdot}10^6$ | 0.90 | $190{\cdot}10^6$ | 1.79 | 14.08 | $147{\cdot}10^6$ |

In addition to the properties presented in Figures A.6 and A.2, structural damping is also considered in the modeling of the behavior of the installation tower, for this stiffness proportional Rayleigh structural damping was introduced in Section A.2. The damping coefficient already modeled in OrcaFlex is stiffness proportional and has a damping coefficient of 1% for the response period of 0.75s.

# A.4. External forces

The external forces acting on and exitations transmitted to the installation tower are listed below:

- Aerodynamic drag force on the installation tower.
- Aerodynamic drag force on the nacelle.
- Aerodynamic forces on the blades, if there is a blade installed on the nacelle.
- Vessel's motions transmitted to the tower base.

## A.4.1. Aerodynamic drag on installation tower

The aerodynamic drag force per unit length that acts on the tower is modeled as follows:

$$\mathbf{f_{TD}}(z,t) = \frac{1}{2}\rho_{air} D(z) C_D(z) \mathbf{V_{wind,rel}}(z,t) |\mathbf{V_{wind,rel}}(z,t)| \tag{A.8}$$

The relative wind speed $\mathbf{V_{wind,rel}}$ is the wind speed in the $x-$ and $y-$ directions, as seen by the tower, as formulated below.

$$\mathbf{V_{wind,rel}}(z,t) = \mathbf{V_{wind,global}}(z,t) - \dot{\mathbf{u}}(z,t) \tag{A.9}$$

The simplified model set up in this section will not account for turbulent wind; nevertheless, the wind shear effect is considered using the power law profile, where the power law exponent is defined as $\alpha = 0.12$ in [57].

$$\mathbf{V_{wind,global}}(z,t) = \mathbf{V_{wind,global}}(t)|_{z=z_{ref}} \left(\frac{z}{z_{ref}}\right)^{\alpha} \tag{A.10}$$

Where $\mathbf{V_{wind,global}}(t)|_{z=ref}$ is a 2D vector that contains the wind speed in the $x-$ and $y-$ directions at the reference height $z = ref$, usually 10 m. Therefore, Equation A.8 can be written as:

$$\begin{aligned}\mathbf{f_{TD}}(z,t) = \frac{1}{2}\rho_{air} D(z) C_D(z) \Bigg(\mathbf{V_{wind,global}}(t)|_{z=z_{ref}} \left(\frac{z}{z_{ref}}\right)^{\alpha} - \dot{\mathbf{u}}(z,t)\Bigg) \\ \left|\mathbf{V_{wind,global}}(t)|_{z=z_{ref}} \left(\frac{z}{z_{ref}}\right)^{\alpha} - \dot{\mathbf{u}}(z,t)\right|\end{aligned} \tag{A.11}$$

### A.4.2. Aerodynamic drag on nacelle

The nacelle is also subject to aerodynamic drag forces, and similarly to the drag force on the installation tower, the former is formulated as follows:

$$\mathbf{F}_{\mathbf{Drag,Nacelle}} = \frac{1}{2}\rho_{air}\mathbf{A}_{\mathbf{Nacelle}}\mathbf{C}_{\mathbf{D,Nacelle}} \left(\mathbf{V}_{\mathbf{wind,global}}(t)|_{z=z_{ref}} \left(\frac{z_{hub}}{z_{ref}}\right)^{\alpha} - \dot{\mathbf{u}}(z=L,t)\right) \left|\mathbf{V}_{\mathbf{wind,global}}(t)|_{z=z_{ref}} \left(\frac{z_{hub}}{z_{ref}}\right)^{\alpha} - \dot{\mathbf{u}}(z=L,t)\right| \tag{A.12}$$

Where $z_{hub}$ is the height of the tower from the water level. It is important to point out that the drag forces in the $x-$ and $y-$ directions calculated using Equation A.12 are point forces acting on the center of the projected nacelle area in the $y-z$ and $x-z$ planes, and because the center of the projected nacelle area in the $x-z$ plane does not fall on the local $z-$ axis, the resulting aerodynamic drag force of the nacelle will contribute to the force $\mathbf{P}(t)$ of Equation A.3 in the $y-$ direction, as well as the torque $M_t^{ext}$ of Equation A.7.

### A.4.3. Aerodynamic loads on the blades

The blades already installed in the hub and nacelle on top of the installation tower are subject to aerodynamic loads that are transmitted to the installation tower as forces and moments. Because the blades are not rotating, the loads on the blades cannot be calculated using the BEM (Blade Element Momentum) theory, for example. Taking blades as rigid bodies, the aerodynamic loads that act on them are calculated using the cross-flow method with a correction factor proposed in [31]. In the cross-flow sense, lift and drag are the forces perpendicular to and parallel to the normal flow component of the inflow vector only.

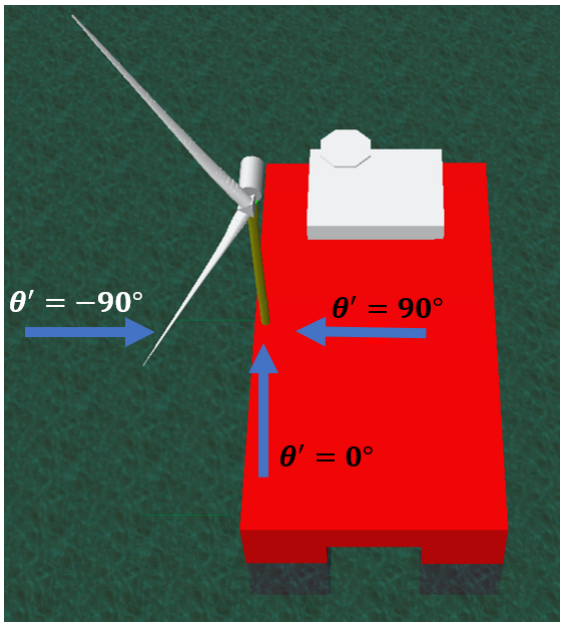


**Figure A.7:** Wind speed direction, $\theta'$, reference system.

In [31] the blades were considered horizontal; therefore, a change in wind direction affected only the inflow direction. For the blades on the installation tower, a change in wind direction changes not only the inflow angle but also the angle of attack. Because the blades are equally spaced, 120°, and the upper blade connected to the hub has a 30° angle relative to the vertical plane, the actual change in wind direction of 90° will be seen from the blade as a change of 30° in the direction of inflow and a change of 90° in the angle of attack.

The inflow angle as seen by the blades is:

$$\theta = \frac{\pi}{6}\sin\left(\theta' + \psi(z=L)\right) \tag{A.13}$$

Where $\theta'$ is the wind direction as depicted in Figure A.7. The angle of attack is calculated as follows:

$$\alpha = \theta' + \psi + \beta; \quad \theta' > 0 \tag{A.14a}$$

$$\alpha = \theta' + \psi - \beta; \quad \theta' \leq 0 \tag{A.14b}$$

Where $\beta$ is the pitch angle of the blade. With the inflow angle as seen by the blades and the angle of attack, it is possible to calculate the correction factor for the crossflow method proposed in [31].

$$\begin{aligned} R(\alpha, k, \theta) = \frac{2}{\pi} \cdot \arctan\left(40 \cdot k \cdot \left(1 + 1000 \cdot \operatorname{sech}\left(\frac{\theta}{2}\right)\right)\right) \cdot \\ \left(1 + |\sin\theta| \cdot \left(k - \frac{1}{4}\right) \cdot \left(\frac{8}{3} \cdot \sin^2\alpha + \frac{2}{3} \cdot |\sin\alpha| \cdot \sin^2 2\alpha\right)\right) \end{aligned} \tag{A.15}$$

Where:

$$\text{if} \quad \theta > 0: \quad k = s/s_{tip} \quad \text{else} \quad k = 1 - s/s_{tip}$$

Where $s$ is the span coordinate of the section and $s_{tip}$ is the span coordinate of the blade tip.

Having calculated the correction factor in Equation A.15, the lift and drag forces as well as the moment can be calculated.

$$l = R(\alpha, k, \theta)\frac{1}{2}C_l\rho_{air}\cos^2\theta\left(\mathbf{V}_{\mathbf{wind,global}}(t)|_{z=z_{ref}}\left(\frac{z}{z_{ref}}\right)^{\alpha} - \dot{\mathbf{u}}(z,t)\right)^2 \tag{A.16a}$$

$$d = R(\alpha, k, \theta)\frac{1}{2}C_d\rho_{air}\cos^2\theta\left(\mathbf{V}_{\mathbf{wind,global}}(t)|_{z=z_{ref}}\left(\frac{z}{z_{ref}}\right)^{\alpha} - \dot{\mathbf{u}}(z,t)\right)^2 \tag{A.16b}$$

$$m = R(\alpha, k, \theta)\frac{1}{2}C_m\rho_{air}\cos^2\theta\left(\mathbf{V}_{\mathbf{wind,global}}(t)|_{z=z_{ref}}\left(\frac{z}{z_{ref}}\right)^{\alpha} - \dot{\mathbf{u}}(z,t)\right)^2 \tag{A.16c}$$

## A.5. Model simplification and structural damping

### A.5.1. Model simplification

The model derived in Section A.2 is used in this thesis for two main purposes, i.e. to calculate the gains of the controller as well as the requirements for the Stewart platform's actuators (required stroke, velocity, acceleration, etc.). For these applications, the above-mentioned system of partial differential equations can be simplified in order to provide simpler and faster solutions. These simplifications are:

- Neglecting the relative velocity between wind, tower, nacelle, and blades. As the maximum wind speed for which the operation will occur is significantly higher than the response of the installation tower, the responses of the installation tower in Section A.4 are neglected.
- Considering that the tower has constant structural properties along its height. These properties are: EI (bending stiffness), GJ (torsional stiffness), $\rho$A (mass per unit length), EA (axial stiffness), and $\rho$J. The external diameter remains varying along the tower's height.

To obtain the equivalent structural properties of the installation tower, a weighted average was calculated integrating the distributed properties along the height of the tower and dividing it by the total height of the tower (51.92 m), and is presented graphically in Figure A.8.

Furthermore, Equations A.1 and A.5 are simplified, respectively, to:

**Table A.3:** Equivalent installation tower structural and physical properties

| Parameter | Value | Unit |
|---|---|---|
| EI - Bending stiffness | $145{\cdot}10^6$ | kN.m$^2$ |
| GJ - Torsional stiffness | $112{\cdot}10^6$ | kN.m$^2$ |
| $\rho$A - Mass per unit length | 3.85 | te/m |
| $\rho$J | 10.77 | te.m |
| EA - Axial stiffness | $104{\cdot}10^6$ | kN |

$$\rho A \frac{\partial^2 \mathbf{u}}{\partial t^2} + EI \frac{\partial^4 \mathbf{u}}{\partial z^4} = \mathbf{f_{TD}} \tag{A.17}$$

$$\rho J \frac{\partial^2 \psi}{\partial t^2} = GJ \frac{\partial^2 \psi}{\partial z^2} \tag{A.18}$$

Where $\rho$A, EI, $\rho$J and GJ are constant in space and time, their values are shown in Table A.3. The boundary conditions formulated in Section A.2 remain unchanged with respect to the physical and structural properties of the tower.

The external loads equations are simplified based on the fact that the installation tower's responses are considerably smaller than the maximum allowable wind speed for the blade installation operation, hence the equations in Section A.4 are simplified to neglect the tower's response compared to the wind speed. The aerodynamic drag on the installation tower, Equation A.11, becomes:

$$\mathbf{f_{TD}}(z,t) = \frac{1}{2}\rho_{air} D(z) C_D(z) \mathbf{V_{wind,global}}(t)|_{z=z_{ref}} \left(\frac{z}{z_{ref}}\right)^{2\alpha} \left|\mathbf{V_{wind,global}}(t)|_{z=z_{ref}}\right| \tag{A.19}$$

The aerodynamic drag on the nacelle, Equation A.12, becomes:

$$\mathbf{F_{Drag,Nacelle}} = \frac{1}{2}\rho_{air} \mathbf{A_{Nacelle}} \mathbf{C_{D,Nacelle}} \mathbf{V_{wind,global}}(t)|_{z=z_{ref}} \left(\frac{z_{hub}}{z_{ref}}\right)^{2\alpha} \left|\mathbf{V_{wind,global}}(t)|_{z=z_{ref}}\right| \tag{A.20}$$

Regarding the aerodynamic forces acting on the blades, the tower torsion, $\psi$, in Equation A.14, can be neglected as its contribution to the change in angle of attack is minimal. The same argument applies to the inflow angle as seen by the blades Equation A.13. Equations A.14 and A.13 become, respectively:

$$\alpha = \theta' + \beta; \quad \theta' > 0 \tag{A.21a}$$

$$\alpha = \theta' - \beta; \quad \theta' \leq 0 \tag{A.21b}$$

$$\theta = \frac{\pi}{6} \sin(\theta') \tag{A.22}$$

The simplified inflow angle and angle of attack are used to calculate the correction factor $R(\alpha, k, \theta)$ in Equation A.15, which is used to calculate the distributed loads acting on the blade(s) below:

$$l = R(\alpha,k,\theta)\frac{1}{2}\rho_{air} C_l \mathbf{V^2_{wind,global}}(t)|_{z=z_{ref}} \left(\frac{z}{z_{ref}}\right)^{2\alpha} \cos^2\theta \tag{A.23a}$$

$$d = R(\alpha,k,\theta)\frac{1}{2}\rho_{air} C_d \mathbf{V^2_{wind,global}}(t)|_{z=z_{ref}} \left(\frac{z}{z_{ref}}\right)^{2\alpha} \cos^2\theta \tag{A.23b}$$

$$m = R(\alpha,k,\theta)\frac{1}{2}\rho_{air} C_m \mathbf{V^2_{wind,global}}(t)|_{z=z_{ref}} \left(\frac{z}{z_{ref}}\right)^{2\alpha} \cos^2\theta \tag{A.23c}$$

### A.5.2. Structural damping

To reproduce the structural damping of the installation tower, Rayleigh damping is introduced. The damping matrix **C** is given by $\mathbf{C} = \mu\mathbf{M} + \lambda\mathbf{K}$, where **M** and **K** are the mass and stiffness matrices, respectively, and $\mu$ and $\lambda$ are constants of proportionality. The damping ratio, $\xi$, is a function of angular frequency and is formulated as follows:

$$\xi = \frac{1}{2}\left(\frac{\mu}{\omega} + \lambda\omega\right) \tag{A.24}$$

As can be observed from Equation A.24, if the Rayleigh structural damping is proportional to both the mass and the stiffness, the damping ratio at low frequencies becomes too large and unrealistic. For this reason, mainly, the installation tower is modeled with stiffness proportional damping only, with damping ratio $\xi = 1\%$ at a period of 0.75 s ($\omega \approx 8.38$rad/s). With this damping ratio at the specified frequency, the proportionality stiffness constant $\lambda$ can be calculated, and then the damping ratio as a function of the frequency is obtained.

$$\lambda = \frac{2\xi}{\omega} = \frac{2 \cdot 0.01 \cdot 0.75}{2\pi} \approx 0.00239\text{s}$$

After calculating the proportionality structural damping constant $\lambda$, it can be introduced into the equations of motion that govern the behavior of the installation tower, Equations A.17 and A.18. The system is presented below in matrix form.

$$\begin{bmatrix} \rho A & 0 & 0 \\ 0 & \rho A & 0 \\ 0 & 0 & \rho J \end{bmatrix} \begin{bmatrix} \ddot{u} \\ \ddot{v} \\ \ddot{\psi} \end{bmatrix} + \begin{bmatrix} \lambda EI\frac{\partial^4}{\partial z^4} & 0 & 0 \\ 0 & \lambda EI\frac{\partial^4}{\partial z^4} & 0 \\ 0 & 0 & -\lambda GJ\frac{\partial^2}{\partial z^2} \end{bmatrix} \begin{bmatrix} \dot{u} \\ \dot{v} \\ \dot{\psi} \end{bmatrix} + \begin{bmatrix} EI\frac{\partial^4}{\partial z^4} & 0 & 0 \\ 0 & EI\frac{\partial^4}{\partial z^4} & 0 \\ 0 & 0 & GJ\frac{\partial^2}{\partial z^2} \end{bmatrix} \begin{bmatrix} u \\ v \\ \psi \end{bmatrix} = \begin{bmatrix} f_{TD,x} \\ f_{TD,y} \\ 0 \end{bmatrix} \tag{A.25}$$

Where $f_{TD,x}$ and $f_{TD,y}$ are, respectively, the components $x-$ and $y-$ of aerodynamic tower drag according to Equation A.19, which can be rewritten as:

$$\begin{bmatrix} \rho A & 0 & 0 \\ 0 & \rho A & 0 \\ 0 & 0 & \rho J \end{bmatrix} \begin{bmatrix} \ddot{u} \\ \ddot{v} \\ \ddot{\psi} \end{bmatrix} + \begin{bmatrix} \lambda EI\frac{\partial^4}{\partial z^4} & 0 & 0 \\ 0 & \lambda EI\frac{\partial^4}{\partial z^4} & 0 \\ 0 & 0 & -\lambda GJ\frac{\partial^2}{\partial z^2} \end{bmatrix} \begin{bmatrix} \dot{u} \\ \dot{v} \\ \dot{\psi} \end{bmatrix} + \begin{bmatrix} EI\frac{\partial^4}{\partial z^4} & 0 & 0 \\ 0 & EI\frac{\partial^4}{\partial z^4} & 0 \\ 0 & 0 & GJ\frac{\partial^2}{\partial z^2} \end{bmatrix} \begin{bmatrix} u \\ v \\ \psi \end{bmatrix} = \begin{bmatrix} \frac{1}{2}\rho C_D(z) D(z) \left(\frac{z}{z_{ref}}\right)^{2\alpha} \|\mathbf{V_{wind}}\| \cos\theta' \\ \frac{1}{2}\rho C_D(z) D(z) \left(\frac{z}{z_{ref}}\right)^{2\alpha} \|\mathbf{V_{wind}}\| \sin\theta' \\ 0 \end{bmatrix} \tag{A.26}$$

Where $\|\mathbf{V_{wind}}\|$ is the magnitude of the wind velocity vector.

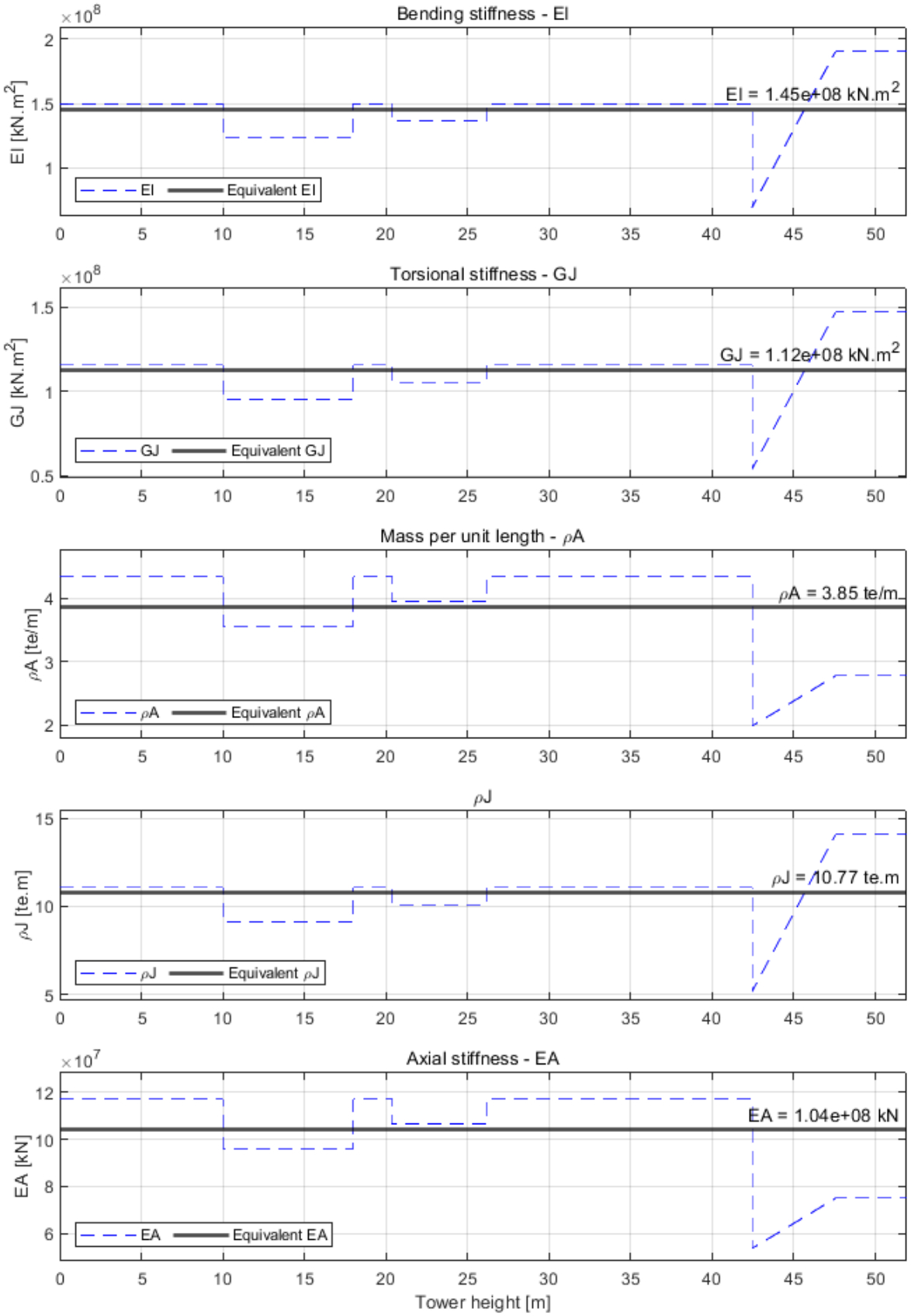


**Figure A.8:** Equivalent installation tower structural and physical properties.

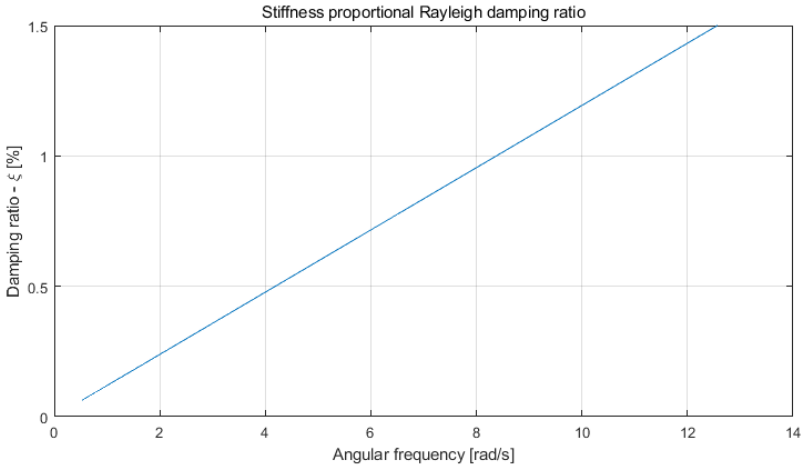


**Figure A.9:** Stiffness proportional damping ratio as a function of the frequency.

# B

# Aerodynamic loads acting on blade during installation

The Stewart platform and its actuators that hold the blades and lifting accessories must be designed to withstand all the loads during normal and abnormal operation conditions. Therefore, it becomes necessary to calculate the aerodynamic loads acting on the blade that are transmitted to the Stewart platform.

Similarly to the approach used to calculate the aerodynamic loads acting on the blades attached to the hub on the installation tower, the aerodynamic loads acting on the blade during installation are also calculated using the method proposed by [31] with the correction factor for the crossflow principle.

The aerodynamic loads acting on the blade are calculated for different configurations of incident wind direction, following the same coordinate system as in Figures A.4 and A.7, angle of attack and wind speeds. The angle of attack in the installation configuration is directly the blade pitch angle, for the blade in the horizontal position (installation position), the blade leading edge against the wind means an angle of attack $\alpha = 0°$, while the leading edge pointed upward represents an angle of attack $\alpha = 90°$. The wind speeds considered ranged from 4m / s to 16m / s with increments of 2m/s. The maximum wind speed used in the calculations was chosen to be in the upper range of the allowable limit for the blade lifting operation.

The correction factor $R(\alpha, k, \theta)$ in Equation A.15 is calculated for the different angles of attack and wind directions, then the distributed lift and drag forces on the length of the blade are calculated using Equation A.23 and disregarding the wind shear effect, given the fact that the blade is in the horizontal position, that is, it is not subject to variations of the wind speed in the $z-$ direction.

Distributed lift and drag forces are then integrated along the blade's length to result in the total lift and drag forces acting on the blade. Additionally, these forces are not acting directly on the blade's CoG (where it is being lifted from), therefore they will result in a moment that must be considered. Moments caused by the lift and drag forces are calculated around the blade's CoG, where the blade's CoG is at position $0$m, the root is at position $-20.8$m, and the blade's tip is at $63.0$m. The total aerodynamic force and moment acting on the blade are calculated by a vector sum of the lift and drag forces and moments, respectively.

Figures B.1 and B.2 represent, respectively, the total aerodynamic force and moment on the blade for a fixed wind speed of 16m/s as a function of the wind direction and angle of attack. Figures B.3 until B.6 show the total drag and lift forces and moments as a function of the wind direction for different wind speeds and angles of attack. Finally, Figure B.7 present the total aerodynamic force and moment as a function of wind direction at the angles of attack where the total force ($\alpha = 15°$) and the total moment ($\alpha = 90°$) are at its maximum values. Similarly, Figure B.8 presents the total aerodynamic force and

moment as a function of angle of attack in the wind directions where the total force ($\theta = 2°$) and the total moment ($\theta = 23°$) are at their maximum values.

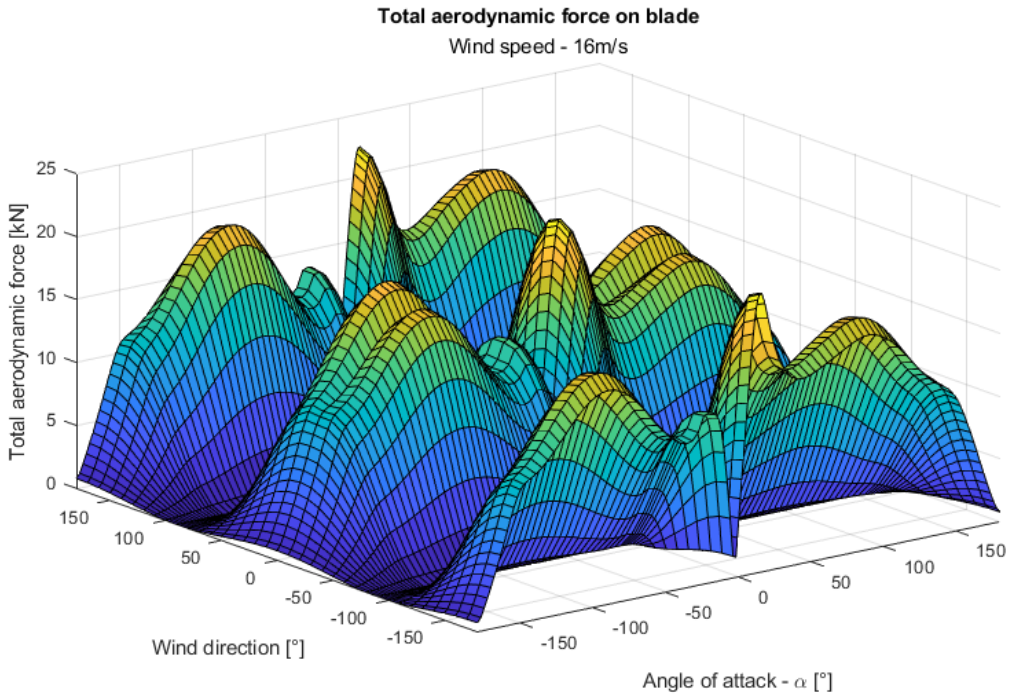


**Figure B.1:** Total aerodynamic forces acting on the blade as a function of wind direction and angle of attack. Wind speed of 16m/s.

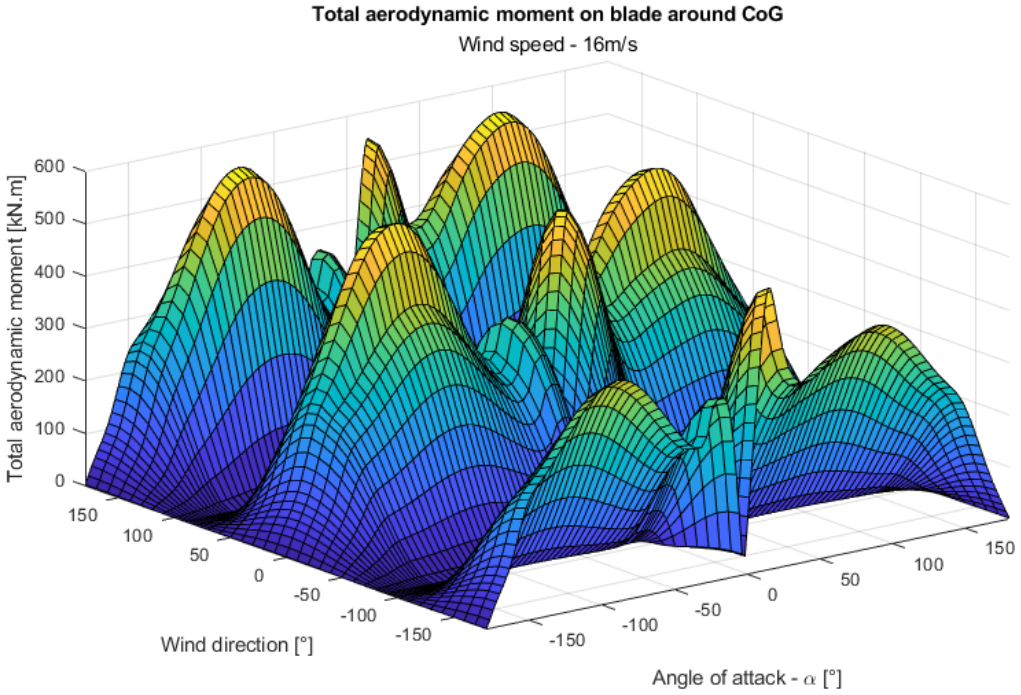


**Figure B.2:** Total aerodynamic moment acting on the blade, around its CoG, as a function of wind direction and angle of attack. Wind speed of 16m/s.

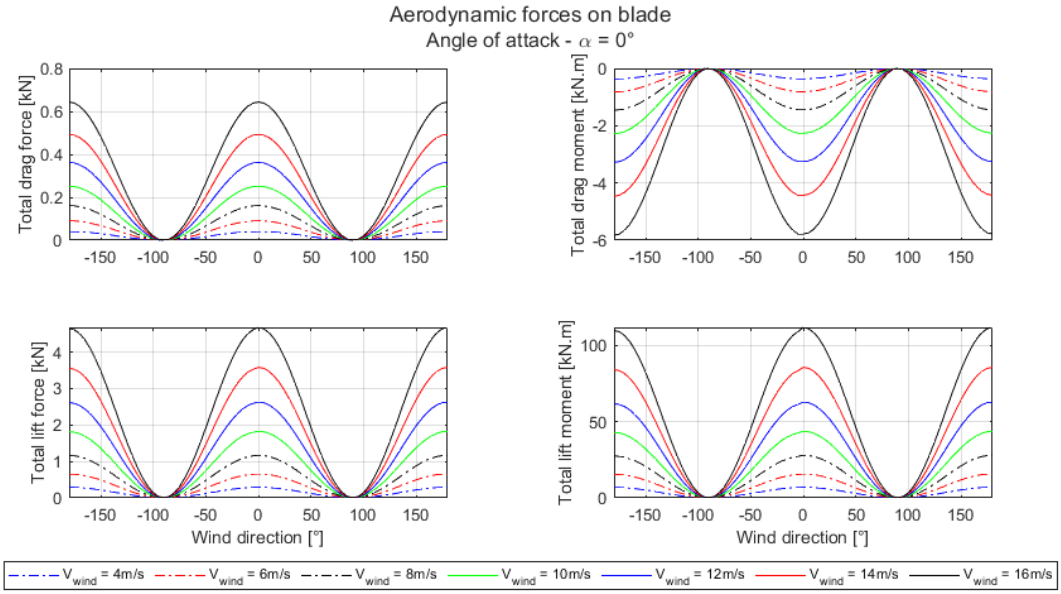


**Figure B.3:** Total lift and drag forces and moments acting on the blade as a function of the wind speed and direction. Angle of attack $\alpha = 0°$.

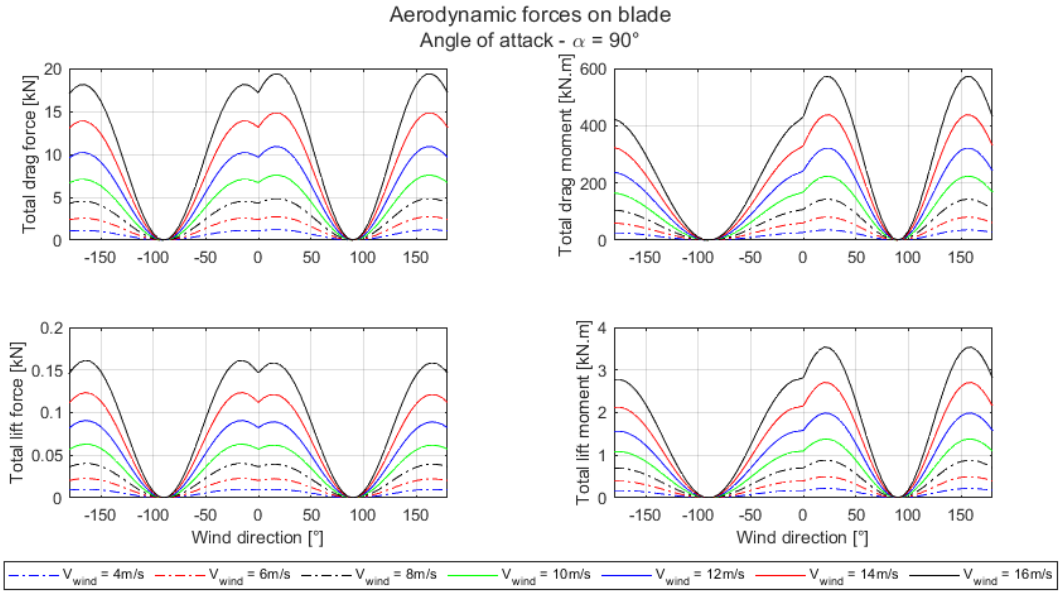


**Figure B.4:** Total lift and drag forces and moments acting on the blade as a function of the wind speed and direction. Angle of attack $\alpha = 90°$.

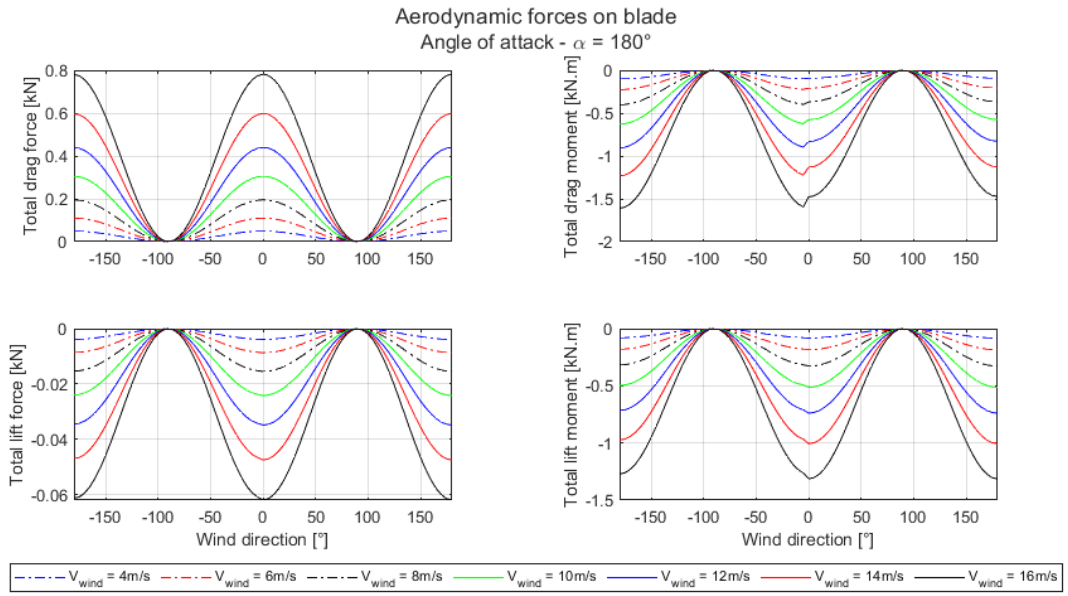


**Figure B.5:** Total lift and drag forces and moments acting on the blade as a function of the wind speed and direction. Angle of attack $\alpha = \pm 180°$.

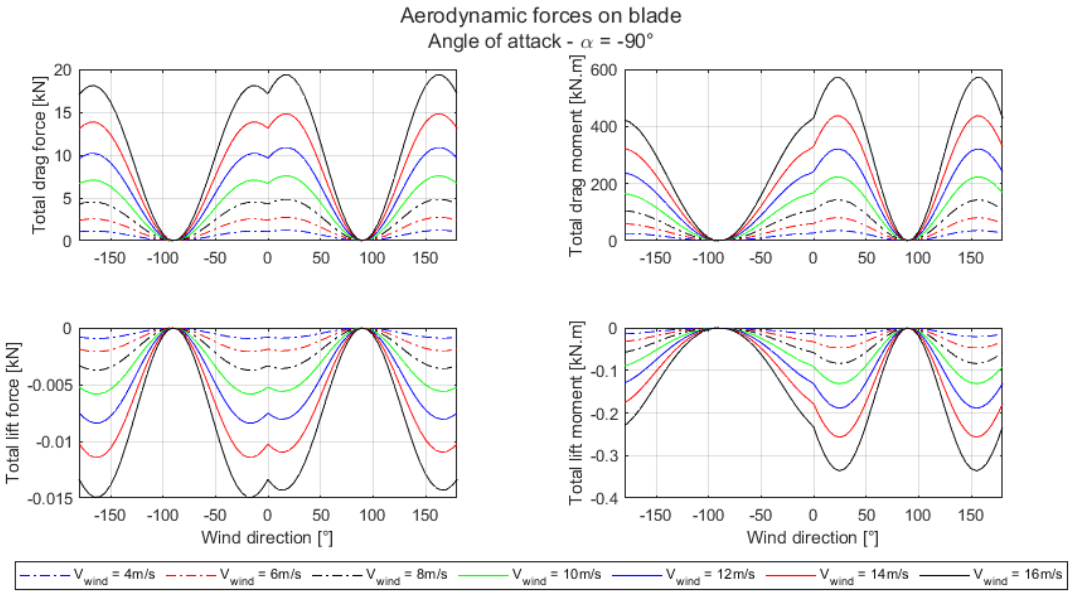


**Figure B.6:** Total lift and drag forces and moments acting on the blade as a function of the wind speed and direction. Angle of attack $\alpha = -90°$.

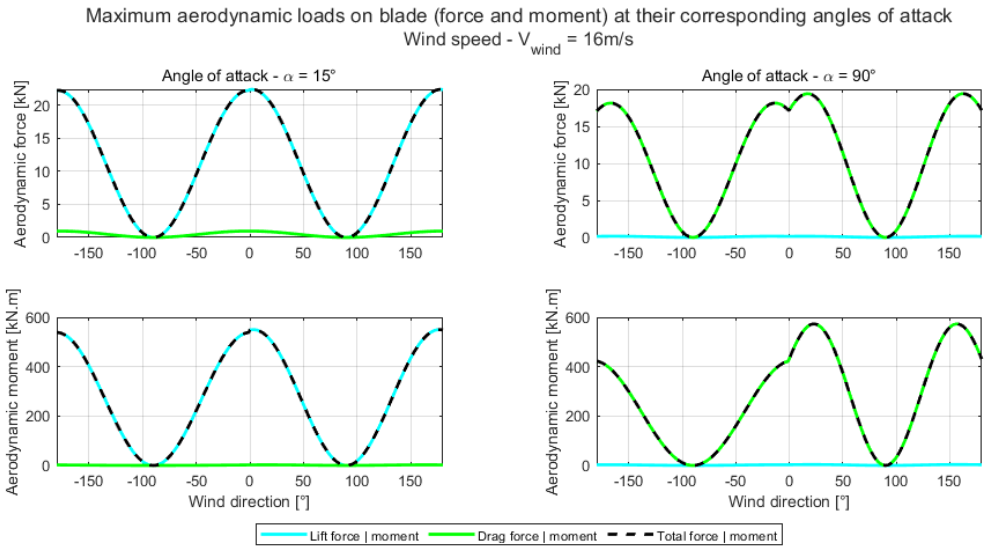


**Figure B.7:** Aerodynamic force and moment as a function of wind direction for fixed angles of attack. Wind speed of 16m/s.

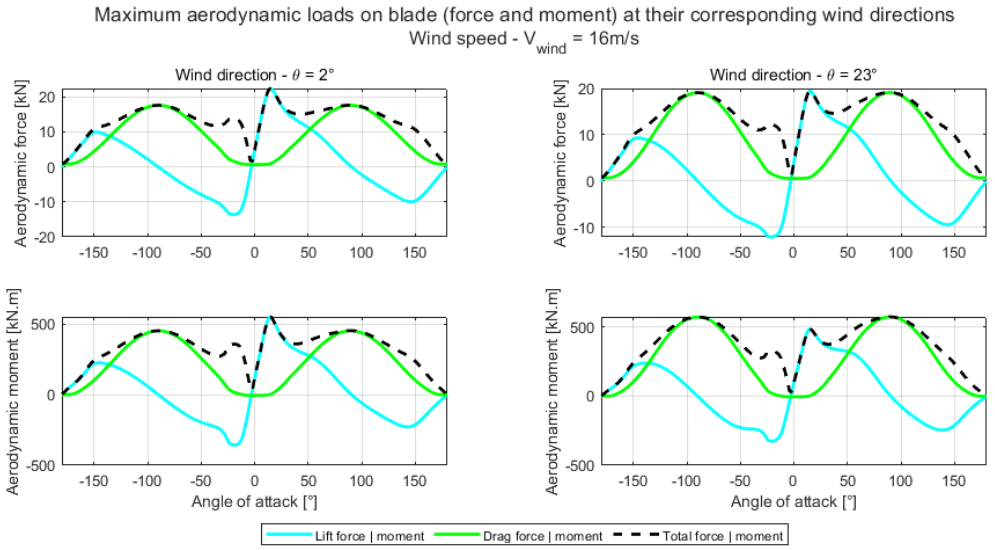


**Figure B.8:** Aerodynamic force and moment as a function of angle of attack for fixed wind directions. Wind speed of 16m/s.

# C

# Motion control results

The results presented in Chapter 6 correspond to the load case #29. The results corresponding to the load cases #19, #20, and #30 are presented in this appendix. The choice of these additional load cases was to present cases with different configurations with respect to the number of blades installed, as well as opposite wind and wave directions.

It is important to note that the controller gains were not changed, neither were the filter parameters.

## C.1. Load case #19

- Wind speed: 14 m/s.
- Wind direction: 0° - from the stern.
- Significant wave height $H_S$: 2.5 m.
- Wave peak period $T_P$: 8 s.
- Wave direction: -90° - from the portside.
- Number of blades installed in the hub: 1 blade.

**Table C.1:** Maximum absolute error and error standard deviation per actuator - Load case 19.

| Noise | Actuator | #1 | #2 | #3 | #4 | #5 | #6 |
|---|---|---|---|---|---|---|---|
| No | Error std. [mm] | 1.9 | 9.2 | 3.5 | 1.6 | 9.1 | 3.7 |
| | Max. abs. error [mm] | 6.7 | 28.1 | 10.5 | 5.1 | 27.5 | 11.0 |
| Unfiltered | Error std. [mm] | 2.2 | 9.3 | 3.7 | 2.1 | 9.2 | 4.0 |
| | Max. abs. error [mm] | 8.3 | 28.9 | 12.3 | 7.7 | 28.6 | 12.8 |
| Filtered | Error std. [mm] | 2.6 | 11.1 | 4.3 | 2.3 | 11.0 | 4.6 |
| | Max. abs. error [mm] | 9.0 | 34.8 | 13.4 | 8.1 | 34.2 | 14.2 |

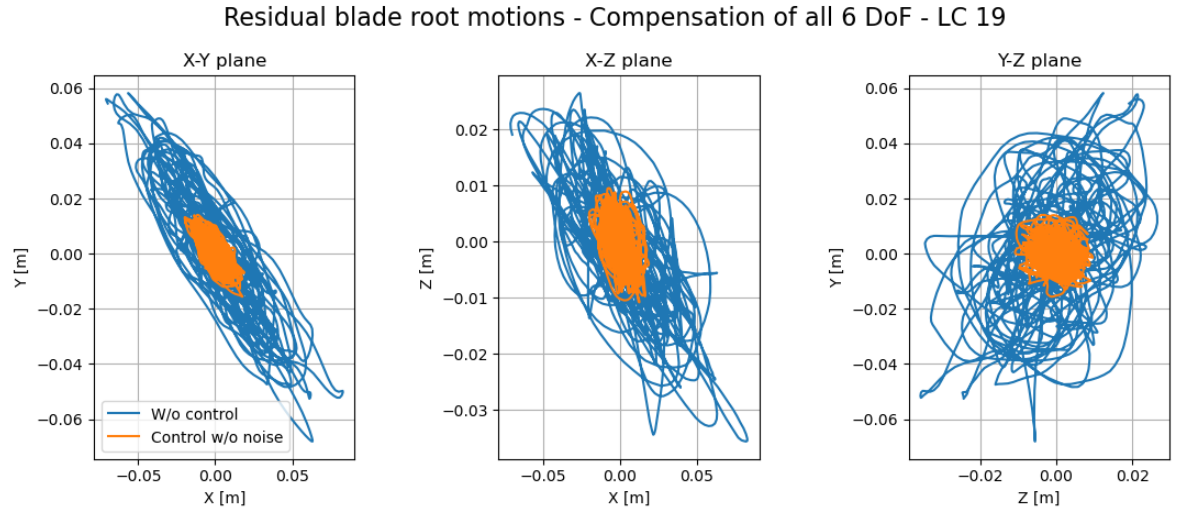


**Figure C.1:** Blade root residual motion without motion control (blue) and with the proposed control system (orange) - No instrumentation noise - Load case 19.

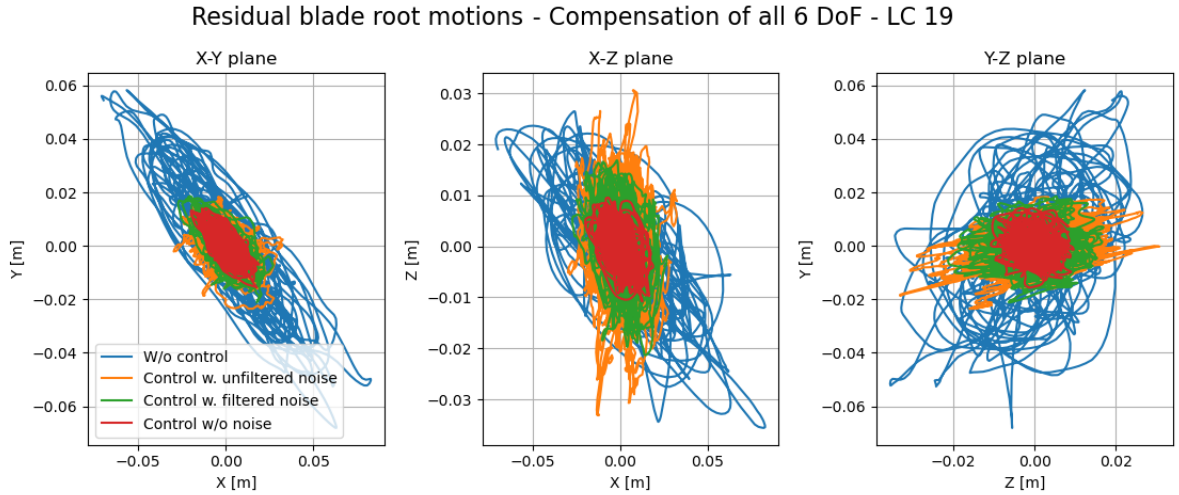


**Figure C.2:** Blade root residual motion without motion control (blue), with the proposed motion control system without instrumentation noise (red), with unfiltered instrumentation noise (orange), and filtered noise (green) - Load case 19.

**Table C.2:** Maximum absolute error and error standard deviation per degree of freedom - Load case 19.

| Noise | Degree of freedom | X [mm] | Y [mm] | Z [mm] | Rx [°] | Ry [°] | Rz [°] |
|---|---|---|---|---|---|---|---|
| No control | Error std. | 25.5 | 22.4 | 11.5 | 0.02 | 0.04 | 0.01 |
| | Max. abs. error | 82.8 | 68.1 | 35.6 | 0.07 | 0.13 | 0.03 |
| No | Error std. | 6.5 | 4.9 | 4.0 | 0.01 | 0.01 | 0.00 |
| | Max. abs. error | 19.9 | 15.6 | 10.8 | 0.03 | 0.03 | 0.01 |
| Unfiltered | Error std. | 8.3 | 5.7 | 7.6 | 0.02 | 0.01 | 0.01 |
| | Max. abs. error | 32.5 | 23.5 | 33.2 | 0.08 | 0.05 | 0.05 |
| Filtered | Error std. | 8.2 | 6.3 | 6.0 | 0.01 | 0.01 | 0.01 |
| | Max. abs. error | 27.2 | 21.2 | 21.3 | 0.05 | 0.04 | 0.03 |

## C.2. Load case #20

- Wind speed: 14 m/s.
- Wind direction: -90° - from portside.
- Significant wave height $H_S$: 2.5 m.
- Wave peak period $T_P$: 8 s.
- Wave direction: 0° - from the stern.
- Number of blades installed in the hub: 1 blade.

**Table C.3:** Maximum absolute error and error standard deviation per actuator - Load case 20.

| Noise | Actuator | #1 | #2 | #3 | #4 | #5 | #6 |
|---|---|---|---|---|---|---|---|
| No | Error std. [mm] | 1.0 | 5.3 | 2.9 | 1.3 | 5.4 | 3.1 |
| | Max. abs. error [mm] | 3.1 | 16.8 | 9.7 | 4.8 | 17.6 | 10.5 |
| Unfiltered | Error std. [mm] | 1.5 | 5.3 | 3.0 | 1.8 | 5.4 | 3.2 |
| | Max. abs. error [mm] | 5.8 | 19.5 | 10.6 | 6.9 | 20.2 | 11.7 |
| Filtered | Error std. [mm] | 1.8 | 6.5 | 3.7 | 2.0 | 6.6 | 3.9 |
| | Max. abs. error [mm] | 6.0 | 22.6 | 12.4 | 8.3 | 24.0 | 13.7 |

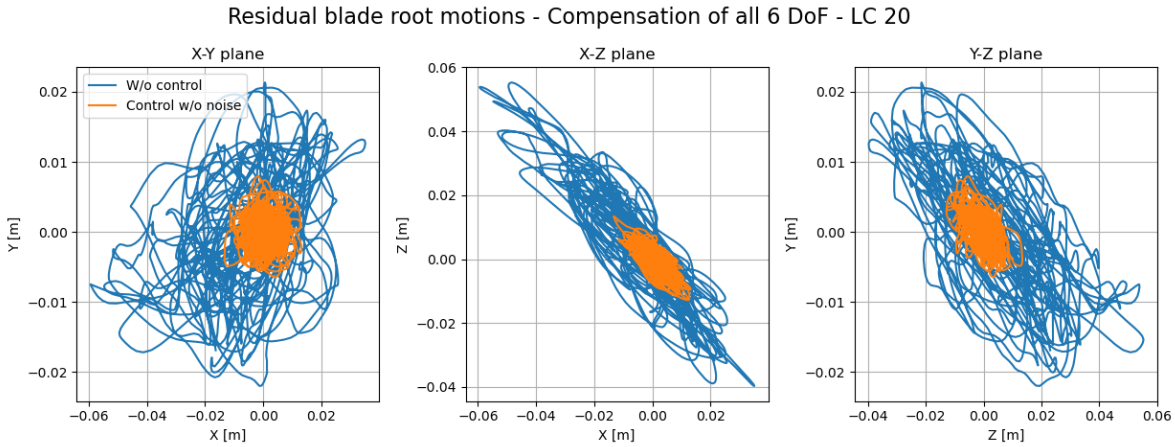


**Figure C.3:** Blade root residual motion without motion control (blue) and with the proposed control system (orange) - No instrumentation noise - Load case 20.

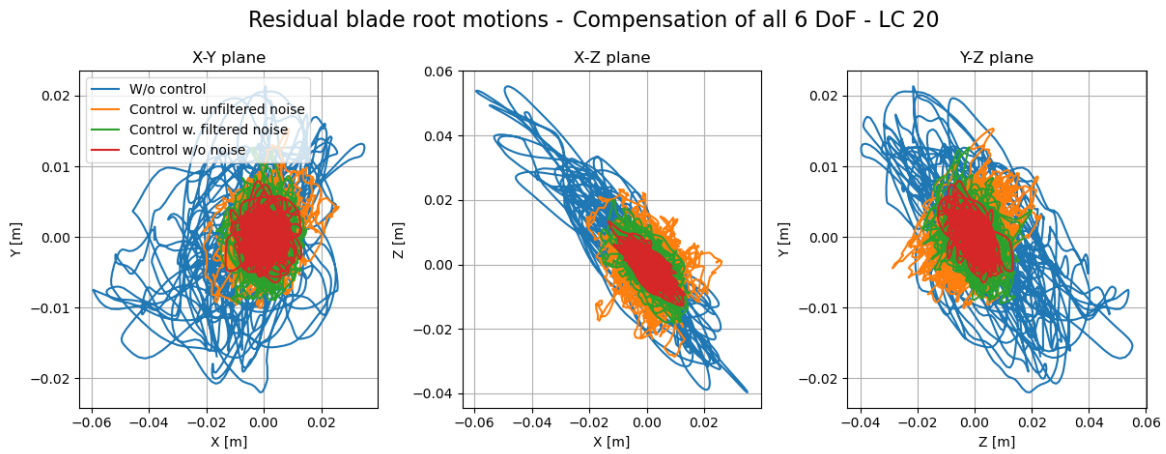


**Figure C.4:** Blade root residual motion without motion control (blue), with the proposed motion control system without instrumentation noise (red), with unfiltered instrumentation noise (orange), and filtered noise (green) - Load case 20.

**Table C.4:** Maximum absolute error and error standard deviation per degree of freedom - Load case 20.

| Noise | Degree of freedom | X [mm] | Y [mm] | Z [mm] | Rx [°] | Ry [°] | Rz [°] |
|---|---|---|---|---|---|---|---|
| No control | Error std. | 16.4 | 8.9 | 18.0 | 0.02 | 0.02 | 0.00 |
| | Max. abs. error | 59.4 | 22.0 | 55.3 | 0.04 | 0.08 | 0.01 |
| No | Error std. | 4.3 | 2.2 | 3.9 | 0.00 | 0.01 | 0.00 |
| | Max. abs. error | 13.3 | 7.9 | 13.4 | 0.01 | 0.02 | 0.01 |
| Unfiltered | Error std. | 5.3 | 3.1 | 6.4 | 0.01 | 0.01 | 0.01 |
| | Max. abs. error | 26.1 | 15.3 | 28.7 | 0.06 | 0.04 | 0.03 |
| Filtered | Error std. | 5.2 | 3.4 | 5.4 | 0.01 | 0.01 | 0.00 |
| | Max. abs. error | 16.5 | 12.7 | 19.9 | 0.03 | 0.04 | 0.02 |

## C.3. Load case #30

- Wind speed: 14 m/s.
- Wind direction: -90° - from portside.
- Significant wave height $H_S$: 2.5 m.
- Wave peak period $T_P$: 8 s.
- Wave direction: 0° - from the stern.
- Number of blades installed in the hub: 2 blades.

**Table C.5:** Maximum absolute error and error standard deviation per actuator - Load case 30.

| Noise | Actuator | #1 | #2 | #3 | #4 | #5 | #6 |
|---|---|---|---|---|---|---|---|
| No | Error std. [mm] | 1.3 | 4.8 | 3.5 | 1.6 | 5.0 | 3.8 |
| | Max. abs. error [mm] | 3.5 | 16.1 | 9.9 | 4.7 | 16.6 | 10.6 |
| Unfiltered | Error std. [mm] | 1.7 | 5.0 | 3.7 | 2.0 | 5.2 | 4.0 |
| | Max. abs. error [mm] | 6.0 | 16.8 | 11.1 | 6.6 | 17.8 | 11.9 |
| Filtered | Error std. [mm] | 2.1 | 5.9 | 4.4 | 2.4 | 6.1 | 4.8 |
| | Max. abs. error [mm] | 6.8 | 18.8 | 13.2 | 7.2 | 20.1 | 14.6 |

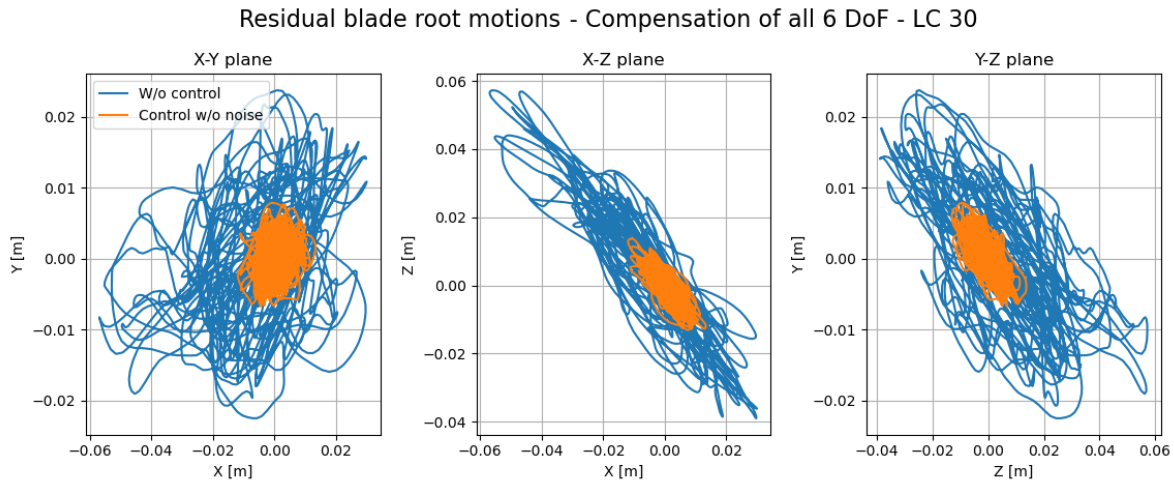


**Figure C.5:** Blade root residual motion without motion control (blue) and with the proposed control system (orange) - No instrumentation noise - Load case 30.

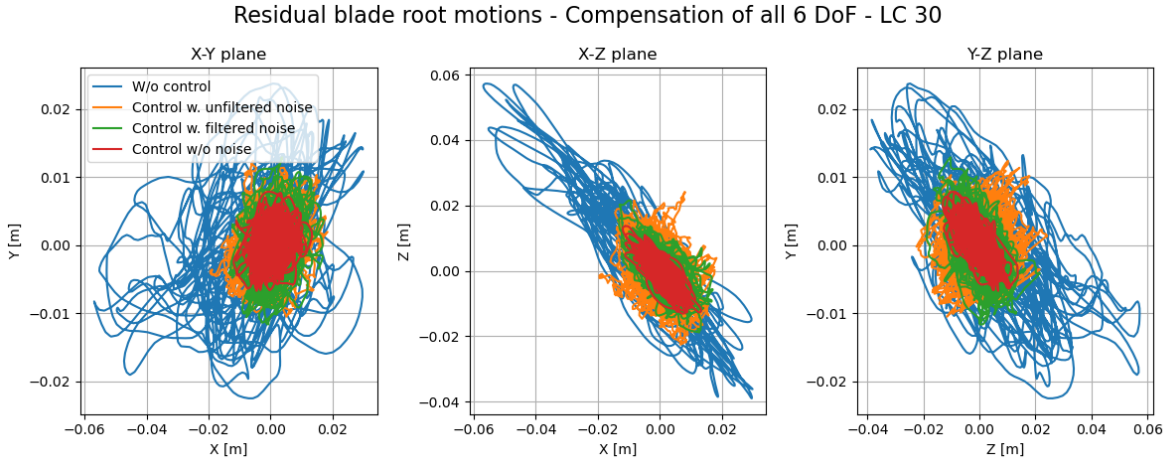


**Figure C.6:** Blade root residual motion without motion control (blue), with the proposed motion control system without instrumentation noise (red), with unfiltered instrumentation noise (orange), and filtered noise (green) - Load case 30.

**Table C.6:** Maximum absolute error and error standard deviation per degree of freedom - Load case 30.

| Noise | Degree of freedom | X [mm] | Y [mm] | Z [mm] | Rx [°] | Ry [°] | Rz [°] |
|---|---|---|---|---|---|---|---|
| No control | Error std. | 16.2 | 9.3 | 18.5 | 0.02 | 0.02 | 0.01 |
| | Max. abs. error | 56.9 | 23.8 | 57.2 | 0.05 | 0.08 | 0.02 |
| No | Error std. | 4.0 | 2.7 | 4.5 | 0.00 | 0.01 | 0.00 |
| | Max. abs. error | 13.3 | 7.9 | 13.7 | 0.02 | 0.02 | 0.01 |
| Unfiltered | Error std. | 5.2 | 3.5 | 6.4 | 0.01 | 0.01 | 0.01 |
| | Max. abs. error | 19.4 | 12.4 | 24.1 | 0.05 | 0.06 | 0.04 |
| Filtered | Error std. | 5.1 | 4.0 | 5.8 | 0.01 | 0.01 | 0.00 |
| | Max. abs. error | 17.1 | 12.9 | 21.5 | 0.03 | 0.03 | 0.02 |